PHYSICS DEPARTMENT

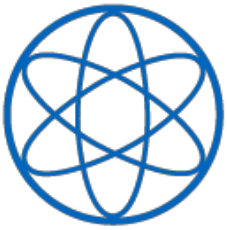

Heat Transport in Evacuated Perlite Powder Insulations and Its Application in Long-Term Hot Water Storages

Master Thesis
of
Matthias Demharter

TECHNISCHE UNIVERSITÄT
MÜNCHEN

Heat Transport in Evacuated Perlite Powder Insulations and Its Application in Long-Term Hot Water Storages

Master Thesis

of

Matthias Demharter

Technische Universität München

Physics Department

Supervisor: Prof. Dr. Rudolf Gross

Bavarian Center for Applied Energy Research (ZAE Bayern)

Division 1: Technology for Energy Systems and Renewable Energy

Advisor: Dr. Thomas Beikircher

Garching, August 2011

Abstract

For many years, the technique of vacuum super insulation (VSI) with expanded perlite has been used for cryogenic applications, especially the storage of liquid gases at temperatures of $20\,\mathrm{K} \leq T \leq 90\,\mathrm{K}$. Expanded perlite is an amorphous, highly porous, granular material of volcanic origin. Its two main components are SiO_2 (70 %) and Al_2O_3 (15 %). Due to the small pore diameters and the small distances between the grains, gas conduction in the pores and in the intergranular spaces is suppressed already in the regime of fine vacuum ($p \approx 0.01\,\mathrm{mbar}$). As a consequence of the material structure, solid conduction is inhibited to a great extent. Furthermore, thermal radiation is blocked by the opaque solid.

Due to these properties and as a consequence of the temperature dependency of the radiative heat transport, which scales with T^4, effective thermal conductivities as low as 3 to $5 \cdot 10^{-3}\,\mathrm{W/mK}$ have been realized at cryogenic temperatures. Compared to conventional insulation materials like polyurethane or rock wool at ambient temperature, the thermal conductivity is lowered by a factor of 6 to 10. A commercially available type of expanded perlite is TECHNOPERL ® - C 1,5 from the Austrian manufacturer EUROPERL, STAUSS PERLITE GMBH. This specific material is actually used in practice for liquid gas storage tanks.

In a current federally granted research project at ZAE Bayern (grant number 0325964A, German ministry of environment), the approach is pursued to apply perlite based VSI also at higher temperatures. Primarily, the long-term and seasonal storage of hot water up to $T = 150\,°\mathrm{C}$ in solar thermal heating systems is considered. However, other fields of application have also been identified, for example the intermediate storage of thermal energy in industrial processes or in solar thermal power plants for electric power generation. So far, experimental data for the effective thermal conductivity λ_{eff} of evacuated perlite in this temperature regime has been very rare. Therefore, various measurements have been performed within this thesis in order to determine λ_{eff} of TECHNOPERL ® - C 1,5 at different temperatures ($20\,°\mathrm{C} \leq T \leq 150\,°\mathrm{C}$), vacuum pressures ($10^{-3}\,\mathrm{mbar} \leq p \leq 10^{3}\,\mathrm{mbar}$), densities ($55\,\mathrm{kg/m^3} \leq \rho \leq 95\,\mathrm{kg/m^3}$) and grain structures (self-compression of the bulk by space-saving arrangement in a close-packing of spheres on the one hand versus application of external mechanical pressure, resulting in partial grain destruction on the other hand). Laboratory experiments have been

done both in an existing parallel plate apparatus and in a cut-off cylinder device, which was specially designed and set up during this thesis. In order to separately determine the radiative heat transport, Fourier transform infrared spectroscopy (FTIR) measurements have been performed and evaluated. Furthermore, a real-size cylindrical storage prototype with a water storage volume of $V = 16.4\,\mathrm{m^3}$ has been available for experiments under practical conditions.

In order to interpret and compare the measurement data, a theoretical understanding of the different heat transport mechanisms contributing to the effective thermal conductivity of evacuated perlite has been developed, and it has been possible to explain the results of all four measurements in a consistent way. For this theoretical description, conventional approaches and models have been used, which have successfully been applied to similar systems during the last decades, and which can be found in literature: The pressure dependency of gaseous conduction has been characterized using the Sherman interpolation between the continuum at high pressures and the regime of free molecular flow at low pressures. Regarding the solid thermal conductivity, a linear dependency on density has been derived from the experimental data. This result is in agreement with other empirical findings. However, the initially assumed dependency of solid conduction on temperature has not been observable. Radiative heat transport has been treated using the heat diffusion model, which describes absorption and scattering of thermal radiation within a material and allows the introduction of a radiative thermal conductivity. For the gas conduction in the intergranular spaces, also referred to as coupling effect, a special new model for perlite has been developed, based on approaches, which have originally been applied to particle beds in general, and have also been adapted to aerogels in particular.

For gaseous conduction inside the pores, the experimentally determined characteristic half-value pressure for air ranges from $p^g_{1/2} = 1.38\,\mathrm{mbar}$ to $p^g_{1/2} = 5.1\,\mathrm{mbar}$. These values correspond to effective mean pore diameters of $d_p = 167\,\mu\mathrm{m}$ and $d_p = 45.1\,\mu\mathrm{m}$. Similar results have been obtained from measurements with the inert gases argon ($p^g_{1/2} = 1.46\,\mathrm{mbar}$) and krypton ($p^g_{1/2} = 1.24\,\mathrm{mbar}$). For the coupling term, a half-value pressure of $p^c_{1/2} = 39\,\mathrm{mbar}$ has been derived from the measurements with air. This result is equivalent to an effective grain interspace of $d_g = 5.9\,\mu\mathrm{m}$. For argon and krypton, the respective values are $p^c_{1/2} = 17.4\,\mathrm{mbar}$ (argon) and $p^c_{1/2} = 4.5\,\mathrm{mbar}$ (krypton). This might indicate that the interaction of the heavy noble gases with the perlite surface is different from the diatomic air molecules N_2 and O_2.

For practical purposes, simple formulas have been derived to calculate the effective thermal conductivity λ_{eff} of TECHNOPERL ® - C 1,5 and its individual components λ_r (radiative heat transport), λ_s (solid conduction), λ_g (gas conduction in pores) and λ_c (coupling effect) as a function of vacuum pressure (including the filling gases air, argon and krypton), bulk density and temperature. This knowledge is of particular interest

for the application of vacuum super insulation in practice. From the theoretical models and the experimental results, it has been possible to suggest optimization approaches to minimize λ_{eff}. Currently, a value as low as $\lambda_{eff} = 9.2 \cdot 10^{-3}$ W/mK has been achieved for the real-size prototype at a mean water temperature of $T = 86.4$ °C, which is composed of $\lambda_r = 2.6 \cdot 10^{-3}$ W/mK, $\lambda_s = 5.1 \cdot 10^{-3}$ W/mK and $\lambda_g + \lambda_c = 1.5 \cdot 10^{-3}$ W/mK. By using a bulk density of around $\rho = 60$ kg/m³ and lowering the vacuum pressure to $p = 0.01$ mbar, this value is expected to decrease to $\lambda_{eff} \approx 7.3 \cdot 10^{-3}$ W/mK according to the theoretical predictions. The application of inert filling gases like argon or krypton has been proven to be disadvantageous.

A further experimental task was the determination of the moisture content within TECHNOPERL ® - C 1,5. According to theory, moisture in its liquid or gaseous form can dramatically increase the thermal conductivity of an insulation in some cases. However, as a result of the experiments and due to phase diagram considerations, these effects can be neglected for practical applications.

Contents

Chapter 1

Introduction

1.1 Motivation and Background

During the last years, renewable energy sources have continuously gained importance (figure 1.1). In Germany, roughly 10 % of the overall energy demand are meanwhile supplied from renewables [1]. As one of the pioneering nations regarding the expansion of renewable energies, the German government has declared the intent to increase this fraction to 18 % until 2020 and to 50 % by 2050 [2]. Also in other countries, there are initiatives to expand the usage of renewable energies. This development is mainly motivated by the ambition of climate protection. In general, an increasing awareness for sustainability has been observed in our society during the last years [3]. Especially nuclear energy has dramatically lost its acceptance as a consequence of the recent series of accidents at the Fukushima nuclear power plant [4]. The nuclear power phase-out until 2022, which was subsequently decided by the German government [5], is planned to be realized by enhanced application of renewable energies.

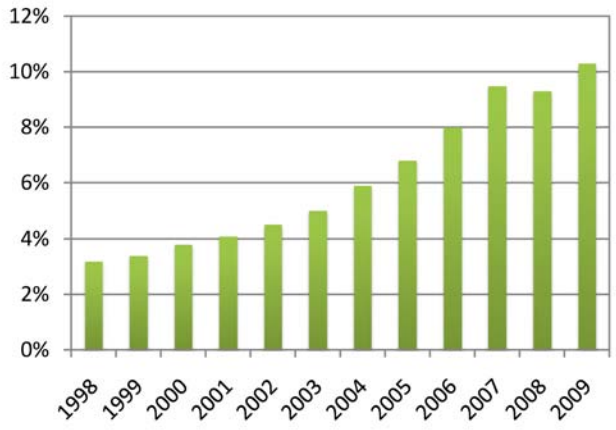

Figure 1.1: Contribution of renewables to the supply of final energy in Germany [1].

However, the change from conventional energy sources to renewables can not be accomplished just by political decisions and societal trends. Economic factors also play an important role. In many cases, burning fossil fuels for heating and electric power generation is still favorable from the economic point of view, not to mention automotive and transport applications. Nevertheless, because the availability of fossil fuels is beginning to decrease [6] and prices have steadily been rising (figure 1.2) [7], the break-even point might soon be reached. Due to the recent introduction of CO_2 emissions trading [8], renewable energy sources will be more competitive in future. In both the economic and environmental context, also the terms of energy saving and energy efficiency have gained a greater significance.

Even in an industrialized country like Germany, the supply of hot water for domestic use and residential heating makes up a considerable fraction of approximately 20 % [9] of the total energy demand (compare also figure 1.3). Most heating systems are still based on fossil fuels like oil or gas, but there is a huge potential to provide the energy required for this purpose from renewable sources. Modern solar thermal systems [10, 11] have become an economically reasonable alternative, not to mention environmental factors like reduction of CO_2 emissions.

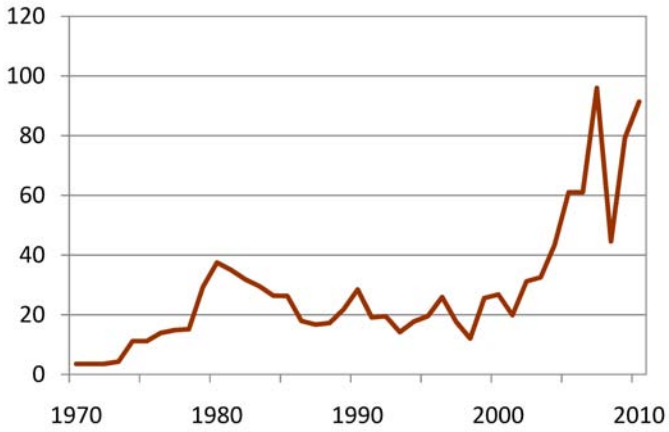

Figure 1.2: Development of the crude oil price in US Dollar per barrel [12].

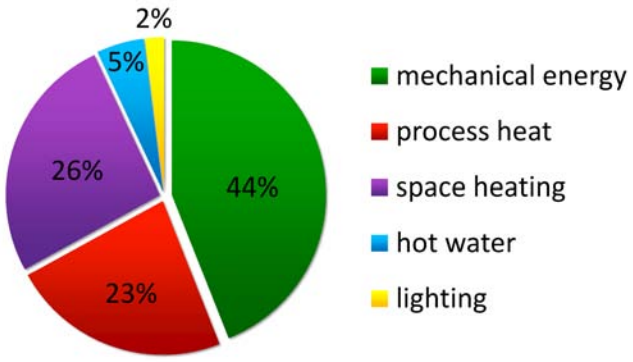

Figure 1.3: Energy demand profile of Germany in 2007 [7].

A solar thermal system for single-family houses (figure 1.4) basically consists of a collector and a storage. The essential component of any collector is the absorber, which heats up as it absorbs the incoming solar radiation. For simple and economic collectors, the emissivity ε (and thus also the absorptivity α, see section 2.3) of the absorber surface is typically close to 1 in the whole spectral range. Modern absorbers in high-efficiency collectors have a selective coating with a high emissivity only in the range of incoming radiation and a low emissivity in the infrared regime in order to reduce losses from re-emission [13]. The heat emerging at the absorber is led away by the heat carrier, often a mixture of water and glycol for frost protection, which flows through the collector. The existing types of collectors basically only differ from each other regarding the insulation techniques that are applied in order to reduce thermal losses. Due to this, also the geometrical layout varies. Free convection is usually suppressed by glass covers. Common flat plate collectors are additionally insulated with mineral wool or similar materials on their rear side and reach efficiencies of 50 - 60 % at typical operation temperatures between 50 and 80 °C [14, 15]. Evacuated tube collectors utilize the insulating properties of vacuum to obtain higher efficiencies at operation temperatures up to 120 °C.

Since solar irradiation is not constantly available, thermal storages are fundamentally important for solar thermal systems. A typical storage tank is built in a slim, cylindrical layout. Due to the the temperature dependency of the density of water, this design allows the development of a stable temperature gradient to maximize the storage exergy. The water at the bottom of the tank is colder and thus heavier than the hotter water layered further above. To charge the storage with the heat coming from the collector, a heat exchanger is installed at the cold bottom of the tank. Hence, the temperature of the heat carrier fluid running back into the collector circuit reaches a lower level, which is more beneficial for the overall efficiency of the system [14]. The connections for the extraction of hot water are located in the upper part of the tank to ensure water supply with the hottest possible temperature.

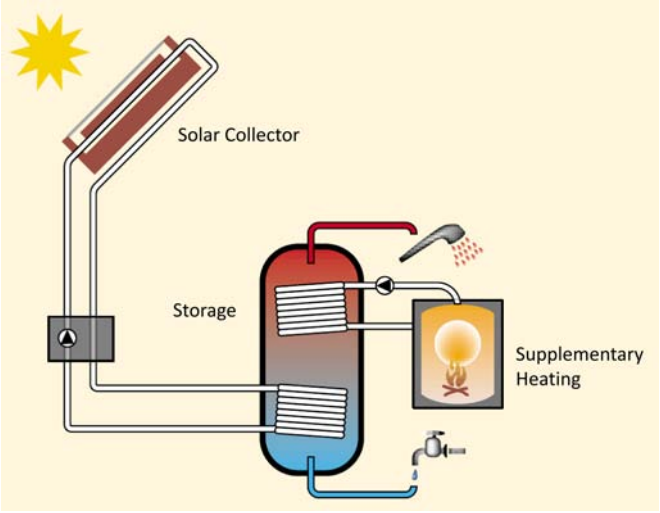

Figure 1.4: System overview of a solar thermal heating installation [14].

An important component of any storage is its insulation, which reduces the thermal losses of the stored hot water to its colder surroundings. At present, storages are insulated using conventional materials like mineral wool or polyurethane foam. The heat conductivity λ of these materials (at room temperature) is typically between 0.024 and 0.05 W/mK.

Most of today's solar thermal installations are only used to produce hot water for domestic use. Only a minority of installed facilities also supports residential heating. With a collector area of 10 - 20 m² and storage sizes between 500 and 1500 liters [16], such systems can provide around 20 - 30 % of the total heat demand of a single-family house (solar fraction). The remaining bigger part must still be supplied by fossil fuels. A detailed investigation using numerical simulation methods [17] shows, that the solar fraction can be improved not only by lowering the heat conductivity of the insulation, but also by increasing the storage volume to 10 - 20 m³ (assuming reasonably-sized collectors). In this way it is possible to transfer the thermal energy generated at days with high solar irradiation into colder periods. Due to this long-time storage, solar fractions of more than 50 % are possible (fossil-supported solar heating). In the extreme case, the heat generated in summer can be carried over into the winter months. This concept is referred to as seasonal storage and allows solar fractions of up to 100 % (complete solar coverage). However, seasonal storage requires storage volumes of around 100 m³ and higher. So far, the number of solar thermal installations with such large storages and solar fractions greater than 50 % has been very low (only around 100 buildings in Germany [18]), although lately more and more manufacturers offer conventionally insulated tanks with volumes of several m³ for long-time storage [19, 20].

From a general consideration of the thermal energy storage process, some important principles for practical applications can be derived. The temperature T of the storage medium (initial temperature T_0) decreases with time t as a consequence of the thermal losses $\dot{Q}$ to the colder surroundings (ambient temperature T_a). On the one hand, $\dot{Q}$ is connected to the temperature decrease dT/dt by the integral heat capacity $C = c_p \rho V$ of the storage medium (c_p: specific heat capacity, ρ: density, V: storage volume). On the other hand, $\dot{Q}$ can be expressed by $\lambda A \left(T - T_a\right) / d$ (λ: heat conductivity of the insulation, A: tank surface, d: insulation thickness). After solving the emerging differential equation, the evolution of $T(t)$ can be calculated:

$$\begin{aligned}
\lambda \frac{A}{d} \left(T - T_a\right) &= \dot{Q} = -C \frac{dT}{dt} = -c_p \rho V \frac{dT}{dt} \\
\frac{dT}{T - T_a} &= -\frac{A\lambda}{c_p \rho V d} dt \\
\ln\left(\frac{T - T_a}{T_0 - T_a}\right) &= -\frac{A\lambda}{c_p \rho V d} t \\
T(t) &= \left(T_0 - T_a\right) \exp\left(-\frac{A\lambda}{c_p \rho V d} t\right) + T_a
\end{aligned} \tag{1.1}$$

On a sidenote, the relation $\dot{Q} = \lambda A \left(T - T_a\right) / d$ is an approximation, which is only valid if the insulation thickness is much smaller than the radius of the cylindrical tank ($d \ll r$, see section 2.1 for details). For practical applications, it is desired to keep the constant $A\lambda / c_p \rho V d$, which determines the cooling rate, as small as possible. Because ρ and c_p are natural properties of water, this can be achieved by three different approaches:

- A first possibility is to minimize the ratio A/V, which can be done by building large storage tanks. This result is in good agreement with the numerical simulations mentioned above, which showed that an up-scaling of the tank dimensions yields higher solar fractions. In addition, spherically-shaped storage tanks are most favorable regarding the ratio A/V. The cylindrical geometry is more practical in many applications, though.
- Furthermore, the cooling rate can be lowered by increasing the insulation thickness d. However, this method is limited by spatial restrictions. In practice, it is desired to obtain a reasonable ratio of storage volume against total tank volume.
- A third method is to use insulation materials and techniques which yield low thermal conductivities. This approach is pursued in this thesis.

In this context, a new super-insulated long-term hot water storage is being developed at the Bavarian Center for Applied Energy Research (ZAE BAYERN) in cooperation with HUMMELSBERGER GMBH, a medium-sized company in the branch of steel processing. The project is funded by the German Federal Environment Ministry [2]. The cylindrical tanks can be built in sizes between 5 and 100 m³. A particular feature is the application of vacuum super insulation. This technique is known from cryogenic engineering and is now used in solar thermal applications for the first time. By evacuating a microporous powder, all possible heat transfer mechanisms are effectively suppressed and in principal, thermal conductivities as low as 0.005 W/mK can be reached [17, 21]. The material used for this purpose is perlite, a porous compound of volcanic origin.

In general, the newly-developed storage tank can be applied to any kind of thermal energy storage process. From storage efficiency considerations, it is obvious though that an improvement of the thermal insulation is especially important for long storage durations and for high temperature levels (compare equation 1.1). Thus, one can identify the following main fields of application for the new super-insulated tank:

First, the long-term storage of solar thermal energy as described above is considered. Due to $T < 100\,°\mathrm{C}$, this represents an application at relatively low temperatures, but long storage durations. With maximum possible tank volumes of 100 m³, seasonal storage is also possible. For conventional solar thermal applications, the storage can be equipped with a special stratification device, which ensures that the water coming from the collector is inserted at the appropriate height according to its temperature. In this way, the temperature gradient can be kept stable, and a mixing of the different temperatures is prevented.

Moreover, one can also think of the intermediate storage of industrial process heat to improve the energy efficiency and to lower production costs. Roughly a third of the process heat demand is in the temperature range below 250 °C [22]. Relevant branches are for example the chemical industry, food industry and paper production. At this temperature level, pressurized water is a suitable storage medium. With recently developed collectors [23], heat at this temperature range ($T \approx 150\,°C$) can even be supplied by solar thermal systems.

Higher temperatures from 300 °C of up to 1600 °C are mainly needed for mineral oil and metal processing and for some processes in chemical industry. If it is possible to implement intermediate storage for these processes, their energy efficiency could be considerable increased, because vacuum super insulation is especially advantageous at these high storage temperatures. However, as a small restriction, the maximum temperature is limited, because the amorphous, glass-like perlite can not withstand temperatures above 800 °C. Furthermore, alternative storage media (e.g. molten salts) would have to be used.

As a third field of application, solar thermal power plants for electric power generation can be mentioned [24, 25]. For large-scale applications in the range of 10 to 50 MW, two different concepts can be distinguished. With parabolic trough collectors (figure 1.5 a), the incident solar radiation is concentrated on a focal line. Concentration factors of around 80 and temperatures close to 400 °C can be reached. Even higher temperatures are possible with solar towers (figure 1.5 b), which are also called central receiver systems (CRS). Here, an arrangement of reflectors (heliostats) is used to concentrate the solar radiation to a small volume at the central receiver, which is located on top of a stationary tower. Concentration factors of 500 to 1000 and temperatures of up to 1100 °C can be achieved as a consequence of the two-dimensional concentration. The theoretical limit is given by $T = 5777\,K$, which is the surface temperature of the sun. In both concepts, conventional turbines are used to generate electricity.

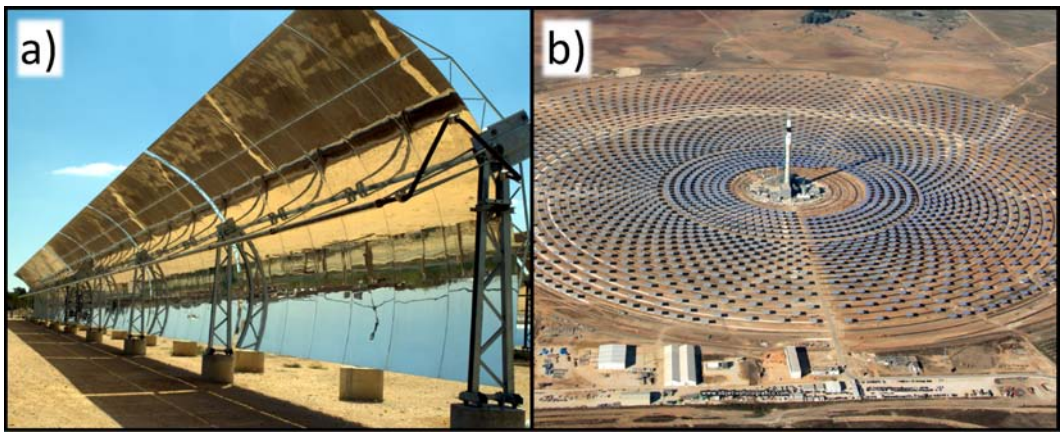

Figure 1.5: Parabolic trough collector at the National Solar Energy Center in Israel (a), Gemasolar CRS power plant in Fuentes de Andalucía, Spain (b) [26, 27].

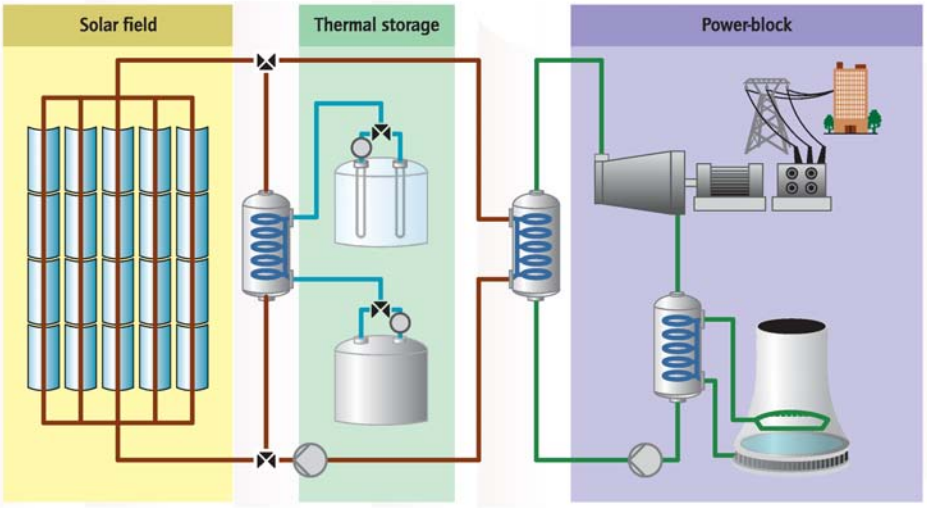

Figure 1.6: System overview of a solar thermal power plant with thermal storage [25].

The implementation of intermediate thermal storage is possible for both systems and has already been realized (figure 1.6). In this way, excess heat can be stored during the day, and the power plant can continue to generate electricity after sunset. For example, the operation time can be extended by an interval of up to 7 hours in some parabolic trough plants in Spain. With a combination of collectors, storages and turbines of appropriate sizes, configurations for base load, medium load and peak load supply can be set up. In the relevant temperature regime, molten salts are often used as a storage medium. With the application of vacuum super insulation, which is especially advantageous at high temperatures, the efficiency of the storage process can be increased.

1.2 Definition of Tasks and Goals

The primary aim of this thesis is the theoretical and experimental investigation of the heat transport in an evacuated perlite powder insulation. This includes both the quantification of the overall heat conductivity and the analysis of different heat transport mechanisms as a function of pressure, temperature and density. Based on this fundamental understanding, another goal is to examine how the total thermal conductivity can be minimized under economical aspects in practice, and to formulate optimization approaches for the application in long-term hot water storages.

1.3 Structure and Procedure

In the first part of this report, the physical and technical background of vacuum super insulation is depicted. After a short overview about heat transport in general (chapter 2) and a brief presentation of existing insulation techniques (chapter 3), the theory

of heat transport in the special case of evacuated powders is investigated in chapter 4. Subsequently, the material perlite and its general properties are treated (chapter 5). Apart from the cryogenic application mentioned above, vacuum super insulations have also been developed for civil engineering applications. Furthermore, the technology has been considered and examined for long-distance heating pipelines. Therefore, chapter 5 also presents the state of scientific and technical knowledge for these applications and motivates the additional research done in this thesis.

The second part is about the performed experiments. Laboratory measurements (chapter 6) have been done in order to provide a general understanding of the heat transport mechanisms of evacuated perlite. In addition, the influence of inert filling gases on the thermal conductivity has been analyzed, and the moisture content of the material has been determined. In order to examine whether the results from laboratory experiments remain valid under practical conditions, heat loss measurements have been performed on a real-size storage prototype (chapter 7). Both experimental chapters contain the description of the respective measurement setup and procedure as well as the presentation and discussion of results. Eventually, chapter 8 summarizes the experimental results with regard to the practical application of vacuum super insulation in hot water storages and outlines optimization approaches.

Chapter 2

Fundamentals of Heat Transport

Generally speaking, heat is the form of energy which can be transferred between thermodynamic systems as a consequence of a temperature difference [28]. Three different mechanisms of heat transport can be distinguished: conduction, convection and radiation. The following sections will briefly describe each of them and focus on equations that will be used in the further progression of this thesis. More detailed explanations can be found in relevant textbooks [10, 28, 30, 31, 32, 33].

2.1 Conduction

Conduction is a heat transfer mechanism that is based on the direct interaction between particles (atoms, molecules, electrons, phonons) and can occur in any kind of matter. Unlike radiation, conduction requires a medium, but no bulk movement of particles. In gases and liquids, the atoms or molecules are mobile, and conduction happens due to collisions of the particles along their random walk. In solids, by contrast, the atoms are bound in a lattice, and conduction is a result of vibrations, physically described by phonons. Additionally, there can be a contribution of free electrons.

Consider a homogeneous, arbitrarily-shaped, three-dimensional body composed of an isotropic material with a temperature distribution $T(\vec{x})$. In the stationary case, heat conduction can be mathematically expressed by Fourier's law. In its differential form it reads

$$\vec{\dot{q}} = -\lambda \vec{\nabla} T \tag{2.1}$$

where $\vec{\dot{q}}$ is the local heat flux per unit area, $\vec{\nabla} T$ is the temperature gradient and the constant of proportionality λ is the thermal conductivity of the material. This equation shows very descriptively that a heat flux is caused by a temperature gradient and that the flux in a certain direction is proportional to the temperature gradient in that specific direction. The negative sign expresses that heat flux is always directed towards decreasing temperatures.

For simple geometries, Fourier's law can be reduced into its one-dimensional form:

$$\dot{Q} = -A\lambda\frac{dT}{dr} \tag{2.2}$$

Here, the gradient $\vec{\nabla}T$ is replaced by the one-dimensional derivative dT/dr and the area A is introduced, which is always aligned normally to the direction of the heat flux $\dot{Q}$. For a planar geometry (e.g. an insulator sandwiched between two parallel plates with temperatures T_1 and T_2, see figure 2.1 a), one can easily solve this differential equation by integration to obtain:

$$\dot{Q}_p = \lambda\frac{A}{d}\left(T_1 - T_2\right) \tag{2.3}$$

In the cylindrical case (figure 2.1 b), with $A = 2\pi rH$ and after separation of variables and integration, one arrives at:

$$\dot{Q}_c = \lambda\frac{2\pi H}{\ln\left(r_2/r_1\right)}\left(T_1 - T_2\right) \tag{2.4}$$

If $d = r_2 - r_1 \ll r_1$ one can neglect terms of quadratic and higher order in the Taylor expansion of the logarithm and arrives at equation 2.3. This result is intuitively obvious, because the curvature of the cylindrical surfaces becomes very small in this case and therefore the planar geometry is a good approximation. It still has to be noted that equations 2.3 and 2.4 are only valid for plates with infinite dimensions and cylinders with infinite height. In the case of finite extensions, the influences of the boundaries are generally not negligible.

A geometry of concentrical spheres (figure 2.1 c) can be treated in analogy to the cylindrical case. By inserting $A = 4\pi r^2$ into equation 2.2, one can derive:

$$\dot{Q}_s = \lambda\frac{4\pi}{\frac{1}{r_1} - \frac{1}{r_2}}\left(T_1 - T_2\right) \tag{2.5}$$

Just like above, for $d = r_2 - r_1 \ll r_1$, the geometry can be approximated by equation 2.3. Due to the fact that spheres are closed surfaces, there are no boundary effects.

The heat flux in a general geometry (also three-dimensional) can be calculated using

$$\dot{Q}_g = \lambda S\left(T_1 - T_2\right) \qquad \text{with} \quad S = \frac{1}{T_1 - T_2}\iint\limits_A \vec{\nabla}T\,d\vec{A} \tag{2.6}$$

where S is a shape factor in units of length that describes the respective geometry. The shape factors for planar, cylindrical and spherical geometries can be read off by comparing equations 2.3, 2.4 and 2.5 with equation 2.6. Shape factors for more complicated technical configurations like squares, ribs and pipes can be found in [34]. This standard reference of engineering science also contains tabulated values for the heat conductivities of numerous gases, liquids and solids.

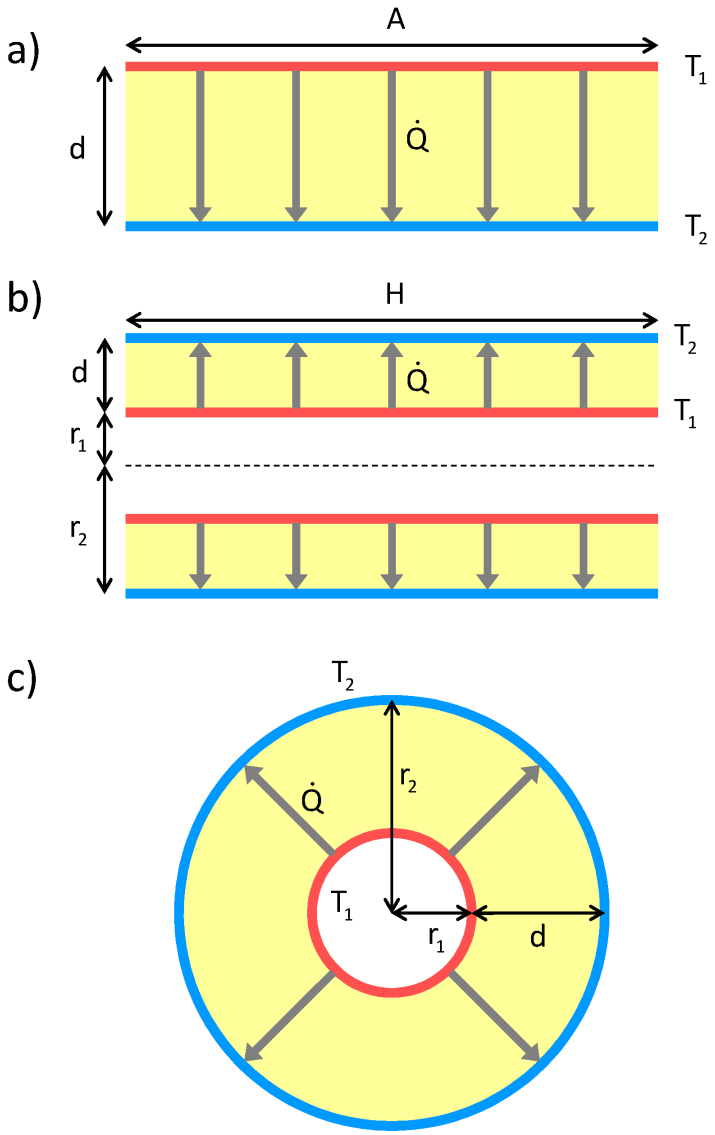

Figure 2.1: Heat conduction between parallel plates (a), concentric cylinders (b) and concentric spheres (c). The conducting material is depicted yellow. It has the thermal conductivity λ and the temperatures T_1 and T_2 at its boundaries.

2.2 Convection

When a (solid) surface is in contact with a fluid in motion, the heat transport between both is referred to as convection [28]. Convection includes both conduction and the effects that are connected to a bulk movement of atoms or molecules within the gas or liquid. The motion can be induced either by external action like fans, pumps or wind (forced convection) or by buoyancy forces due to temperature and therefore density differences (natural or free convection). In case of a fluid at rest, the heat transfer only happens via conduction. For that reason, conduction can be seen as the limiting case of convection.

Consider the case of air flowing over the surface of a hot solid (figure 2.2). The fluid layer at the boundary, which is at rest due to friction, heats up by conduction from the solid. At this point, convection takes effect: On the one hand, conduction within the fluid occurs, so that layers further above will also heat up eventually. On the other hand, the motion of the fluid carries away hot atoms or molecules, replacing them with colder ones. It is therefore obvious that the rate of heat exchange is enhanced compared to pure conduction. The convective heat transfer is described by Newton's law of cooling, which reads:

$$\dot{Q} = H_c A \left(T_s - T_\infty\right) \tag{2.7}$$

Here, T_s is the temperature of the solid. For continuity reasons, T_s is equal to the temperature of the boundary layer. T_∞ is the fluid temperature at large distances from the surface. Although convection is a rather complex phenomenon, the rate of heat exchange is proportional to the temperature difference $\Delta T = T_s - T_\infty$. The proportionality is expressed by the convection heat transfer coefficient H_c, which is not a material constant and in fact depends on a variety of fluid parameters like dynamic viscosity μ, thermal conductivity λ, density ρ and velocity v.

It is very common to introduce characteristic dimensionless numbers for the mathematical description of fluid dynamics. A very fundamental quantity derived from the convection heat transfer coefficient H_c is the Nusselt number Nu, which is defined as:

$$Nu = \frac{H_c \delta}{\lambda} \tag{2.8}$$

In this equation, δ is a characteristic length of the respective geometry. Examples for δ are the length of a plate in the direction of the fluid flow or the diameter of a pipe or sphere. For more complex geometries, δ can be defined as the fluid volume V divided by the surface area A.

The Nusselt number can be interpreted in a very descriptive way if one considers the heat transport within a fluid layer, which has a temperature T_1 at its bottom boundary surface A and temperature T_2 at the top border (figure 2.3). According to the above definition, the characteristic length δ is in this case given by the layer thickness d. The heat transport by conduction is equal to

$$\dot{Q}_{cond} = \lambda \frac{A}{d} \left(T_1 - T_2\right)$$

whereas the convective heat transport is given by:

$$\dot{Q}_{conv} = H_c A \left(T_1 - T_2\right)$$

Taking the ratio $\dot{Q}_{conv}/\dot{Q}_{cond}$ one obtains:

$$\frac{\dot{Q}_{conv}}{\dot{Q}_{cond}} = \frac{H_c A \left(T_1 - T_2\right)}{\lambda \frac{A}{d} \left(T_1 - T_2\right)} = \frac{H_c d}{\lambda} = \frac{H_c \delta}{\lambda} = Nu \tag{2.9}$$

Therefore, the Nusselt number expresses the proportion between convection and conduction, or in other words the enhancement of the conductive heat transport caused by fluid motion. A Nusselt number of $Nu = 1$ describes the case of pure conduction. From the fact that the Nusselt number can typically reach values from 10 up to 10.000 and even higher, it is obvious that convection is a very effective heat transport mechanism compared to pure conduction.

For natural convection, the Nusselt number can be expressed by the Rayleigh number Ra. The exact relation $Nu = f\,(Ra)$ depends on the geometry [34]. For an arrangement of two parallel plains with an inclination angle β towards the horizontal, Ra can be calculated according to equation 2.10 [35]:

$$Ra = \frac{gp^2 c_p d^3 M^2 \Delta T}{\mu \lambda R^2 T^3} \cos\beta \tag{2.10}$$

Descriptively, Ra describes the ratio of weight, buoyancy and friction, which are the three forces that are involved in the emergence of free convection [36]. If $Ra > 1708$, natural convection occurs [37]. For the description of forced convection, the Reynolds number Re is used, which expresses the ratio of inertial forces against viscous force.

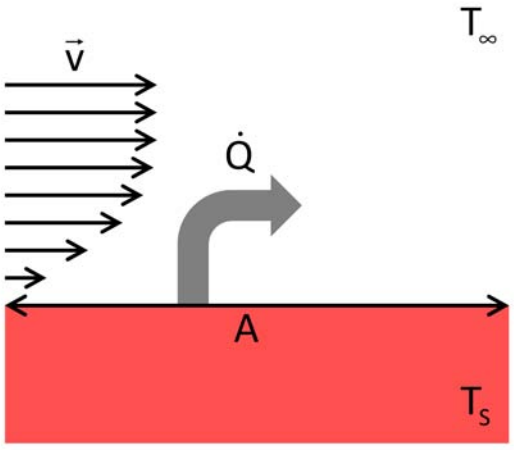

Figure 2.2: Cooling of a hot solid by forced convection.

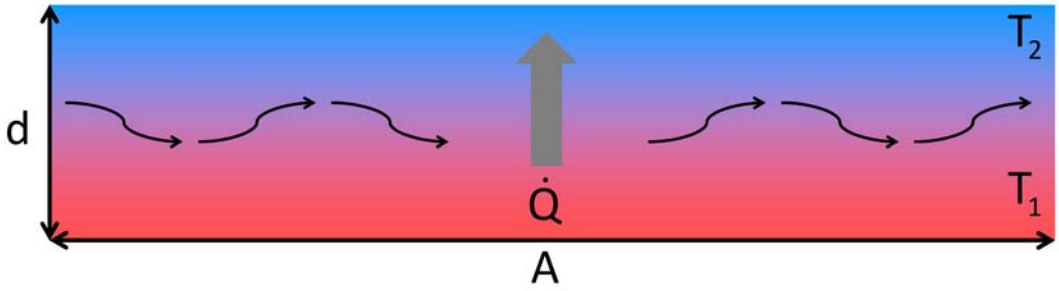

Figure 2.3: Heat transfer through a fluid layer.

2.3 Radiation

Radiative heat transfer is based on the exchange of electromagnetic waves (or photons) between atoms or molecules. Therefore, this mode of heat transport can also occur in vacuum (unlike conduction and convection, which require a transfer medium) and proceeds at the speed of light. In general, the emission of electromagnetic waves can be connected to various reasons, for example low-frequency waves due to electric dipole oscillations or gamma radiation as a result of radioactive decay. For heat transport, one is particularly interested in the thermal radiation emitted by a body due to its temperature [28]. One defines an idealized body, called blackbody, which is a perfect emitter and absorber of radiation. The blackbody spectral irradiation power $I_{b\lambda}$, which is the amount of emitted radiation energy at a given wavelength λ and temperature T per unit time, per unit area and per unit wavelength, is given by Planck's law [28]:

$$I_{b\lambda} = \frac{2\pi hc^2}{\lambda^5 \left(\exp\left(hc/\lambda k_B T\right) - 1\right)} \tag{2.11}$$

The natural constants in this equation are the Planck constant $h = 6.6261 \cdot 10^{-34}$ Js, the Boltzmann constant $k_B = 1.3807 \cdot 10^{-23}$ J/K and the speed of light $c = 2.9979 \cdot 10^{8}$ m/s. Figure 2.4 shows the blackbody spectral irradiation power for different temperatures.

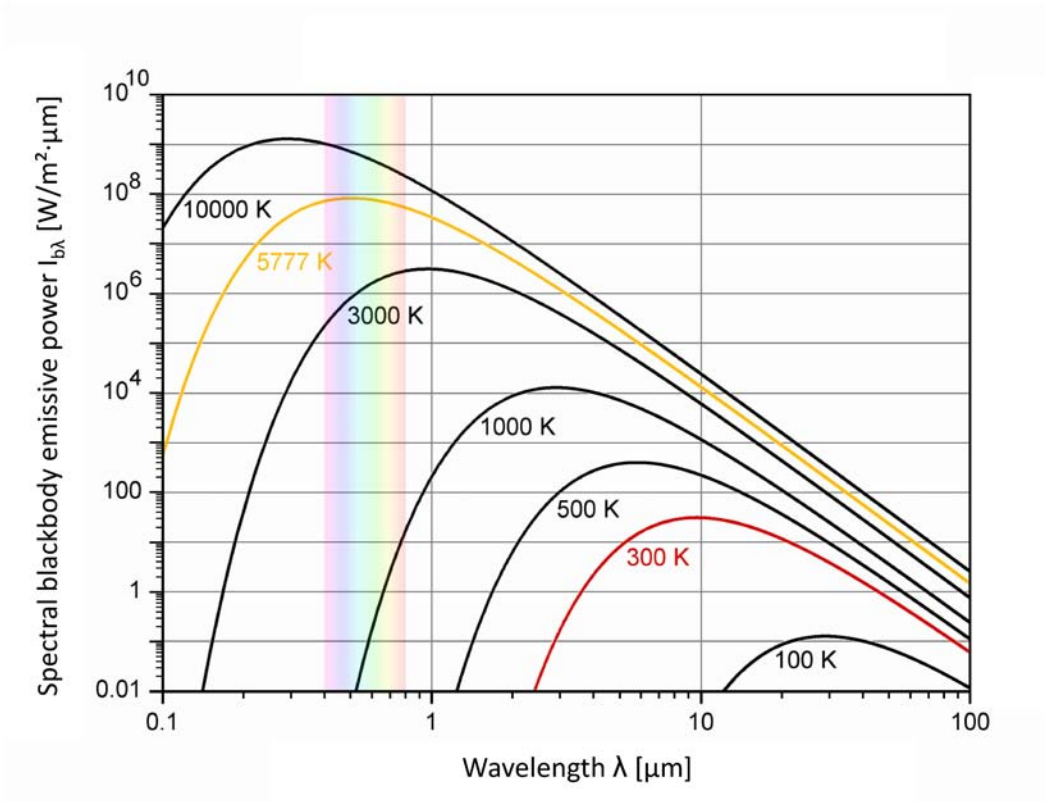

Figure 2.4: Blackbody emission spectra at different temperatures [29]. The curve with $T = 5777\,\mathrm{K}$ corresponds to the sun's surface.

By integration over the whole wavelength spectrum [11], one obtains the Stefan-Boltzmann law, which describes the total amount of eradiated power from a surface A as a function of its temperature:

$$P = \varepsilon \sigma A T^4 \tag{2.12}$$

Here, $\sigma = 5.6704 \cdot 10^{-8}\ \mathrm{W/m^2K^4}$ is the Stefan-Boltzmann constant and ε denotes the emissivity, which is defined as the total amount of radiation emitted by a given surface of temperature T divided by the radiation of a blackbody at the same temperature. As a consequence, $\varepsilon = 1$ for the blackbody whereas $\varepsilon < 1$ for all real surfaces.

Since matter does not only emit, but also absorb radiation, another important quantity is the absorptivity α, which is the fraction of incident radiation that is absorbed by a surface. Both emissivity and absorptivity are temperature- and wavelength-dependent in general. According to Kirchhoff's law, ε and α are equal at a given temperature and wavelength:

$$\varepsilon(\lambda, T) = \alpha(\lambda, T) \tag{2.13}$$

Another equation that can be derived from Planck's law is Wien's displacement law. It states that the wavelength λ_{max}, at which the irradiated intensity attains its maximum value (see figure 2.4), is inversely proportional to the temperature:

$$\lambda_{max} = \frac{2897.8\,\mu\mathrm{m\,K}}{T} \tag{2.14}$$

For the sun with an effective surface temperature of 5777 K, the intensity maximum is at $\lambda_{max} \approx 500$ nm, which corresponds to green visible light. Bodies at room temperature have their maximum in the infrared regime: $\lambda_{max}\,(T = 300\ \mathrm{K}) \approx 10\ \mu\mathrm{m}$.

As an example, consider the general case of radiative heat transport between two opaque surfaces with different sizes, emissivities and temperatures (figure 2.5). Both surfaces emit radiation according to their area A, emissivity ε and temperature T as expressed by the Stefan-Boltzmann law (equation 2.12). In addition, both surfaces absorb, transmit and reflect fractions of incident radiation. These fractions are denoted with α, τ and ϱ. From energy conservation, one can derive $\alpha + \tau + \varrho = 1$. For opaque surfaces, $\tau = 0$ and thus $\varepsilon + \varrho = 1$, where α is replaced by ε due to Kirchhoff's law. Furthermore, one has to introduce a view factor F_{12}. It describes the fraction of radiation leaving surface 1 (by emission or reflection) which arrives directly (without intermediate reflection) at surface 2 (and gets absorbed or reflected there). View factors only depend on the geometry of the problem. The factors F_{12} and F_{21}, which describe the energy flux in opposite directions are related via $A_1 F_{12} = A_2 F_{21}$. Therefore, the radiation exchange can be calculated from the view of either surface. If $T_1 > T_2$ without loss of generality, the net heat flow $\dot{Q}_{12}$ has a positive value and is given by [28]:

$$\dot{Q}_{12} = \sigma \left(T_1^4 - T_2^4\right) \left(\frac{1-\varepsilon_1}{A_1 \varepsilon_1} + \frac{1}{A_1 F_{12}} + \frac{1-\varepsilon_2}{A_2 \varepsilon_2}\right)^{-1} \tag{2.15}$$

A more specific case with large practical relevance is the radiation exchange between parallel plates (figure 2.6) with $A = A_1 = A_2$. If A is large enough compared to the distance d between the plates, the view factor approaches $F_{12} = 1$. The heat flux is then given by

$$\dot{Q}_{12} = \sigma A \left(T_1^4 - T_2^4\right) \left(\frac{1}{\varepsilon_1} + \frac{1}{\varepsilon_2} - 1\right)^{-1} = \varepsilon_{eff} \sigma A \left(T_1^4 - T_2^4\right) \tag{2.16}$$

with ε_{eff} denoting the effective emissivity defined as:

$$\varepsilon_{eff} = \left(\frac{1}{\varepsilon_1} + \frac{1}{\varepsilon_2} - 1\right)^{-1} \tag{2.17}$$

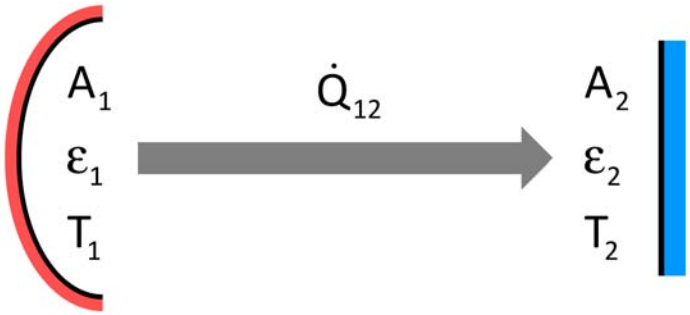

Figure 2.5: Radiative heat transport between arbitrary surfaces.

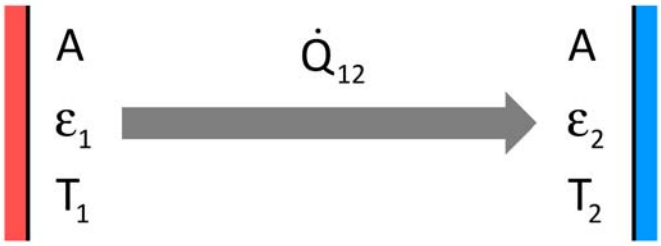

Figure 2.6: Radiative heat transport between parallel plates.

Chapter 3

Overview: Insulation Techniques

Thermal insulations have numerous fields of application in technology and in everyday life. The reduction of a heat flux is often required to slow down the temperature change of a system, to reduce the heating or cooling power that is needed to keep it at a certain temperature or to decouple it from its surroundings. In general, three major insulation techniques can be distinguished, which differ regarding their functionality, effort and insulation performance. A brief introduction of each of them is given in this chapter.

3.1 Conventional Insulation Materials

The insulating properties of conventional insulation materials are based on the confinement of air by a porous solid, which can be a granular, fibrous or foamed material. The heat transport within these materials is a combination of solid and gaseous conduction. Convection is suppressed inside the small pores, as the emerging buoyancy forces do not exceed friction ($Ra \ll 1$ for typical values, compare equation 2.10), and radiation is blocked by the opaque solid. The heat conductivities of commonly used materials are listed in table 3.1, some of these materials are shown in figure 3.1. A remarkable class of materials are aerogels [38, 39, 40, 41, 42], which can reach thermal conductivities around $\lambda = 0.02$ W/mK as a result of their high porosity and small pore size (see section 4.1).

In practice, one defines the heat transfer coefficient (also called k-value) for a given insulation, which includes both the thermal conductivity of the material and the insulation thickness d:

$$H_i = \frac{\lambda}{d} = \frac{\dot{Q}}{A\,(T_1 - T_2)} = \frac{\dot{q}}{\Delta T} \tag{3.1}$$

A lower value indicates a better suppression of the heat flux by the insulation. When materials with a lower thermal conductivity are used, the insulation thickness can be reduced to obtain the same heat transfer coefficient, which is often desired in practice due to space-saving.

material	λ [W/mK]
perlite	0.05...0.07
foam glass	0.04...0.05
rock wool	0.032...0.045
polystyrene	0.03...0.05
polyurethane	0.024...0.035
aerogels	0.013...0.02

Table 3.1: Thermal conductivities of selected insulation materials at ambient pressure. The values are taken from [43, 44].

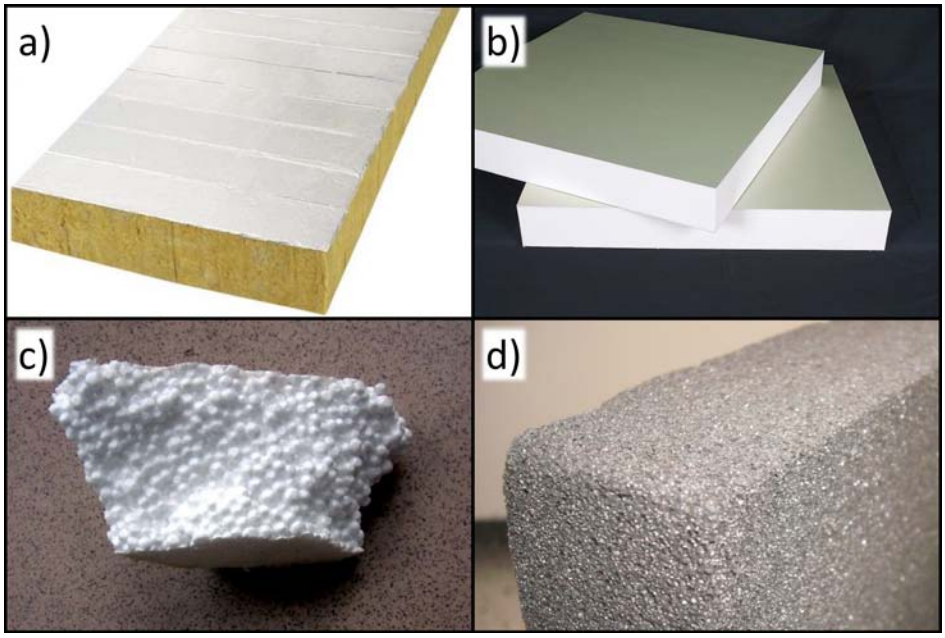

Figure 3.1: Conventional insulation materials: rock wool (a), polyurethane (b), polystyrene (c) and foam glass (d) [45, 46, 47, 48].

3.2 Vacuum Insulation

A vacuum insulation is realized by evacuating the empty space between two walls. As mentioned in chapter 2, the only heat transfer mechanism that can occur in vacuum is radiation. In practice, gas conduction will also happen to a very small amount, because a perfect vacuum cannot be generated. However, this effect can be neglected if the pressure is sufficiently low (see section 4.1 for details).

Therefore, the rate of heat exchange is in general given by equation 2.15. Consider now the special case of a cylindrical vacuum flask (also called Dewar flask, see figure 3.2), which is a very common application for vacuum insulation. Because the inner vessel is convex and completely surrounded by the outer surface, the view factor is equal to $F_{12} = 1$. As a consequence, the heat transport is given by:

$$\dot{Q}_{12} = \sigma A_1 \left(T_1^4 - T_2^4\right) \left[\frac{1}{\varepsilon_1} + \frac{1-\varepsilon_2}{\varepsilon_2}\left(\frac{A_1}{A_2}\right)\right]^{-1} \tag{3.2}$$

If the content of the vessel is colder than its surroundings, $\dot{Q}_{12}$ has a negative value, because the direction of the heat flux is in fact reversed. Equation 3.2 is also valid for the case of concentrical spheres with surfaces A_1 and A_2. A planar geometry is covered by equation 2.16.

To reduce the amount of exchanged heat, one would ideally use surfaces with low emissivities. Some materials fulfill this requirement innately, for example aluminum with $\varepsilon_{Al} = 0.04$ [31]. For the rest, a low ε can be achieved by surface coating. Additional heat loss mechanisms in practice are solid conduction in the upper part of the flaks, where the closure is located (figure 3.2 b), or direct thermal contact of the liquid gas with environmental air (figure 3.2 c).

Because radiation is not attenuated in vacuum, a special property of vacuum insulation is the fact that the radiative heat transfer is independent of the thickness d of the spacing. Thus, the gap size can be only a few millimeters (see figure 3.2 b), which comes to advantage in applications where space-saving is an issue. On the contrary, vacuum insulation can be unfavorable in the case of high temperatures, since the radiative heat transfer increases with the fourth power of temperature.

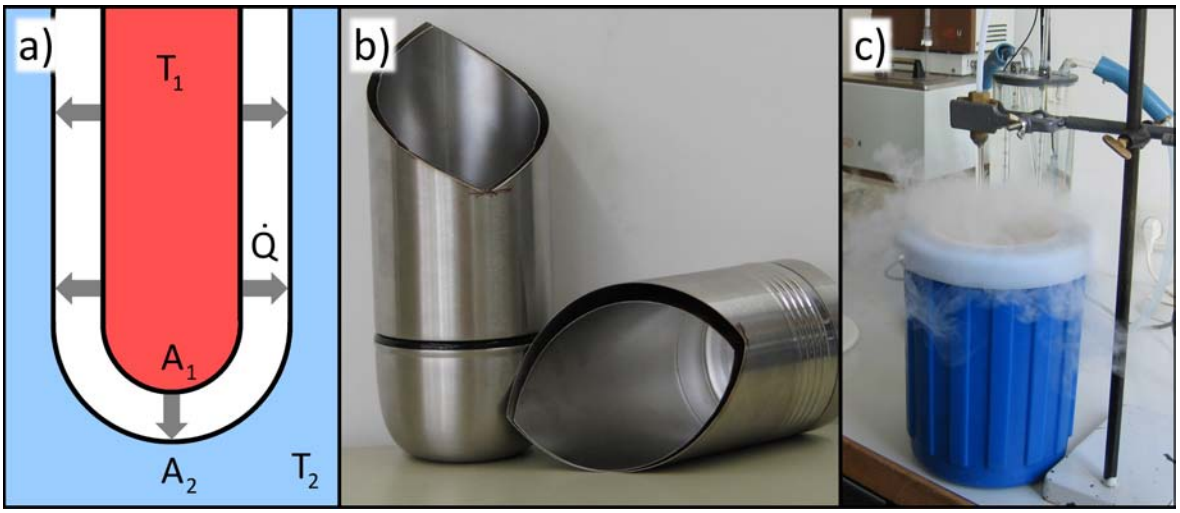

Figure 3.2: Vacuum insulation: sketch of a vacuum flask (a), sliced vacuum flask for domestic use, e.g. storage of beverages (b), Dewar flask for cryogenic applications, e.g. liquid gases (c) [49].

3.3 Vacuum Super Insulation

As mentioned in the previous section, radiation is the only significant heat transport mechanism that occurs in vacuum. To a certain extent, it can be reduced by surfaces with low emissivities. However, the radiative heat transfer can be significantly suppressed further by introducing opaque materials into the evacuated spacing of a vacuum insulation, in order to block radiation. Although solid conduction appears as an additional mode of heat transfer, the total rate of heat exchange can effectively be reduced using proper techniques. This type of insulation is called vacuum super insulation [50]. There are two types with practical relevance: foil insulation and powder insulation. Both shall briefly be described in this section. A detailed investigation of the heat transport in evacuated powder insulations will be made in chapter 4.

3.3.1 Foil Insulation

Beginning from the heat transfer between two parallel plates (figure 3.3 a), which is described by equation 2.16, consider the case where a single foil is introduced into the evacuated gap (figure 3.3 b). For the sake of simplicity, let the surface areas A of both plates and all foils be equal and let A be large enough to neglect boundary effects, so that all view factors are equal to $F_{ij} = 1$. In addition, let all surfaces initially be blackbodies: $\varepsilon_1 = \varepsilon_2 = ... = \varepsilon_N = 1$. The following considerations are equally valid for the radiation heat flux $\dot{Q}_1$, which is directed from the hotter towards the colder plate, for $\dot{Q}_2$, which has opposite direction, and thus also for the net heat flux $\dot{Q}_{12}$, which is the difference of both.

The radiation power $\dot{Q}_1$ being directed from left to right is absorbed by the foil, which heats up until equilibrium is reached, i.e. the emitted and the absorbed radiation power are equal. However, the irradiation of the foil happens homogeneously into both directions. Therefore, only half of the incoming heat flux arrives at the cold plate, whereas the other half is radiated back towards the hot plate. The effective heat flux from left to right $\dot{Q}_{1\,eff}$ (indicated by the green arrows in figure 3.3) is thus reduced by a factor of 2. If additional foils are introduced, the radiation power that reaches the cold plate is further decreased. By inserting 2 foils (figure 3.3 c), $\dot{Q}_{1\,eff}$ is reduced by a factor of 3 in thermal equilibrium. For the general case of N foils, the reduction factor is given by $N + 1$ (see figure 3.3 d).

The above arguments remain valid for real surfaces with emissivities $\varepsilon < 1$. In typical applications, all surfaces are identical: $\varepsilon_1 = \varepsilon_2 = ... = \varepsilon_N = \varepsilon < 1$. The net heat flux $\dot{Q}_{12}$ is then given by:

$$\dot{Q}_{12} = \frac{\sigma A \left(T_1^4 - T_2^4\right)}{\left(\frac{2}{\varepsilon} - 1\right)(N + 1)} \tag{3.3}$$

Comparison with equation 2.16 shows again that introducing N foils suppresses the radiative heat flux by a factor of $N + 1$.

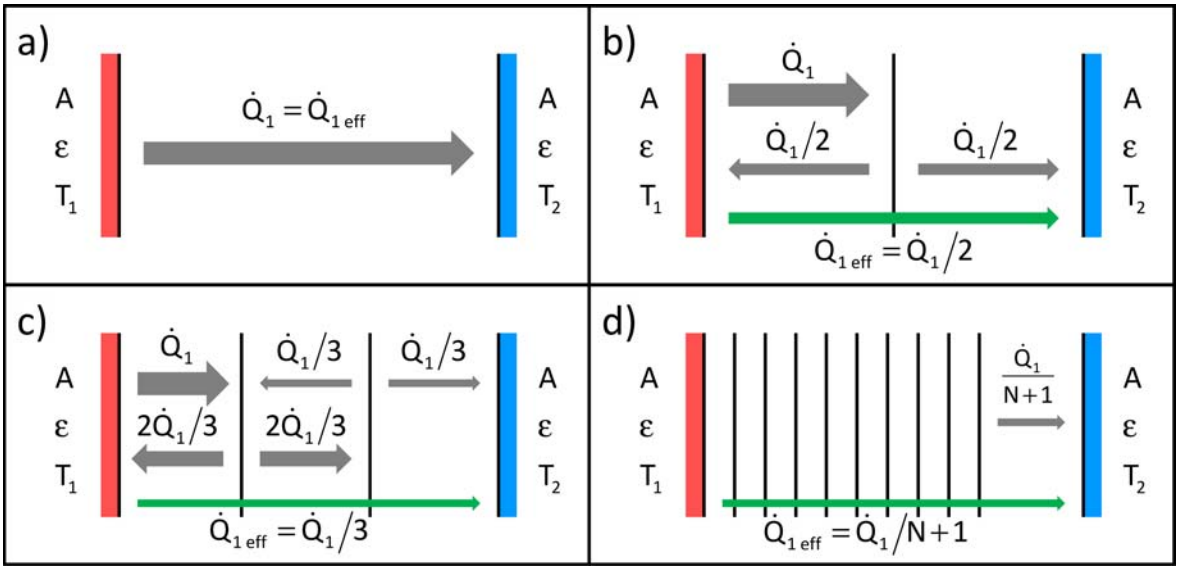

Figure 3.3: Principle of foil insulation: Due to the fact that the eradiation from the foils is always homogeneously emitted into both directions, the effective heat flux is reduced with increasing number of foils. Image d) only shows the heat flux between the last foil and the cold plate, which is always equal to $\dot{Q}_{1\,eff}$. To avoid confusion, only the arrows connected to the heat flux $\dot{Q}_1$, which emerges at the hot plate, are drawn. However, the situation is exactly analog for $\dot{Q}_2$, which is eradiated from the cold plate, and as well for the net heat flux $\dot{Q}_{12} = \dot{Q}_{1\,eff} - \dot{Q}_{2\,eff}$.

The most important application of foil insulation is in spacecraft engineering, because thermal losses of satellites and space vehicles in the orbit are almost only due to radiation. The technique is also often called multilayer insulation in this context [51, 52] and is mainly necessary to keep on-board electronic devices at an operating temperature of around 20 °C. For this purpose, plastic foils with a thickness of only a few micrometers are coated with a thin metal layer (silver, aluminum or gold). The layers are separated by a mesh made of cloth or synthetic materials (figure 3.4 a). Despite of the resulting solid conduction, the effective total heat flux can be reduced by a factor of around 300 using 30 to 40 layers with surface emissivities below $\varepsilon = 0.05$ [52].

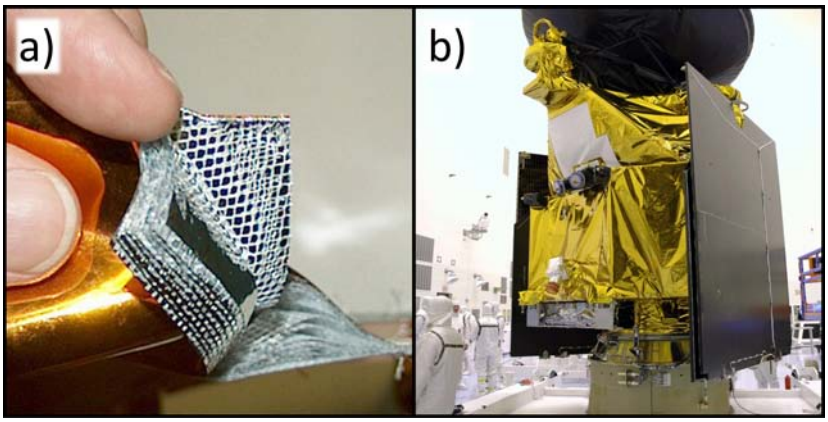

Figure 3.4: Foil insulation: Closeup view (a), Mars Reconnaissance Orbiter covered with multilayer insulation (b) [51, 52].

3.3.2 Powder Insulation

In a very similar way to the multilayer insulation described above, also a powder can reduce the radiative heat transfer between two surfaces. The powder grains absorb and re-emit radiation just like foils. The only major difference is, that due to the spherical shape of the grains, the emitted radiation will be homogeneously distributed into all spatial directions. In contrast, flat foils only emit into the two directions perpendicular to their surface.

It still has to be mentioned that a vacuum super insulation could in principal be realized by evacuating any conventional insulation material. Experiments with rockwool [21] have shown that the results differ only slightly from powders due to different pore sizes and porosities. However, using powders is often less complicated in practice, also compared to multilayer insulations. Whereas spacecraft applications naturally take place in evacuated space, the vacuum inside a gap-shaped leakproof enclosure has to be generated artificially for applications on earth. Filling a powder or a similar bulk material into this gap prior to evacuating is often easier than installing plates of conventional insulation materials or a multilayer insulation there. For this reason, also the vacuum super insulation of the long-term hot water storage, which is newly developed in the context of this thesis, is realized using a perlite powder. Due to its granular structure, the material is self-adapting to any arbitrary geometry.

Chapter 4

Heat Transport in Evacuated Powder Insulations

As the previous chapters contained a general overview about heat transfer and the presentation of different insulation techniques, now the physics of heat transport in a powder-based vacuum super insulation is treated. In the framework of this thesis, this technique is applied to hot water storages. There are four mechanisms which contribute to the heat transfer inside the evacuated powder: gaseous conduction, solid conduction, radiation and the coupling effect. Each of them will be described below. Additionally, the utilization of insulating inert gases (section 4.1) and the influence of moisture within the material (section 4.6) will be addressed from a theoretical point of view.

4.1 Gas Heat Conduction and Smoluchowski Effect

Consider a gas enclosed between two walls of different temperatures and an imaginary plane at position x_0 (figure 4.1). The number of gas molecules per unit time per unit area that cross the plane in one direction is given by $n\overline{v}/6$, where n is the particle density and $\overline{v}$ is their average velocity according to the Maxwell-Boltzmann distribution. The factor $1/6$ is due to the fact that particle motion is possible in all three dimensions of space with a positive and a negative direction for every dimension. The mean distance which the molecules can travel freely between collisions with other particles is called mean free path l_f. Since both the distance between the walls and the gas density are assumed to be very large, collisions with the boundary walls can be neglected compared to the number of gas-gas-collisions. The thermal energy $E = k_B T/2$ of the particles is a function of their temperature, and as temperature varies along the x-direction, also E depends on x. Molecules crossing the plane from the left have the mean energy $\bar{E}_{lr} = E(x_0 - l_f)$, because their last collision was at an average distance l_f from the plain. In analogy, particles from the right carry the average thermal energy $\bar{E}_{rl} = E(x_0 + l_f)$.

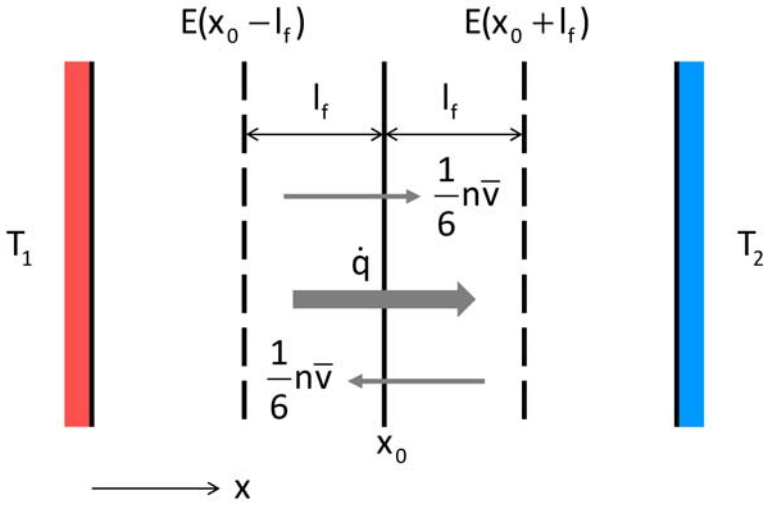

Figure 4.1: Heat conduction according to the kinetic theory of gases.

The net heat transport across the plain can be expressed as

$$\begin{aligned}
\dot{q}_{net} &= \dot{q}_{lr} - \dot{q}_{rl} \\
&= \frac{1}{6} n\bar{v} E(x_0 - l_f) - \frac{1}{6} n\bar{v} E(x_0 + l_f) \\
&= \frac{1}{6} n\bar{v} \left(E(x_0) - l_f \frac{\partial E}{\partial x} - E(x_0) - l_f \frac{\partial E}{\partial x} \right) \\
&= -\frac{1}{3} n\bar{v} l_f \frac{\partial E}{\partial T} \frac{\partial T}{\partial x} = -\frac{1}{3} \rho c_V \bar{v} l_f \frac{\partial T}{\partial x}
\end{aligned} \tag{4.1}$$

with ρ denoting the mass density and c_V the specific heat capacity of the gas. By comparison with the Fourier law of heat conduction (equation 2.1), one obtains the following relation for the thermal conductivity of gases [21, 53]:

$$\lambda_g = \frac{1}{3} n\bar{v} l_f \frac{\partial E}{\partial T} = \frac{1}{3} \rho c_V \bar{v} l_f \tag{4.2}$$

In the idealized case, where the distance d between the boundary walls is very large, the mean free path l_f is only related to the frequency of collisions between gas molecules. However, in reality the influence of the walls may become noticeable. One introduces a characteristic length d_c, which is given by the distance of the system boundaries. For example, the characteristic length of a gas inside a porous material is related to the average pore diameter. For the above geometry of two parallel plates, d_c is simply the distance between the plates. As an additional quantity, one defines the dimensionless Knudsen number Kn as the ratio between mean free path and characteristic length:

$$Kn = \frac{l_f}{d_c} \tag{4.3}$$

Expressed by the Knudsen number, three different regimes of gas heat conduction can be distinguished:

A) Continuum ($Kn \ll 1$): Collisions with the boundary walls become negligible if $d_c \gg l_f$, which corresponds to $Kn \ll 1$. This is exactly the previously described case, where the heat conductivity is given by equation 4.2. From the kinetic theory of gases [53], it is known that the mean free path is inversely proportional to the particle (and mass) density: $l_f \sim n^{-1} \sim \rho^{-1}$. The expression for λ_g contains the product ρl_f and the quantities c_V and $\bar{v}$, which do not depend on pressure for an ideal gas. As a first important result, it follows that the thermal conductivity is independent of gas pressure. The heat transport for $Kn \ll 1$ is also referred to as heat diffusion, because it is only related to collisions of gas molecules along their random walk.

B) Free Molecular Flow / Knudsen Flow ($Kn \gg 1$): In the opposite case with $d_c \ll l_f$, which for example occurs at low gas pressures or small pore diameters, the collisions between the molecules can be neglected. Thus, thermal energy is directly transferred between the boundary walls. This situation is also called ballistic transport. Equation 4.2 is still valid, but l_f has to be replaced by d_c, which is the new effective distance that particles can travel before they hit the walls. Because d_c is a constant, but the term for λ_g still includes the density ρ, which is proportional to the gas pressure, the thermal conductivity becomes a linear function of pressure. In a perfect vacuum, λ_g approaches zero, and gaseous conduction is suppressed.

C) Transition Regime ($Kn \approx 1$): Whereas the limiting cases above could be treated straight-foreward, the discussion of gas heat conduction in the transition range between continuum and free molecular flow becomes rather complicated. In a detailed investigation of gas conduction in evacuated solar thermal collectors, different calculation approaches have been collected and discussed [35]. The most general method is solving the Boltzmann transport equation [54], which is connected to a considerable calculatory effort. Analytical solutions are only known for simple geometries and within narrow pressure and temperature intervals. Another possibility is the temperature-jump method, which assumes Fourier's law to be valid also in the transition regime, but at the same time uses different boundary conditions at the walls. In its original form, this method was applicable only in the region of $Kn < 0.1$ [55]. A modified version of the temperature-jump method has been developed, which is valid for a significantly larger range of Knudsen numbers, but requires the solution of the heat equation with mixed boundary conditions [35]. Finally, a simple and heuristic equation derived from experimental data is known, which interpolates the thermal conductivity in the transition regime [34, 56]:

$$\lambda_g = \frac{\lambda_0}{1 + 2\beta_S Kn} = \frac{\lambda_0}{1 + \frac{p_{1/2}}{p}} \tag{4.4}$$

Here, λ_0 is the heat conductivity in the continuum, and $p_{1/2}$ is the characteristic pressure at which λ_g reaches half of the continuum value. β_S is an experimentally determined constant. For air, the values are $p_{1/2} = 230\,\mathrm{mbar}/\left(d_c\,[\mu\mathrm{m}]\right)$ and $\beta_S = 1.6$ [57].

Equation 4.4 is known as Sherman interpolation. It is equal to the temperature-jump method and exact only for one-dimensional geometries [35]. For other geometries, it is a practical approximation, whereas the temperature-jump method recently could be expanded also to arbitrary geometries [35].

The gas heat conductivity of air as a function of pressure is shown in figure 4.2. For high pressures, one can identify the continuum where λ_g becomes constant. In the opposite case of Knudsen flow, the heat conductivity is proportional to the pressure, which is equivalent to an exponential curve in the logarithmic plot. The position of the transition regime is determined by the Knudsen number, which includes both the characteristic length and the mean free path that is connected to gas pressure. Therefore, one obtains different curves for different values of d_c, and the choice of d_c determines the gas heat conductivity at a given pressure. As an example, four values for the characteristic length are shown in the diagram. In general, the reduced heat conductivity of gases under the influence of boundary walls is referred to as Smoluchowski effect, named after Marian Smoluchowski, who was the first to study the phenomenon experimentally and theoretically [58, 59].

The temperature dependency of the continuum thermal conductivity λ_0 can also be derived from equation 4.2. Again, ρ and l_f cancel due to their inverse proportionality, and the specific heat c_V is constant for an ideal gas. An expression for the average velocity $\bar{v}$ is obtained [53] by integrating over the Maxwell-Boltzmann distribution $F(v)$. Consequently, one arrives at:

$$\lambda_0 \quad = \quad \frac{1}{3}\rho c_V \bar{v} l_f \sim \bar{v} \sim \sqrt{T} \qquad \text{with} \quad \bar{v} = \frac{1}{n}\int_0^\infty F(v) v dv = \sqrt{\frac{8 k_B T}{\pi m}} \tag{4.5}$$

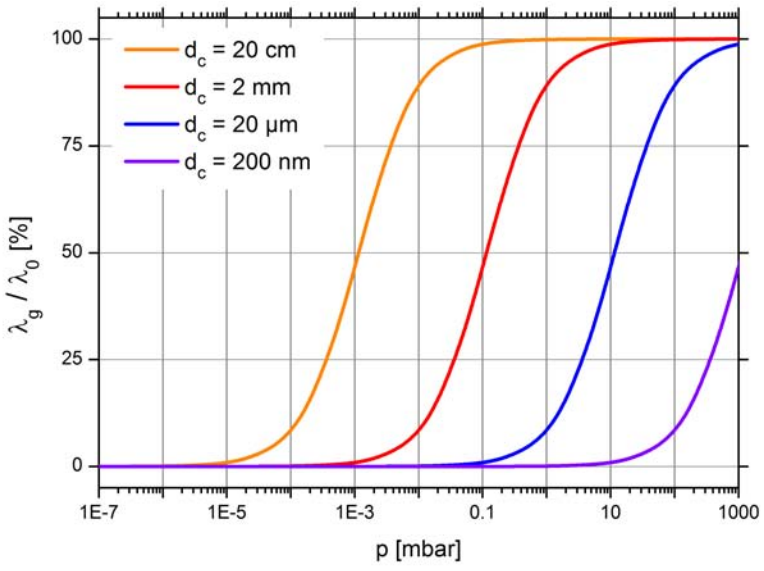

Figure 4.2: Pressure dependency of the thermal conductivity of air enclosed in cavities with different dimensions d_c, normalized to the continuum value $\lambda_0 = 0.026\,\mathrm{W/mK}$.

One could have also obtained the relation $\bar{v} \sim \sqrt{T}$ from $\bar{E} = \frac{1}{2}k_B T = \frac{1}{2}m\bar{v^2}$. However, this derivation is somewhat sloppy, because the mean square speed $\bar{v^2}$ has to be distinguished from the squared average speed $\bar{v}^2$ is ignored. Actually, $\bar{v^2}$ and $\bar{v}^2$ differ from each other only by a constant factor of $8/3\pi$, which does not matter for the temperature-dependency. But this fact can only be derived from integrating both v and v^2 over the Maxwell-Boltzmann distribution. Therefore, the integral has to be calculated anyway.

Up to now, general properties of the thermal conductivity of gases and their dependencies on pressure and temperature have been discussed. In the following, some more specific aspects are presented, which may become relevant under practical conditions. First of all, an important relation is obtained from a closer look at the different quantities that determine the heat conductivity of a gas according to equation 4.2:

$$\lambda_g = \frac{1}{3}\rho c_V \bar{v} l_f \sim \frac{f}{\varsigma\sqrt{M}} \tag{4.6}$$

$$\text{with} \qquad \rho \sim M \qquad c_V \sim \frac{f}{M} \qquad \bar{v} \sim \frac{1}{\sqrt{M}} \qquad l_f \sim \frac{1}{\varsigma}$$

As a consequence, gases with a high cross section ς for collisions, a high molar mass M and few degrees of freedom f have lower thermal conductivities. All three requirements are fulfilled for the inert gases argon, krypton and xenon. These gases consist of only one atom. Therefore, degrees of freedom due to rotation and oscillation are not existent, and only the three degrees of freedom connected to translational motion are available. In addition, the atoms are relatively heavy and have a large effective diameter, which is especially valid for krypton and even more for xenon. The resulting low continuum heat conductivities and other relevant properties of these gases are listed in table 4.1. For comparison, the values for air have also been included.

	Air	Argon	Krypton	Xenon
M [g/mol]	14.007	39.948	83.798	131.293
r_W [pm]	155	188	202	216
f [1]	6	3	3	3
λ_0 [10^{-3} W/mK] at $T = 25\,°C$	26.1	17.7	9.5	5.6
α_{HGS}	0.83	1	0.5	0.55
α_{Al}	0.95	0.34	0.5	0.4

Table 4.1: Selected properties of argon, krypton and xenon compared to air: molar mass M, van der Waals radius r_W, number of degrees of freedom f, continuum heat conductivity λ_0 and accommodation coefficients α for high-grade steel and aluminum. For air, the values of M, r_W and f refer to pure nitrogen [34, 35, 44, 66, 67, 68, 69].

From a more detailed investigation [35] based on the temperature-jump method according to [55] and [58], one can derive equation 4.7, which describes the gas heat conductivity in a very explicit way. It contains the pressure dependency according to equation 4.4, the temperature dependency from equation 4.5 and also includes the parameters f, ς and M from equation 4.6:

$$\lambda_g\left(p,T\right)=\frac{\sqrt{\frac{RT}{8\pi M}}}{\frac{16\sqrt{2}\varsigma}{5\pi k_B(2f+9)}+\frac{T}{pd_c\alpha_{red}(f+1)}} \tag{4.7}$$

In addition to the already defined quantities, the gas constant $R = 8.31\,\mathrm{J/K\,mol}$ and the reduced accommodation coefficient α_{red}, which shall be explained later, occur in this term. For the limiting case of $p \to \infty$, which corresponds to the continuum, one can neglect the second summand in the denominator to obtain equation 4.8, which is a more precise version of equation 4.6:

$$\lambda_g \sim \frac{(2f+9)\sqrt{T}}{\varsigma\sqrt{M}} \tag{4.8}$$

In the opposite situation where $p \to 0$, the first addend can be ignored, which yields:

$$\lambda_g \sim \frac{p\alpha_{red}\,(f+1)}{\sqrt{MT}} \tag{4.9}$$

In this case of ballistic heat transport, the interactions between molecules can be neglected compared to collisions with the boundary walls (see page 25). It is therefore comprehensible that the cross section ς for intermolecular collisions does no longer matter. Instead, an accommodation coefficient α occurs, which describes the interaction with the walls. It is defined as:

$$\alpha=\frac{T_{out}-T_{in}}{T_{wall}-T_{in}} \tag{4.10}$$

If the incoming particles with temperature T_{in} adopt the wall temperature completely, which means $T_{out} = T_{wall}$ after the collision, the accommodation coefficient is $\alpha = 1$. The situation where there is no temperature exchange at all ($T_{out} = T_{in}$) is described by an accommodation coefficient of $\alpha = 0$. The intermediate cases are expressed by $0 < \alpha < 1$, according to how big the temperature change is. The coefficients for a specific gas vary for different wall materials. As an example, the values for nitrogen, argon, krypton and xenon in combination with high-grade steel and aluminum are listen in table 4.1.

For the usual case where a gas is enclosed between two parallel plates with accommodation coefficients α_1 and α_2, the reduced accommodation coefficient has to be used to include the interaction with both walls:

$$\alpha_{red}=\frac{\alpha_1\alpha_2}{\alpha_1+\alpha_2-\alpha_1\alpha_2} \tag{4.11}$$

If the surface areas of the boundary walls are not equal, for example in cylindrical geometries, the reduced accommodation coefficient in equation 4.9 has to be replaced by the area-asymmetric accommodation factor $\hat{f}(\alpha_i, A_i)$ to correct the errors of the standard temperature-jump method at low gas pressures. An expression for $\hat{f}(\alpha_i, A_i)$ was first derived by [70]:

$$\hat{f}(\alpha_i, A_i) = \left[\frac{1}{A_1\alpha_1} + \frac{1}{A_2}\left(\frac{1}{\alpha_2} - 1\right)\right]^{-1} \tag{4.12}$$

Putting everything together, the thermal conductivity of the inert gases argon, krypton and xenon is lower compared to nitrogen not only in the continuum, but also in the regime of free molecular flow due to beneficial accommodation coefficients, a high molar mass and a low number of degrees of freedom. This fact has also been confirmed experimentally [35]. On a sidenote, this does not automatically have to be true. For example, sulfur hexafluoride SF_6 has a lower heat conductivity than nitrogen in the continuum because of its high mass and large diameter. However, in the Knudsen regime, its thermal conductivity is higher. This is a result of disadvantageous accommodation coefficients and the high number of degrees of freedom ($f_{SF_6} = 19$), which are weighted differently in the regime of free molecular flow (factor $2f + 9$ versus $f + 1$, see equations 4.8 and 4.9).

In practical applications with evacuated powder insulations, it may be reasonable to replace air with an inert gas, for example if the vacuum pressure that is necessary for a complete suppression of gaseous conduction cannot be maintained because of technically unavoidable leakages. In this case, the insulating properties of inert gases described above can be utilized. In real applications, due to the entrance of air through the leakage, a gas mixture will be present though, and the fraction of air will increase with time. It is known [71] that the thermal conductivity of gas mixtures can be expressed by the following formula if the pressure is in the continuum regime for both gases:

$$\lambda_{tot} = \frac{\lambda_1 p_1 + \lambda_2 p_2}{p_1 + p_2} = \frac{\lambda_1 \frac{p_1}{P_2} + \lambda_2}{\frac{p_1}{p_2} + 1} \tag{4.13}$$

λ_i and p_i are the continuum heat conductivities and the partial pressures of the single components. The combined thermal conductivity λ_{tot} only depends on the ratio of partial pressures. In a logarithmic plot, one obtains an S-shaped curve, which is shown in fig. 4.3 for a mixture of air and krypton.

Although the thermal conductivity of inert gases is well-known, the effective heat conductivity of an evacuated perlite powder insulation under the influence of argon and krypton has been measured in the experimental part of this thesis (section 6.3). The main motivation of these measurements was to verify the demonstrated effects for perlite and to investigate the coupling effect for inert gases.

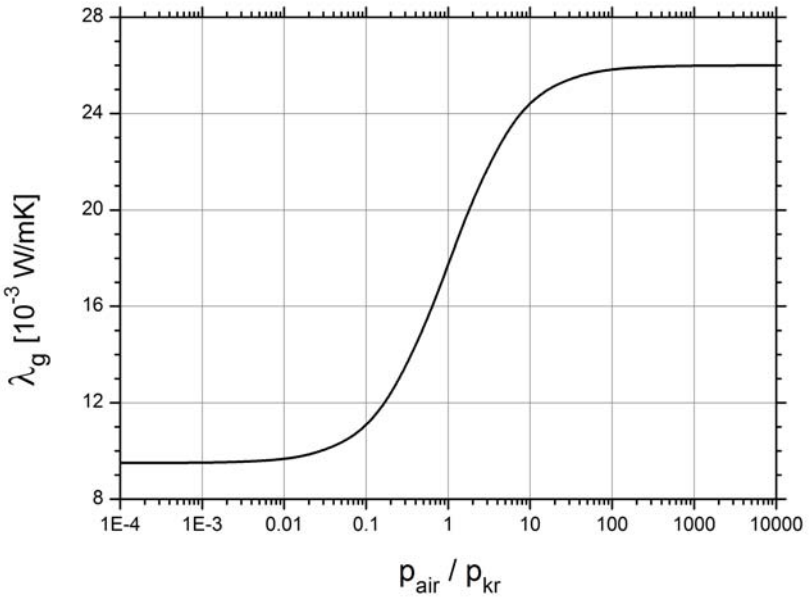

Figure 4.3: Total thermal conductivity of a gas mixture of air and krypton in the continuum at $T = 25\,°\mathrm{C}$ as a function of partial pressure ratio [71].

4.2 Solid Heat Conduction

As mentioned in section 2.1, conductive heat transfer in solids can be due to phonons or electrons. However, the electronic heat transport requires mobility of electrons, which is only given in metals and, to a lower extent, in semiconductors. Heat insulation materials are usually not electrically conducting, since the electrons are bound to the lattice atoms. Therefore, only the phononic heat transport occurs. For porous materials, two relevant solid heat conductivities can be distinguished. On the one hand, there is the heat conductivity λ_s^*, which describes the massive part of the solid without any effects that are related to the material structure. On the other hand, there is the effective solid heat conductivity λ_s, which takes into account the morphology of the material.

For the theoretical characterization of λ_s^*, the phononic heat transport has to be considered. From a physical point of view, one can treat phonons like an ideal gas of particles confined in the volume of the solid. As a consequence, the results from kinetic theory of gases can be transferred, and equation 4.2 is still valid if the values $\bar{v}$ and l_f are adjusted for phonons. The quantity $\bar{v}$, which previously was the mean velocity of gas molecules according to the Maxwell-Boltzmann distribution, has to be replaced by the group velocity of phonons, which is obtained from the dispersion relation. Regarding the mean free path l_f, one has to consider both phonon-phonon-scattering and scattering on defects and impurities.

In order to describe the temperature dependency of the solid heat conductivity in detail, it has to be taken into account that both the specific heat c_V of the solid and the mean free path l_f of phonons can vary with temperature [60]. For the description of c_V at

low temperatures, a quantum mechanical treatment is necessary. However, at high temperatures (room temperature), the specific heat capacity approaches the classically obtained Dulong-Petit value of $c_V = 3Nk_B/m = const.$ where N is the total number of atoms and m is the mass of the solid. Therefore, only the mean free path l_f determines the temperature dependency of the solid heat conductivity λ_s^*. At high temperatures, scattering on defects can be neglected, and only phonon-phonon scattering is relevant. As a consequence, l_f becomes inversely proportional to T [60]:

$$\lambda_s^* \sim \frac{1}{T} \tag{4.14}$$

The effective solid heat conductivity λ_s of a porous insulation material is usually much smaller than λ_s^* [10], because the morphology of these materials influences the heat transport (see figure 4.4). The heat flux (red arrow) can not always be aligned parallel to the temperature gradient and has to follow an indirect route, because the direct pathway is obstructed by the presence of pores. As an additional effect in the case of powders, the transition to an adjacent grain can only happen at the small contact area, which is pointlike in an idealized view . The combination of both effects results in small effective solid heat conductivities. In other words, there are additional thermal resistances arising from the structure of the material. A very demonstrative example for these effects is the highly-porous perlite: The two major components of this material are SiO_2 (65 to 75 %) and Al_2O_3 (10 to 15 %) with thermal conductivities of $\lambda^*_{SiO_2} \approx 1.2$ W/mK and $\lambda^*_{Al_2O_3} \approx 28$ W/mK [44]. Therefore, $\lambda^*_{perlite}$ is supposed to be in the order of 1 W/mK. Typical values for λ_s are 2 to 3 orders of magnitude lower.

It is obvious that the effective solid heat conductivity λ_s rises with higher bulk densities, because the volume ratio between massive solid and pores increases. From empirical findings, the following relation between λ_s and the bulk density ρ of the material is known:

$$\lambda_s \sim \rho^\gamma \tag{4.15}$$

The scaling parameter γ can vary between $1 \leq \gamma \leq 2$ depending on the type of material [41, 57, 61, 62].

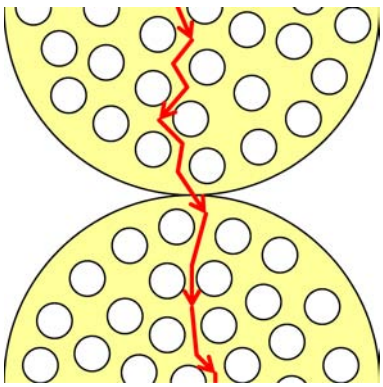

Figure 4.4: Illustration of solid conduction in a porous powder.

4.3 Radiative Heat Transfer

In section 2.3, the heat exchange between two gray surfaces due to radiation was treated, where the intermediate space between the surfaces was supposed to be evacuated. As a consequence, there was no attenuation of radiation by absorption or scattering, and thermal energy was directly transferred from one surface to the other (comparable to ballistic heat transport for gases in section 4.1).

The situation changes if the radiative heat transfer in an evacuated powder is considered, because a certain amount of radiation will be absorbed by the material. As a first assumption, one could think that the intensity I of radiation at the position x inside the medium follows the Lambert-Beer law, which describes the attenuation of (especially high-energetic) radiation as a result of absorption:

$$I_x = I_0 \exp\left(-\kappa x\right) \tag{4.16}$$

In this equation, the coefficient κ expresses the ability of the material to absorb radiation. However, it has to be said that thermal radiation is not only absorbed by the powder, but also constantly emitted due to its temperature. Therefore, equation 4.16 becomes invalid. As already mentioned in section 3.3.2, the emission is distributed homogeneously into all spatial directions. Furthermore, scattering of radiation occurs. It is therefore necessary to apply the heat diffusion model to infrared-photons. Once again, one can proceed like in section 4.1 to obtain an expression for the radiative heat transport (compare to equation 4.1):

$$\dot{q}_{net} = -\frac{1}{3} n \bar{v} l_f \frac{\partial E}{\partial T} \frac{\partial T}{\partial x} \tag{4.17}$$

Now some specifications have to be made to represent a gas of photons, which are the particles related to the exchange of electromagnetic radiation. At first, the product $n\left(\partial E/\partial T\right)$ is equivalent to the temperature derivative of the energy density u which can be obtained from Planck's law:

$$\begin{aligned}
u(T) &= \int_0^\infty u(\nu, T) d\nu = \int_0^\infty \frac{8\pi h \nu^3}{\tilde{c}^3} \frac{1}{\exp\left(\frac{h\nu}{k_B T}\right) - 1} d\nu \\
&= \frac{8\pi \tilde{n}^3 k_B^4 T^4}{h^3 c^3} \int_0^\infty \frac{x^3}{\exp(x) - 1} dx \\
&= \frac{8\pi \tilde{n}^3 k_B^4 T^4}{h^3 c^3} \frac{\pi^4}{15} = \frac{4\sigma \tilde{n}^3 T^4}{c} \\
n \frac{\partial E}{\partial T} &= \frac{\partial u}{\partial T} = \frac{16\sigma \tilde{n}^3 T^3}{c}
\end{aligned} \tag{4.18}$$

For this derivation, the spectral energy density $u(\nu, T)$ as a function of frequency ν has been used. The refractive index $\tilde{n} = c/\tilde{c}$ has been introduced, where $\tilde{c}$ is the propagation velocity of radiation inside the medium. For the evaluation of the integral, the substitution $x = h\nu/k_B T$ has been applied. The occurring constants have been combined using the Stefan-Boltzmann constant σ. The result for $\partial u/\partial T$ can be inserted into equation 4.17. With $\bar{v} = \tilde{c}$ and by expressing the mean free path l_f of phonons as the reciprocal of an extinction coefficient $E_{ex}(T)$ (see equations 4.22 to 4.28), one arrives at [10]:

$$\dot{q}_{net} = -\frac{1}{3}\frac{c}{\tilde{n}}\frac{1}{E_{ex}(T)}\frac{16\sigma\tilde{n}^3T^3}{c}\frac{\partial T}{\partial x} = \frac{16\sigma\tilde{n}^2T^3}{3E_{ex}(T)}\frac{\partial T}{\partial x} \tag{4.19}$$

In the case of diffusive radiation propagation, it is now reasonable to introduce a radiative heat conductivity λ_r by comparing equation 4.19 with Fourier's law (equation 2.1) to obtain [57]:

$$\lambda_r = \frac{16\sigma\tilde{n}^2T_r^3}{3E_{ex}(T_r)} \tag{4.20}$$

Here, T_r denotes the so-called radiation temperature, which is a mean value of the boundary temperatures T_1 and T_2 defined as:

$$T_1^4 - T_2^4 = 4T_r^3\left(T_1 - T_2\right) \quad \Rightarrow \quad T_r = \sqrt[3]{\frac{1}{4}\left(T_1^2 + T_2^2\right)\left(T_1 + T_2\right)} \tag{4.21}$$

For small temperature differences and planar geometries, T_r approaches the arithmetic mean temperature $\bar{T}_r = \frac{1}{2}\left(T_1 + T_2\right)$.

In the following, the extinction coefficient $E_{ex}(T_r)$ is described more explicitly. First, a spectral mass-specific extinction coefficient $e_\lambda^*(\lambda)$ is defined. As already mentioned above, both scattering and absorption contribute to the extinction of thermal radiation in a given material. Both mechanisms are wavelength-dependent in general. The spectral mass-specific extinction coefficient $e_\lambda^*(\lambda)$ is then obtained by adding the spectral mass-specific scattering coefficient $s_\lambda^*(\lambda)$ and the spectral mass-specific absorption coefficient $a_\lambda^*(\lambda)$ [63]:

$$e_\lambda^*(\lambda) = s_\lambda^*(\lambda) + a_\lambda^*(\lambda) \tag{4.22}$$

The quantity $e_\lambda^*(\lambda)$ can be interpreted as the fraction $I_e(x, \lambda)/I_0$ of radiation that is scattered or absorbed on its way through a thin layer of matter, divided by the mass density ρ and the layer thickness x:

$$e_\lambda^*(\lambda) = \frac{I_e(x, \lambda)}{I_0\rho x} \tag{4.23}$$

The normalization is reasonable, since the extinction will generally increase for higher values of ρ and x. Therefore, $e^*_\lambda(\lambda)$ is a material constant. The ratio $I_e(x,\lambda)/I_0$ can be expressed by the layer thickness x and the mean free path $l_f(\lambda)$ of photons:

$$\frac{I_e(x,\lambda)}{I_0} = \frac{x}{l_f(\lambda)} \tag{4.24}$$

This becomes obvious by considering some special cases: If $x = 0$, which is equivalent to the absence of a medium, radiation will not be extinguished at all, thus $I_e(0,\lambda) = 0$. For increasing values of x, the absorbed or scattered fraction will rise proportionally. If $x = l_f(\lambda)$, every incoming photon gets scattered or absorbed exactly once, and therefore the relation $I_e(l_f,\lambda)/I_0 = 1$ is valid. For $x > l_f(\lambda)$, multiple scattering or absorption and re-emission occurs, which is expressed by $I_e(l_f,\lambda)/I_0 > 1$. By inserting the relation $I_e(l_f,\lambda)/I_0 = 1$ into equation 4.23, one obtains an important correlation between the mass-specific extinction coefficient and the mean free path:

$$e^*_\lambda(\lambda) = \frac{1}{\rho l_f(\lambda)} \;\Leftrightarrow\; l_f(\lambda) = \frac{1}{\rho e^*_\lambda(\lambda)} \tag{4.25}$$

Up to now, all quantities have been functions of wavelength. In order to eliminate this dependency and to obtain average values, one has to integrate over the whole wavelength spectrum [63]:

$$\frac{1}{e^*(T)} = \frac{\int_0^\infty \frac{1}{e^*_\lambda(\lambda)} f_R(\lambda,T)d\lambda}{\int_0^\infty f_R(\lambda,T)d\lambda} \tag{4.26}$$

$$\text{with} \quad f_R(\lambda,T) = \frac{\partial I_B(\lambda,T)}{\partial I_B(T)} \tag{4.27}$$

Different wavelengths are weighted using the Rosseland function $f_R(\lambda,T)$, which is defined as the partial derivative of the spectral blackbody intensity $I_B(\lambda,T)$ at a given temperature with respect to the total intensity $I_B(T)$ irradiated at the same temperature. Therefore, the Rosseland weighting function favors wavelengths according to their fraction of occurrence within the blackbody spectrum. As a consequence, the total mass-specific extinction coefficient $e^*(T_r)$ receives a weak temperature-dependence. This is related to the wavelength shift of the Planck spectrum with varying temperature (compare to Wien's displacement law, equation 2.14).

Finally, by multiplying the total mass-specific extinction coefficient $e^*(T_r)$ with the density ρ, one arrives at the initially introduced extinction coefficient $E_{ex}(T_r)$. It is the reciprocal of the effective mean free path $l_{f,eff}$, which is averaged over all wavelengths [57]:

$$E_{ex}(T_r) = \rho e^*(T_r) = \frac{1}{l_{f,eff}} \tag{4.28}$$

The extinction coefficient $E_{ex}(T_r)$ is needed to calculate the radiative heat conductivity λ_r (see equation 4.20). $E_{ex}(T_r)$ is no longer a material constant, but a characteristic property of a given material sample with density ρ. In this context, it has to be noted that the bulk density of powders can vary considerably between different samples. Furthermore, the material can be compressed by external forces, by its own weight or by vibrations which cause the grains to align in a more compact packing of spheres.

By means of the previous result, one can deduce a criterion that indicates whether the heat diffusion model is suitable for a given case or not. From the requirement that the mean free path $l_{f,eff}$ has to be much smaller than the thickness d of the material sample, one obtains with equation 4.28:

$$l_{f,eff} \ll d \;\Rightarrow\; \frac{1}{\rho e^*(T_r)} \ll d \;\Rightarrow\; d\rho e^*(T_r) \gg 1 \tag{4.29}$$

A given sample between two surfaces at temperatures T_1 and T_2 is called optically thick if $d\rho e^*(T_r) \gg 1$. In this case, the heat diffusion model can be applied, and the total heat exchange no longer depends on surface emissivities [10]. To reduce the heat flux, one has to maximize the optical thickness $\tau_0 = d\rho e^*(T_r)$. The extinction $e^*(T_r)$ depends mainly on optical properties of the material, especially on the effective cross section for scattering and absorption. For example, a practical method to increase $e^*(T_r)$ is the introduction of highly absorbing soot particles.

As a final note, it is remarkable from a physical point of view that all three mechanisms of gas heat conduction, solid heat conduction and radiative heat transfer can be described in an analog way by assuming a gas of particles (accordingly molecules, phonons or photons) and using the kinetic theory of gases. This procedure is very fundamental for the physical description of heat transport. For example, it is also possible to derive an expression for the heat conductivity of metals if one considers a free electron gas and adjusts equation 4.2 respectively [60].

4.4 Coupling Effect

As pointed out in section 4.2, powders have small effective solid thermal conductivities, which is mainly due to thermal resistances as a consequence of pointlike contacts between the grains. However, when the intermediate space between the grains is filled by a gas, the thermal resistances are shorted by gaseous conduction [41, 42, 57, 61]. Therefore, an additional mode of heat transfer occurs, which is referred to as coupling effect and quantitatively expressed by the coupling heat conductivity λ_c. Conduction via the gas inside the pores remains unaffected. The coupling effect can be significant at moderate vacuum pressures ($p > 10\,\text{mbar}$) and at ambient pressure. Values of $\lambda_c = 0.02\,\text{W/mK}$ up to $\lambda_c = 0.03\,\text{W/mK}$ are possible for powders [41, 57], which is in the range of the continuum heat conductivity of air. In order to suppress the coupling, the material has to be sufficiently far evacuated, typically below 1 mbar.

In this thesis, a special model has been developed with the aim to quantify the coupling effect for perlite. It starts out from an existing model for particle beds in general [64], which has been adapted also for aerogels [42]. Although some simplifications are introduced, the measured data for perlite can successfully be described (see sections 6.2.2 and 6.3.2).

For an illustration of the model, the heat transport between two perlite grains is shown in figure 4.5, both with and without coupling. The particles are supposed to be spherical, which is an appropriate assumption for perlite [65]. If the material is completely evacuated (image a), the situation is exactly like in section 4.2, where the heat flow is restricted by the pointlike contact between the grains. A possible pathway is indicated by the red arrow. In the presence of a gas (image b), there are additional routes which involve heat transport along the solid backbone (red arrows) and via the gas (blue arrows). At the grain border, a transition between solid and gaseous conduction occurs. As a consequence, the coupling thermal conductivity can be calculated from a serial connection of thermal resistances, which are defined in analogy to electrical resistances and follow the same rules for serial and parallel connection:

$$
\begin{aligned}
R_{el} = \frac{d}{A\sigma_{el}} \quad &\Rightarrow \quad R_{th} = \frac{d}{A\lambda} \\
R_{tot} \quad &= \quad \sum_{i=1}^{N} R_i \qquad \text{for serial connection} \\
\frac{1}{R_{tot}} \quad &= \quad \sum_{i=1}^{N} \frac{1}{R_i} \qquad \text{for parallel connection}
\end{aligned}
\tag{4.30}
$$

In the above definition, σ_{el} is the electrical conductivity, d is the length of the conductor and A is the reference area.

Applying these relations to the serial connection of solid and gaseous conduction described above, one arrives at:

$$\lambda_c = (1-\Pi)\left[\frac{1-\Gamma}{\lambda_s^*} + \Gamma\left(\frac{\lambda_0}{1+\frac{p_{1/2}^c}{p}}\right)^{-1}\right]^{-1} \tag{4.31}$$

It is assumed that the thermal conductivity for the heat transport along the massive solid backbone is equal to λ_s^* (see section 4.2). For the gas heat conduction, the expression from equation 4.4 is inserted. λ_0 is the continuum thermal conductivity of the gas, and $p_{1/2}^c$ is the characteristic pressure. Because the effective gap size between the grains is different from the average pore diameter, the characteristic pressures $p_{1/2}^c$ for coupling and $p_{1/2}^g$ for gaseous conduction inside the pores are expected to vary from each other. The solid and gaseous contributions to the coupling effect are weighted by the factor Γ, which is related to the relevant pathlengths of the solid and gaseous phase and will be explained below. The overall term is weighted by $1-\Pi$, where Π is a modified porosity which only takes into account the volume of the pores [42]. It differs from the conventional porosity Ψ which also includes the volume of the empty space between the grains. As a consequence, the weighting factor $1-\Pi$ is equal to the volume fraction in which coupling occurs.

Due to the fact that the heat conductivity λ_s^* along the solid is in the order of 1 W/mK (see section 4.2) and thus much larger than the maximum heat conductivity of the gas ($\lambda_0 = 0.026$ W/mK for air at $T = 25$ °C), the first addend in equation 4.31 is expected to become negligible in practice. As an approximation, the coupling thermal conductivity can consequently also be written as:

$$\lambda_c = \frac{1-\Pi}{\Gamma}\frac{\lambda_0}{1+\frac{p_{1/2}^c}{p}} = \Phi\frac{\lambda_0}{1+\frac{p_{1/2}^c}{p}} \tag{4.32}$$

Here, the factors $1-\Pi$ and $1/\Gamma$ have been summarized to a general weighting factor Φ.

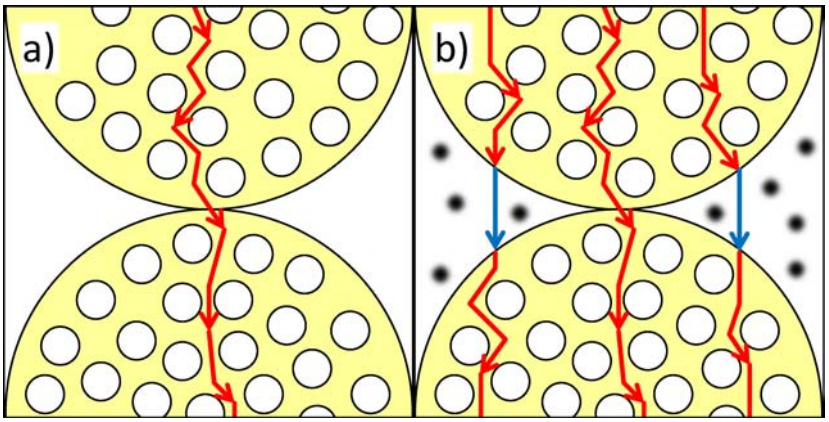

Figure 4.5: Coupling effect for a powder consisting of spherical particles. Gas heat conduction inside the pores is not depicted.

In the following, the weighting factor Γ is described in more detail: Consider the heat flux due to the coupling effect $\dot{Q}_c$, which flows from the warm end of a perlite sample (thickness D_{tot}) to the cold end (temperatures T_1 and T_2). The pathway is composed of small distances d_i, which are located either in the solid phase ($d_{s,i}$, depicted red) or in the gas phase ($d_{g,i}$, depicted blue). On the one hand, the total effective thermal resistance of the sample due to coupling is given by:

$$R_{th} = \frac{D_{tot}}{A\lambda_c} \tag{4.33}$$

On the other hand, from the law of serial connections of resistances (equation 4.30), a second equation for R_{th} is obtained:

$$R_{th} = \sum_{i=1}^{N} R_i = \sum_{i=1}^{N} \frac{d_i}{A\lambda_i} = \frac{D_s}{A\lambda_s^*} + \frac{D_g}{A\lambda_g} \tag{4.34}$$

Here, $D_s = \sum d_{s,i}$ and $D_g = \sum d_{g,i}$ are the total distances which the heat flux travels in either the solid or the gas phase on its way through the perlite sample. λ_s^* and λ_g are the respective thermal conductivities. By comparing equations 4.33 and 4.34, one arrives at:

$$\lambda_c = \left(\frac{D_s}{D_{tot}\lambda_s^*} + \frac{D_g}{D_{tot}\lambda_g} \right)^{-1} \tag{4.35}$$

Because $D_s + D_g = D_{tot}$, the weighting factor Γ is defined according to:

$$\frac{D_g}{D_{tot}} = \Gamma \quad \Leftrightarrow \quad \frac{D_s}{D_{tot}} = 1 - \Gamma \tag{4.36}$$

As a consequence, Γ is always smaller than 1. In the simplified coupling model (equation 4.32), the prefactor $(1 - \Pi)$ is also in the range $0 < (1 - \Pi) < 1$. Hence, the weighting factor $\Phi = (1 - \Pi)/\Gamma$, which is determined by fitting of experimental data in this thesis, can theoretically have values between zero and infinity.

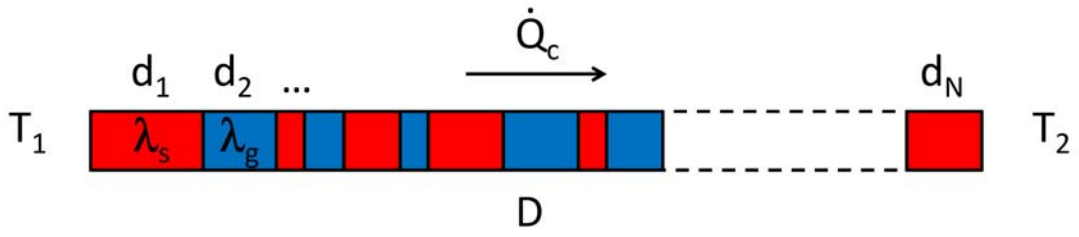

Figure 4.6: Thermal resistance model for the coupling effect.

4.5 Effective Thermal Conductivity

As described in the previous sections, there are four mechanisms of heat transport which contribute to the overall thermal conductivity of an evacuated powder insulation. Assuming that the individual modes proceed independent of each other, the respective heat conductivities can simply be added. This approach corresponds to a parallel connection of thermal resistances and is commonly used in present literature [21, 41, 42, 57, 61, 62]. The interdependency between gaseous and solid conduction is contained in λ_c. The summation yields the so-called effective thermal conductivity λ_{eff}:

$$\lambda_{eff} = \lambda_g + \lambda_s + \lambda_r + \lambda_c \tag{4.37}$$

An overview about the single contributions including their dependencies on pressure, temperature and bulk density is shown in table 4.2. As an important restriction, equation 4.37 is only valid under the requirement that the material is completely dry. The influence of moisture is presented in the following section.

Mode of heat transport	Parameters	Dependencies
gaseous conduction inside pores	p, T	$\lambda_g = \lambda_0 \left(1 + \frac{p_{1/2}^g}{p}\right)^{-1}$ $\lambda_g \sim \sqrt{T}$
solid conduction	ρ, T	$\lambda_s \sim \rho^\gamma$ $\lambda_s \sim T^{-1}$
radiation	ρ, T	$\lambda_r \sim \frac{T_r^3}{e^*(T_r)}$ $\lambda_r \sim \rho^{-1}$
coupling effect	p, T	$\lambda_c = \Phi\lambda_0 \left(1 + \frac{p_{1/2}^c}{p}\right)^{-1}$ $\lambda_c \sim \sqrt{T}$

Table 4.2: Heat transport mechanisms in evacuated powder insulations and their most important dependencies on p, ρ and T for practical purposes.

4.6 Influences of Moisture

The considerations of the previous sections were based on the condition of dry insulation materials. When moisture is present, additional effects can occur. First of all, it has to be mentioned that moisture can exist in a gaseous phase in the form of water vapor and in a liquid phase as water. It is obvious that water vapor increases both gaseous conduction and the coupling effect. The thermal conductivity in the continuum regime given by is $\lambda_{wv} = 0.025\,\mathrm{W/mK}$ at $T = 100\,°\mathrm{C}$ [34] and has almost the same value as air. Moreover, the characteristic pressure for gas heat conduction according to equation 4.4 can be specified for water vapor: $p^g_{1/2} = 120\,\mathrm{mbar}/(d_c\,[\mu\mathrm{m}])$ [57]. In the simultaneous presence of air or other gases, equation 4.13 for gas mixtures can be used. As another obvious effect of moisture, conduction inside a porous structure can be enhanced by liquid water. Due to its high thermal conductivity ($\lambda_w = 0.6\,\mathrm{W/mK}$ at $T = 25\,°\mathrm{C}$ [34, 72]), this can have a significant negative impact. However, this effect requires high moisture levels and therefore only has a minor relevance in practice.

An additional mode of heat transfer occurring in moistened pores is the so-called pore diffusion. This term refers to the transport of latent heat as a result of evaporation and subsequent condensation of water molecules. It requires the pore surface to be completely covered with a thin layer of water [73]. Consider a moistened pore with a temperature gradient (figure 4.7). In equilibrium, evaporation and condensation happen at equal rates over the whole surface. However, the water molecules will preferably evaporate in the hot domain and, after a diffusion process, condensate in the cold region. Because the molecules can move back to the hot region via the water layer on the pore surface, the latent heat Δh_v connected to the phase change is transported from one end of the pore to the other. To quantify this effect, the pore diffusion thermal conductivity λ_{diff} is introduced.

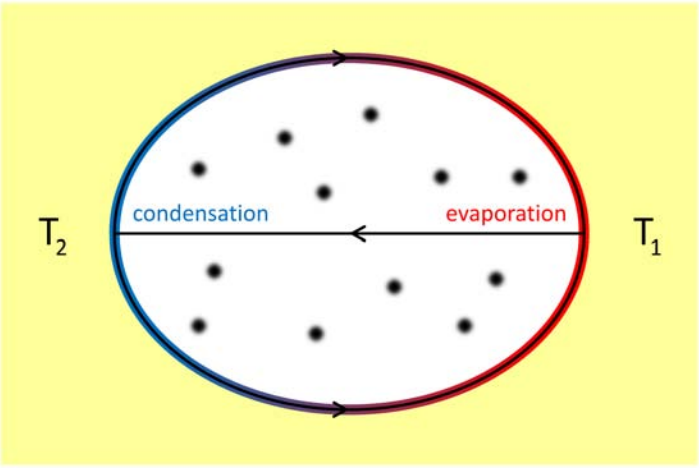

Figure 4.7: Pore diffusion: Transport of latent heat inside a pore due to moisture under the effect of a temperature gradient.

In general, λ_{diff} depends on the vapor diffusion coefficient D_v, the specific heat of evaporation Δh_v and the saturation vapor pressure p_{sat}. The exact dependency on these quantities is not completely consistent, and there are several formulas in literature to express λ_{diff}, which differ slightly from each other [74]. For a bulk material, λ_{diff} is also correlated to the ratio of open and closed pores, because only open pores are well-accessible for moisture. It is also comprehensible that λ_{diff} increases with temperature, since as it is easier to supply the energy needed for the evaporation at higher temperatures. If T approaches the evaporation temperature of water at atmospheric pressure ($T_{ev} = 100\,°\text{C}$), the pore diffusion heat conductivity of a moistened material can be up to 10 times larger than the overall effective heat conductivity of the dry material [74, 75]. This is connected to the fact that the transport of latent heat is a very effective mode of heat transfer. Under vacuum, lower temperatures are sufficient to cause the pore diffusion effect, because the evaporation temperature decreases with lower pressures.

A general model that can be used to describe the heat transport within moistened insulation materials was first developed by Krischer [73]. It has been extended to include materials with both open and closed pores [74]. The model is based on the following steps and assumptions:

- Heat transport within the moistened material can occur via the solid backbone, condensed liquid water, water vapor, other gases (e.g. air) and pore diffusion. The five different modes have to be weighted differently according to their occurrence within the material.

- Solid conduction is described by λ_s. It has to be weighted by a factor of $1 - \Psi$, where $\Psi = 1 - \rho/\rho_s$ is the porosity of the material. For this definition, the bulk density ρ and the solid density ρ_s were used. Pores can be either open or closed, thus $\Psi = \Psi_{op} + \Psi_{cl}$.

- The heat conductivity for closed pores is denoted with λ_{cl}. As closed pores are inaccessible for liquid water by definition, λ_{cl} only includes conduction via gases (e.g. air, water vapor) and radiation: $\lambda_{cl} = \lambda_g + \lambda_r$. The weighting factor is Ψ_{cl}.

- A fraction of open pores described by the factor Ψ_w is completely flooded with liquid water. The thermal conductivity inside these pores is given by $\lambda_w = 0.6\,\frac{W}{mK}$.

- From the remaining part $\Psi_{op} - \Psi_w$, the percentage $1 - b$ is dry, which means that there is no pore diffusion. It can be treated in analogy to closed pores with the only difference being the fact that the gas mixture inside these pores also contains water vapor. Therefore, the thermal conductivity is equal to $\lambda_{op} = \lambda_{g+wv} + \lambda_r$.

- The last fraction of open pores is moistened, and therefore pore diffusion occurs. The heat conductivity in these pores is given by $\lambda_{op} + \lambda_{diff}$. The weighting factor is $b\,(\Psi_{op} - \Psi_w)$.

- To obtain an overall thermal conductivity, the thermal resistances connected to these five modes can be aligned either serial or parallel, depending on the geometry and structure of the material. For a parallel connection, the five thermal conductivities add up, which corresponds to the maximum total heat conductivity (compare equation 4.30). By using the weighting factors, one obtains:

$$\begin{aligned}\lambda_{parallel} &= (1-\Psi)\,\lambda_s + \Psi_w\lambda_w + b\,(\Psi_{op}-\Psi_w)\,(\lambda_{op}+\lambda_{diff}) + \\ &\quad + (1-b)\,(\Psi_{op}-\Psi_w)\,\lambda_{op} + \Psi_{cl}\lambda_{cl}\end{aligned} \tag{4.38}$$

  For a serial connection, which is equivalent to the lowest possible total heat conductivity, the reciprocal values of the heat conductivities add up (equation 4.30), and one arrives at:

$$\lambda_{serial} = \left(\frac{1-\Psi}{\lambda_s} + \frac{\Psi_w}{\lambda_w} + \frac{b\,(\Psi_{op}-\Psi_w)}{\lambda_{op}+\lambda_{diff}} + \frac{(1-b)\,(\Psi_{op}-\Psi_w)}{\lambda_{op}} + \frac{\Psi_{cl}}{\lambda_{cl}}\right)^{-1} \tag{4.39}$$

- In the general case, one combines a serial and a parallel connection and introduces another weighting factor a, so that the overall effective heat conductivity is given by:

$$\lambda_{eff} = \left(\frac{a}{\lambda_{parallel}} + \frac{1-a}{\lambda_{serial}}\right)^{-1} \tag{4.40}$$

  It is obvious that $\lambda_{eff}\,(a=0) = \lambda_{serial}$ and $\lambda_{eff}\,(a=1) = \lambda_{parallel}$. The weighting factor a can be determined experimentally.

An illustrative sketch of the combination of serial and parallel connection including the different weighting factors is shown in figure 4.8.

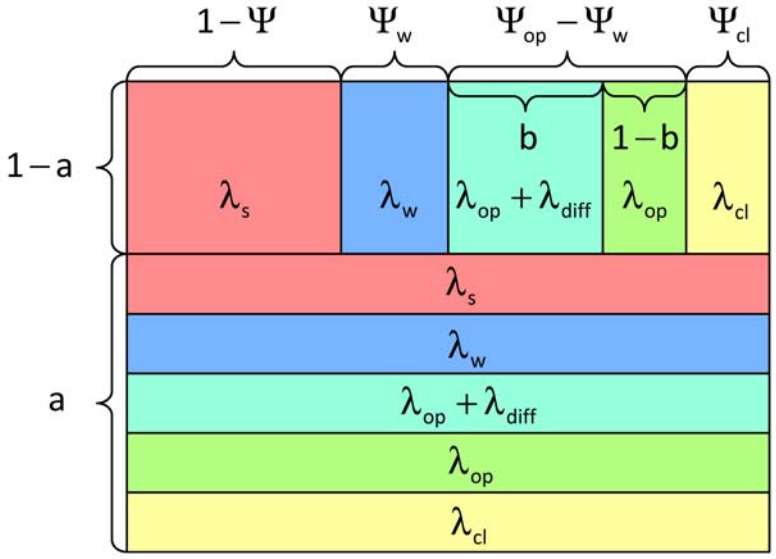

Figure 4.8: Extended Krischer model for the calculation of the effective heat conductivity of moistened materials [73, 74].

For various insulation materials like mineral wool, foam glass, polystyrene, polyurethane and also perlite, the extended Krischer model has successfully been used to describe the temperature dependency of the effective thermal conductivity under the effect of moisture [74, 75]. However, as a restriction, the measurements have only been performed at ambient pressure.

From a look at the phase diagram of water (figure 4.9), one can deduce some important facts for the practical relevance of the possible moisture-related effects described above: The triple point of water is at $p = 6.1\,\text{mbar}$ and $T = 0.01\,°\text{C}$ [72]. At lower pressures, water can only exist in the solid or in the gaseous phase. In vacuum super insulations, the pressure is typically at $0.001\,\text{mbar} \leq p \leq 1\,\text{mbar}$. As a consequence, pore diffusion cannot occur, because it requires a liquid phase. Above $T = 0\,°\text{C}$, the only disadvantageous effect that can play a role in practice is the additional gas conduction due to water vapor. In order to reduce the moisture content and to minimize this effect, the insulating material can be baked out. The decrease of the water content with time during a baking-out process is examined experimentally in section 6.4.

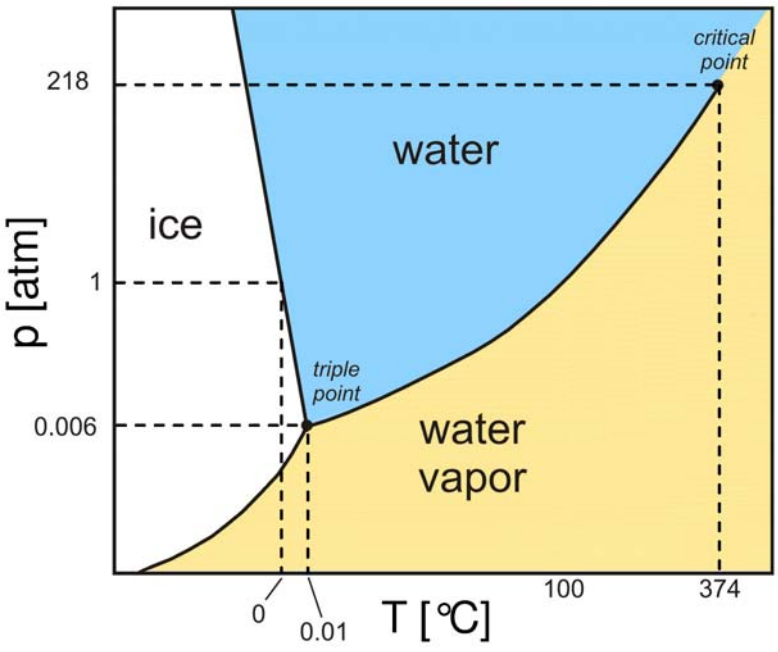

Figure 4.9: Phase diagram of water [76].

Chapter 5

Perlite and Vacuum Super Insulation: State of the Art

As already mentioned in section 3.3.2, a vacuum super insulation can be realized with any kind of porous insulation material. For large storage tanks and applications under vacuum, powders and granules have a practical advantage, as they can be installed by pouring or air-injection. In contrast, the mounting of plates made of e.g. polyurethane or foam glass is rather complicated. Especially perlite is a commonly used material for vacuum super insulations. Other granular materials like diatomaceous earth (kieselguhr), expanded clay or expanded glass granules are also possible, but their practical relevance is not as high. In this chapter, the special properties of perlite which have led to this fact are described, and the most important applications of vacuum super insulation are presented. Furthermore, the results of former research on perlite are outlined, and the motivation for the additional experiments performed in this work is motivated.

5.1 General Properties of Perlite

Perlite [77, 78, 79] is a naturally occurring mineral of volcanic origin. The source material is obsidian (volcanic glass), which is transformed into perlite by hydration. Therefore, perlite has an amorphous structure and a relatively high water content of up to 2 %. The raw material is mainly composed of SiO_2 (65 - 75 %) and Al_2O_3 (10 - 15 %) with small amounts of K_2O, Na_2O, Fe_2O_3, CaO and MgO. It has a mass density of around $\rho = 900...1000$ kg/m³. Due to on-going volcanic activity, the worldwide perlite resources are constantly regenerated.

In a technical expansion process, raw perlite (figure 5.1 a) is heated to temperatures of 850 °C up to 1000 °C, which is close to the glass transition temperature of the amorphous material. As a consequence, the material softens, and enclosed water vaporizes creating a large number of microscopically small pores. After the water has escaped, the porous structure is cooled under well-defined conditions and regains its mechanical stability. As a result of the whole process, the volume can be increased by a factor of 7 up to 20 compared to the raw material, and the bulk density can be tuned between $\rho = 30\,\mathrm{kg/m^3}$ and $\rho = 240\,\mathrm{kg/m^3}$. The low density and the correspondingly high porosity ($0.75 \leq \Psi \leq 0.97$) are two very characteristic properties of expanded perlite (figure 5.1 b), which also make the material suitable for vacuum super insulation. As explained in section 4.1 (compare equation 4.4), the effective pore size has a large influence on the pressure dependence of the gaseous heat conductivity.

In practice, other beneficial properties of expanded perlite are the low price (around 50 €/m³), the high temperature stability (up to 800 °C) and the fact that it is nonburnable and therefore meets fire protection regulations. Furthermore, the material is only weakly hygroscopic, as the fraction of open pores is relatively low [79]. This is an important factor, because moisture can dramatically increase the thermal conductivity (see section 4.6). Apart from the applications for vacuum super insulation, which will be treated in the following sections, there are numerous other fields of application. For instance, the material is used in building technology for thermal insulation at ambient pressure, for acoustic insulation and for lightweight plasters and mortars. In horticulture, soil can be mixed with expanded perlite to reduce compaction and to improve the permeability to air. As a last example, the beverage industry uses expanded perlite for filtering purposes in many production processes [77, 78].

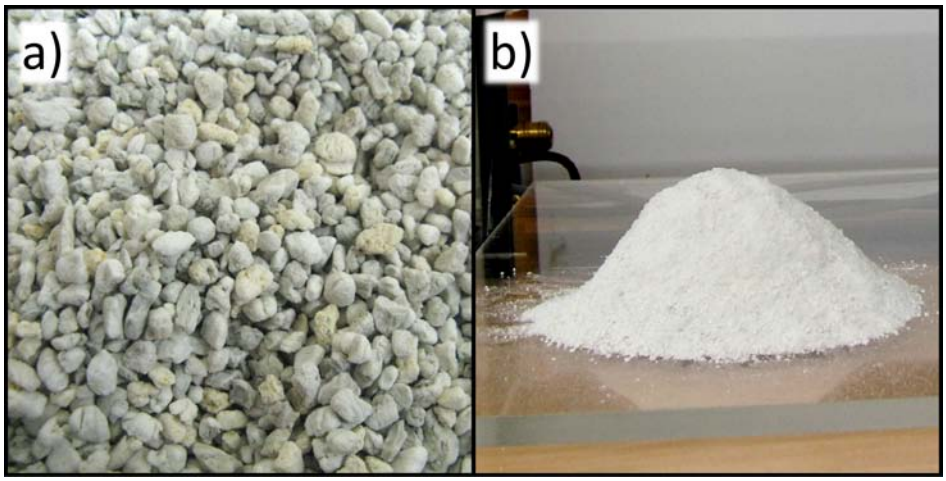

Figure 5.1: Raw (a) and technically expanded (b) perlite [80].

5.2 Vacuum Super Insulation in Cryogenic Engineering

Vacuum super insulation with perlite has established itself as a practical and cost-effective method for the storage of liquid gases. A storage tank (figure 5.2) consists of an inner vessel with a volume of typically a few m³. By a suspension device, it is fixed in the outer container. The annular gap between both vessels is filled with perlite and evacuated into the range of fine vacuum ($p \approx 0.01$ mbar). At this pressure, the effective thermal conductivity of the insulation is sufficiently low, because gas heat conduction is suppressed and only solid conduction and radiative heat transport remain. Nevertheless, a small heat flux occurs, which causes a fraction of the liquid gas to heat up and evaporate. This has a cooling effect, because the heat of evaporation is withdrawn from the liquid. As a consequence of these two antagonizing effects, the temperature of the liquid stays constant. However, the tank pressure increases. As the inner vessel can only withstand pressures of a few bar, the excessive pressure has to be exhausted through a safety valve if the gas is not extracted for its intended use over a longer time interval [81].

In general, this application of an evacuated perlite insulation is very similar to the intended long-term storage of hot water. However, liquid gases are typically stored between 20 K (hydrogen) and 90 K (oxygen), whereas the storage temperature for hot water can be up to 373 K (100 °C) and higher if the water is pressurized. This makes a considerable difference, as the thermal conductivity of evacuated perlite is temperature-dependent (see chapter 4), especially the radiation part which scales with T^3 (see equation 4.20).

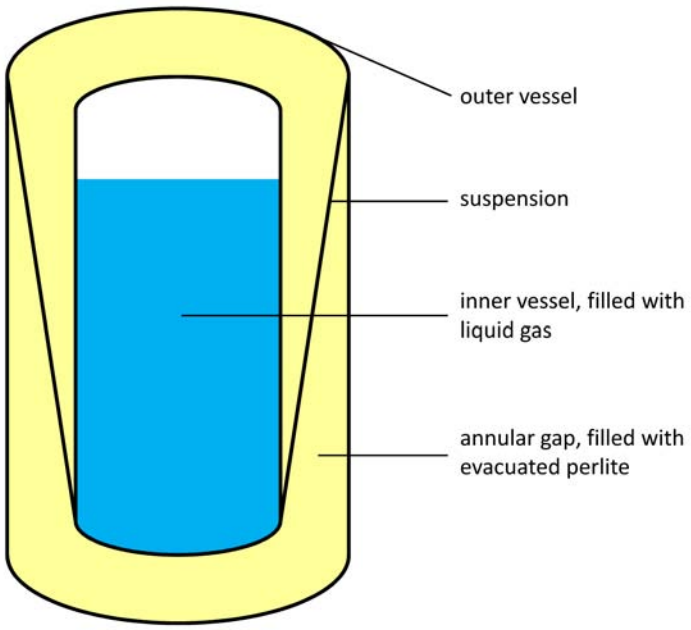

Figure 5.2: Schematical design of a cryogenic storage tank.

5.3 Vacuum Super Insulation of District Heating Pipelines

The concept of long-distance district heating is, to use medium-temperature waste heat ($80\,°C \leq T \leq 130\,°C$) from industrial processes or power plants for residential heating. The heat transfer medium is water. Because the distance between industrial and residential areas is usually a few kilometers, well-insulated pipelines are important for the overall system efficiency. Furthermore, the maximum economically reasonable distance between heat producers and consumers can be increased by a better insulation. For this reason, vacuum super insulation of district heating pipelines has been considered at the beginning of the 1980s, and selected materials including perlite have been examined for this application by Deimling [21, 82]. The measurements of the effective thermal conductivities have been performed in a parallel plate setup and in a real-size pipeline test station with cylindrical geometry. Three perlite samples with the following densities and grain sizes have been investigated:

	density ρ [kg/m³]	grain size d_g [mm]
sample 1	40	0.7...0.8
sample 2	61	0.4
sample 3	88	< 0.1

Table 5.1: Perlite samples examined by Deimling [21, 82].

The most important results of Deimling's measurements are:

- In accordance with the Smoluchowski effect (section 4.1), the effective thermal conductivity decreases at lower pressures following the characteristic S-curve. The characteristic half-value pressure is in the order of $p_{1/2} = 10\,\text{mbar}$, which corresponds to an effective pore diameter of around 20 µm (compare equation 4.4)
- In good approximation, the effective thermal conductivity increases linearly with temperature between $T = 50\,°C$ and $T = 130\,°C$.
- At higher bulk densities, the decrease of the gaseous heat conductivity starts already at higher pressures. This is in good accordance with equation 4.4 and figure 4.2, because the effective distance between the powder grains and therefore the characteristic length d_c is smaller at higher densities.
- The effective heat conductivity in the fully evacuated state ($p < 0.01\,\text{mbar}$) is around $\lambda_{eff} \approx 0.01\,\text{W/mK}$ for samples 1 and 2. The third sample with the highest density showed the lowest value with $\lambda_{eff} \approx 0.005\,\text{W/mK}$. All measurements refer

to a mean sample temperature of $T = 75\,°C$. As a possible explanation, one could state that there is a considerable amount of radiative heat exchange, which gets reduced at higher density (compare section 4.3). Obviously, the contribution of solid conduction, which increases with density, has only a minor impact. This was also a result of the computational evaluation method used by Deimling, where the obtained values of λ_s were close to zero. Solid conduction was therefore ignored in his model.

- In general, sample 3 yields the best results regarding the decrease of λ_{eff} with pressure ($p_{1/2} \approx 20\,\text{mbar}$) and regarding the value of λ_{eff} in the fully evacuated state. The sample was prepared by sifting out a very fine fraction with a grain diameter of $d < 0.1\,\text{mm}$ from the original perlite material. The resulting high density and the small distance between the powder grains has a beneficial effect on the suppression of radiation and gas heat conduction.

5.4 Vacuum-Super-Insulated Panels in Civil Engineering

As the most recent important application of the vacuum super insulation technology, the so-called vacuum insulation panels (VIP) can be mentioned [83, 84, 85]. This term refers to insulating plates which have originally been developed for refrigerators. By intense research and development at ZAE BAYERN during the last decade [57, 61], VIPs have been adapted for the thermal insulation of buildings and are now available on the market as commercial products. Essentially, a VIP consists of a compressed, evacuated kernel material, which has to withstand the mechanical load caused by the atmospheric pressure (10 t/m²), and a vacuum-tight laminate (figure 5.3). In the evacuated state, the panels have an effective thermal conductivity of around $\lambda = 0.007\,\text{W/mK}$.

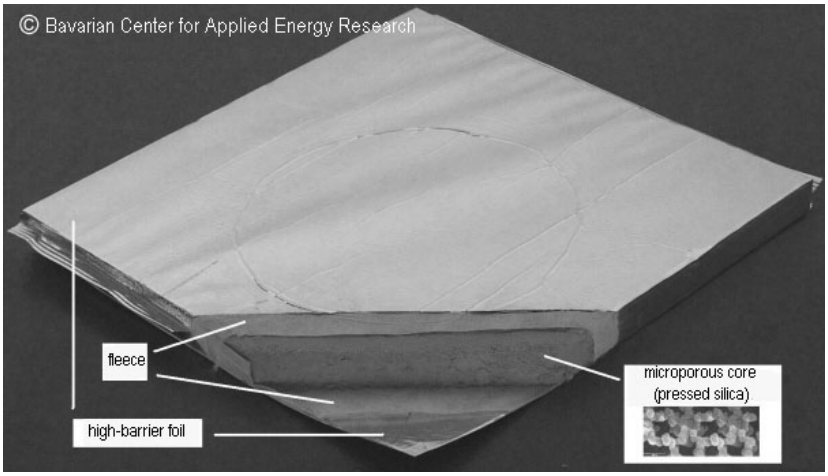

Figure 5.3: Sliced vacuum insulation panel [86].

The sealing foil consists of several resilient polymer layers. Since polymers are rather permeable for water vapor, nitrogen and oxygen, the foils are coated with a thin aluminum layer ($d = 100\,\text{nm}$). The kernel material is usually not perlite, and fumed silica is used instead. This material has a notably finer pore structure with average pore diameters of only 200 nm. Therefore, gas heat conduction is already suppressed at relatively high vacuum pressures of 20 to 50 mbar. This is important for the long-term stability of VIPs. At the beginning of their life cycle, the panels are evacuated to $p = 0.1\,\text{mbar}$. With a pressure increase of 1 to 2 mbar per year due to leakages, they maintain their insulating properties over a few decades, and the effective thermal conductivity is expected to remain below $\lambda = 0.008\,\text{W/mK}$ even after a duration of 50 years [57]. As another beneficial consequence of the small pore diameter, the thermal conductivity of fumed silica at ambient pressure is only $\lambda = 0.018\,\text{W/mK}$ [83]. Hence, even when the sealing laminate is damaged and the vacuum inside the panel is destroyed, an effective thermal insulation is still existent. To suppress radiative heat transport inside the kernel material, infrared opacifiers like SiC can be introduced.

Compared to conventional insulation materials, the advantage of VIPs is that they reach the same heat transfer coefficient (k-value) at a much smaller insulation thickness. To obtain the same k-value as a VIP with a thickness of 5 cm, one would have to use 30 cm of conventional insulation. Due to this, VIPs are especially used for insulation applications under spatial constraints (e.g. due to urban heritage conservation), where they are also economically reasonable. The average price of VIPs with a thickness of 2 cm is between 50 and 100 €/m².

Apart from building applications, VIPs are also used for cooling of food or pharmaceuticals, especially in refrigerated vehicles. Also here, the increase of usable volume pays off the higher costs of VIPs. To withstand the mechanical stress which occurs for instance at the bottom of a cooling chamber, the aluminum-polymer laminate can be replaced by thin sheets of high-grade steel.

5.5 Material Selection and Motivation for Additional Research

For the vacuum super insulation of the first hot water storage tank prototype (see chapter 7), the perlite TECHNOPERL ® - C 1,5 from the Austrian manufacturer EUROPERL, STAUSS PERLITE GMBH is used [79, 87]. This material has already been applied successfully to liquid gas storage tanks (compare section 5.2). According to the specification of the manufacturer, the density of an uncompressed bulk is $\rho \approx 53\,\text{kg/m}^3$, and the grain size varies between 0 and 1.5 mm. However, it shows in practice that the material can be compressed up to $\rho \approx 100\,\text{kg/m}^3$ by vibration or by applying mechanical pressure. Although measurement data for perlite is already known from the work of Deimling (section 5.3), there is still motivation for further investigation of perlite in general and

TECHNOPERL ® - C 1,5 in particular:

- The perlite used by Deimling differs from TECHNOPERL ® - C 1,5 regarding grain size and density, especially sample 3 (see table 5.1), which showed the best results.
- In general, perlite may not always have exactly identical properties, since it is a natural product.
- TECHNOPERL ® - C 1,5 is optimized for cryogenic application and performs well within this temperature range. However, in the temperature regime of hot water storage, radiation may have a significantly higher impact. Therefore, it is not clear whether the existing technology for liquid gas storage can easily be transferred towards higher temperatures, and whether TECHNOPERL ® - C 1,5 is also the optimum material for vacuum super insulation of hot water storages.
- The coupling effect in perlite has not been investigated separately by Deimling and is still unclear. Also for other vacuum super insulation materials like aerogels, a fully satisfying agreement between the developed theoretical models and the measured data has not yet been achieved [42].
- In practice, the utilization of inert gases may help to keep the thermal conductivity constant for a longer time interval in spite of technically unavoidable leakages of the storage tank (see section 4.1). However, the thermal conductivity of perlite under the influence of these gases has not yet been investigated experimentally.
- Although TECHNOPERL ® - C 1,5 is described to be non-hygroscopic by the manufacturer [79], it is not known how much moisture (in percent of weight) is actually contained.

Because additional research on the material was necessary due to the above reasons, several experiments were performed at ZAE BAYERN (chapter 6). The fundamental tasks were to quantify the contributions of the different heat transport mechanisms described in chapter 4 and to investigate the open questions mentioned above. Besides the laboratory experiments, heat loss measurements on a real-size storage tank prototype were done in order to study whether the results are also valid under practical conditions (chapter 7).

Chapter 6

Laboratory Measurements Regarding the Heat Conductivity of Evacuated Perlite

The following chapter describes the laboratory experiments which were performed at the ZAE BAYERN departments in Würzburg and Garching in order to determine the thermal conductivity of TECHNOPERL ® - C 1,5 under various conditions. As a preliminary examination, spectroscopical measurements were done to obtain the radiative heat conductivity (section 6.1). Subsequently, the effective thermal conductivity as a function of air pressure, bulk density and temperature was measured in a parallel plate setup (section 6.2) for a general understanding of solid and gaseous conduction and the coupling effect. Apart from that, effective thermal conductivity measurements were also performed in a cut-off cylinder apparatus (section 6.3) to examine the effects that occur, when argon and krypton are used as filling gases instead of air. This device also served for a cross-check of the results from the parallel plate apparatus. Finally, the moisture content of TECHNOPERL ® - C 1,5 was determined (section 6.4).

6.1 Spectroscopic Determination of The Radiative Thermal Conductivity

If an insulation material is sufficiently far evacuated ($p \leq 10^{-3}$ mbar for perlite), gas conduction and coupling are suppressed ($\lambda_g = \lambda_c = 0$, see sections 4.1 and 4.4). In this state, the total effective thermal conductivity is the sum of radiative and solid heat conductivity:

$$\lambda_{eff}\,(p \to 0) = \lambda_r + \lambda_s \tag{6.1}$$

Because both contributions depend on density and temperature (see sections 4.2 and 4.3), they are difficult to separate by pure thermal conductivity measurements. However,

there is a different approach to determine the radiative thermal conductivity experimentally. As explained in section 4.3, λ_r is related to the extinction of thermal radiation, which is the combination of scattering and absorption within a material. This property can be determined by infrared spectroscopy measurements. The special technique of Fourier transform infrared spectroscopy (FTIR) [88, 89, 90] was used for this purpose.

6.1.1 Principles of FTIR Spectroscopy

The most essential part of an FTIR spectrometer is a Michelson interferometer (figure 6.1). The beam emitted by the IR-radiation source (ideally a blackbody) is collimated and directed on a semi-transparent mirror, where it is divided into two partial beams. From this point, there are two relevant pathways. The first partial beam is reflected at the semi-transparent mirror, reflected at the fixed mirror and transmitted on the semi-transparent mirror. The second beam first passes the semi-transparent mirror and is then reflected both at the moving mirror and at the semi-transparent mirror. At this point, the two partial beams are merged, interfere with each other and result in the outgoing beam. The outcome of the interference depends on the path difference x, which can be calculated from the distances between the mirrors:

$$x = 2\left(d_m - d_f\right) \tag{6.2}$$

For a given wavelength λ, the maximum positive interference occurs if x is an integer multiple of λ. By contrast, if x is an odd-numbered multiple of $\lambda/2$, both beams annihilate each other. Assuming that the intensity of both partial beams is equal ($I_m = I_f = I$), the intensity I_λ of the outgoing beam due to interference at a single wavelength λ is given by:

$$I_\lambda = I\left(1 + cos\left(\frac{2\pi}{\lambda}x\right)\right) = I\left(1 + \cos\left(2\pi\tilde{\nu}x\right)\right) \tag{6.3}$$

Here, the wave number $\tilde{\nu} = 1/\lambda = \nu/c$ is introduced, which is defined as the reciprocal of the wavelength. The wave number is proportional to the freqency ν, and the factor of proportionality is the inverse of the speed of light c. The total intensity of the outgoing beam as a function of the path difference $I_{tot}(x)$ is then obtained by integrating over all wave numbers in the interval $B = [\tilde{\nu}_1, \tilde{\nu}_2]$, which is the so-called bandwidth of the spectrometer:

$$I_{tot}(x) = \int_{\tilde{\nu}_1}^{\tilde{\nu}_2} \left(I(\tilde{\nu}) + I(\tilde{\nu})\cos\left(2\pi\tilde{\nu}x\right)\right) d\tilde{\nu} \tag{6.4}$$

The first addend yields a constant which does not contain any relevant information and can thus be subtracted. This step is usually performed electronically by the spectrometer device. Below, only the second addend $I(x)$ is considered:

$$I(x) = \int_{\tilde{\nu}_1}^{\tilde{\nu}_2} I(\tilde{\nu}) \cos(2\pi\tilde{\nu}x)\, d\tilde{\nu} = \int_{-\infty}^{\infty} I(\tilde{\nu}) \cos(2\pi\tilde{\nu}x)\, D(\tilde{\nu}) d\tilde{\nu} \tag{6.5}$$

By introducing a window function $D(\tilde{\nu})$ which is equal to one for $\tilde{\nu} \in [\tilde{\nu}_1, \tilde{\nu}_2]$ and zero otherwise, the integration boundaries can be extended to plus and minus infinity.

Equation 6.5 already looks similar to a Fourier transform, but the sine term of the transformation factor $\exp(2\pi i\tilde{\nu}x) = \cos(2\pi\tilde{\nu}x) + i\sin(2\pi\tilde{\nu}x)$ is missing. However, $I(x)$ is an even function since $I(-x) = I(x)$, and thus one can replace $\cos(2\pi\tilde{\nu}x)$ by $\exp(2\pi i\tilde{\nu}x)$. The integral over the sine term must be zero due to the fact that the Fourier representation of an even function may only contain cosine functions which are also even. Therefore, one finally arrives at equation 6.6, which is the definition of the Fourier transform:

$$I(x) = \int_{-\infty}^{\infty} I(\tilde{\nu}) \exp(2\pi i\tilde{\nu}x)\, D(\tilde{\nu}) d\tilde{\nu} \tag{6.6}$$

For spectroscopy measurements, one is typically interested in the spectral intensity $I(\tilde{\nu})$. It can be obtained by measuring $I(x)$ and applying the inverse Fourier transform:

$$I(\tilde{\nu}) = \int_{-\infty}^{\infty} I(x) \exp(-2\pi i\tilde{\nu}x)\, D(\tilde{\nu}) dx \tag{6.7}$$

$I(\tilde{\nu})$ only contains contributions which depend on the path difference x. Constant addends like like thermal irradiation of the investigated sample are filtered out by the Fourier transform.

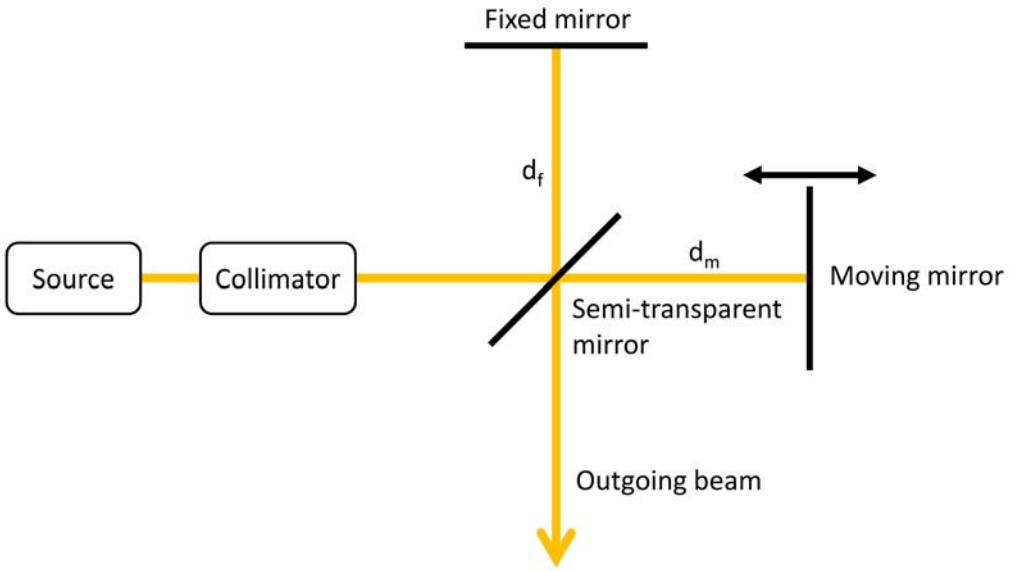

Figure 6.1: Setup of a Michelson interferometer.

6.1.2 Measurement Procedure

To determine the extinction of thermal radiation, usually three measurements are performed:

- A reference measurement (figure 6.2 a), where the outgoing beam of the Michelson interferometer is directly detected. An integrating sphere (Ulbricht sphere) is used to diffuse the beam and to reach a spatially homogeneous intensity.
- A transmission measurement (figure 6.2 b), where the sample is placed in the beamline, and the transmitted radiation is detected with the aid of the integrating sphere.
- A reflection measurement (figure 6.2 c), where the radiation reflected by the sample is detected.

For all three measurements, the position of the moving mirror is varied, and the resulting intensities $I(x)$, which are measured at the detector, are recorded. Subsequently, the respective spectral intensities $I(\tilde{\nu})$ are calculated from the inverse Fourier transform. The extinction of the sample as a function of the wave number is then given by:

$$e(\tilde{\nu}) = \frac{I_{reference}(\tilde{\nu}) - I_{transmission}(\tilde{\nu}) - I_{reflection}(\tilde{\nu})}{I_{reference}(\tilde{\nu})} \tag{6.8}$$

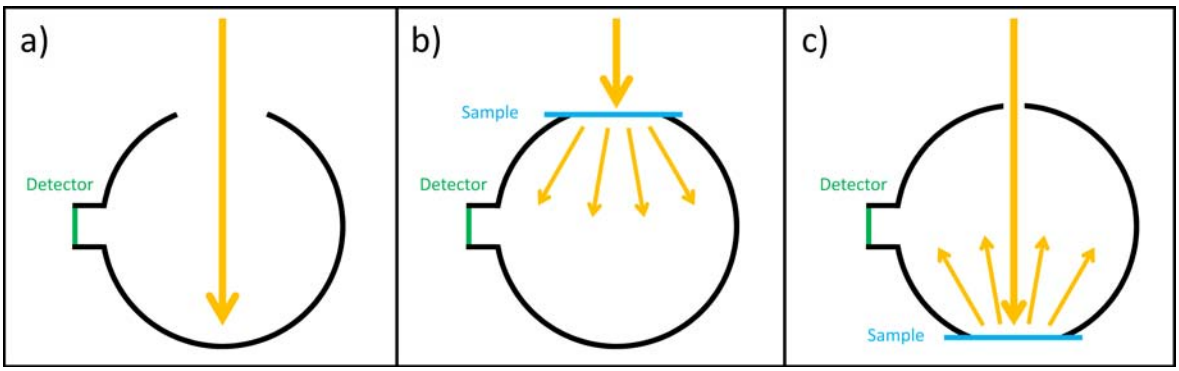

Figure 6.2: FTIR spectroscopy: Positioning of sample, integrating sphere and detector for the reference (a), transmission (b) and reflection (c) measurement.

6.1.3 Experimental Results

For the FTIR spectroscopy measurements of TECHNOPERL ® - C 1,5, thin homogeneous layers of the perlite powder were prepared on an IR-transparent polymer foil. The measured data for the extinction $e(\tilde{\nu})$ was converted back into units of wavelength. For each sample, the areal mass density (mass of the sample divided by the area which is covered by the sample) was determined to calculate the mass-specific extinction coefficient $e^*_\lambda(\lambda)$ (equation 4.23). In figure 6.3, $e^*_\lambda(\lambda)$ is shown as a function of wavelength. The

data of several samples was averaged. The bandwidth of the spectrometer ranged from 1.4 to 18 µm and covers the whole wavelength interval which is relevant for thermal radiation at temperatures between approximately 300 and 500 K (compare figure 2.4 and equation 2.14).

The remaining procedure to obtain the radiative thermal conductivity is described in section 4.3. First, the total mass-specific extinction coefficient $e^*(T)$ has to be calculated using equation 4.25. As already mentioned, $e^*(T_r)$ has a weak temperature-dependence. A plot of $e^*(T_r)$ versus temperature is shown in figure 6.4 for temperatures between 300 and 450 K. In this temperature interval, the total mass-specific extinction coefficient can be approximated with sufficient accuracy using a second order polynomial (equation 6.9). The error of $e^*(T_r)$ is given by $\Delta e^* = 4\,\mathrm{m^2/kg}$ [63].

$$e^*(T_r) = \left(5.32 \cdot 10^{-4} \cdot T_r[\mathrm{K}]^2 - 0.4503 \cdot T_r[\mathrm{K}] + 130.31\right) \frac{m^2}{kg} \pm 4 \frac{m^2}{kg} \tag{6.9}$$

Eventually, for a given bulk density ρ and radiation temperature T_r (see equation 4.21), the radiative heat conductivity of TECHNOPERL ® - C 1,5 can be calculated from equation 6.10, which follows from equations 4.20 and 4.28:

$$\lambda_r = \frac{16\sigma\tilde{n}^2 T_r^3}{3\rho e^*(T_r)} = \frac{16\sigma T_r^3}{3\rho e^*(T_r)} \tag{6.10}$$

For $e^*(T_r)$, the expression from equation 6.9 can be used. The refractive index can be approximated by $\tilde{n} = 1$. At the temperature regime which is relevant for the conventional storage of hot water ($T_1 = 373$ K or lower, $T_2 = 273$ K) and for bulk densities between $\rho = 53\,\mathrm{kg/m^3}$ and $\rho \approx 100\,\mathrm{kg/m^3}$ (see section 5.5), one obtains radiative thermal conductivities between $\lambda_r = 2 \cdot 10^{-3}\,\mathrm{W/mK}$ and $\lambda_r = 5 \cdot 10^{-3}\,\mathrm{W/mK}$ (see table 6.1). Compared to the cryogenic application ($T_1 = 90$ K, $T_2 = 293$ K), the radiative heat conductivity is increased by a factor of 4 to 5. However, the absolute value of λ_r still looks promisingly low, especially at higher densities.

	T_1 [K]	T_2 [K]	T_r [K]	e^* [m²/kg]	ρ [kg/m³]	λ_r [10^{-3} W/mK]
cryogenic application	90	293	208	59.7	53	0.9
					100	0.5
hot water storage low temperature	323	273	299	43.3	53	3.5
					100	1.9
hot water storage high temperature	373	273	326	40.1	53	4.9
					100	2.6

Table 6.1: Radiative thermal conductivity of TECHNOPERL ® - C 1,5 at different application temperatures and bulk densities.

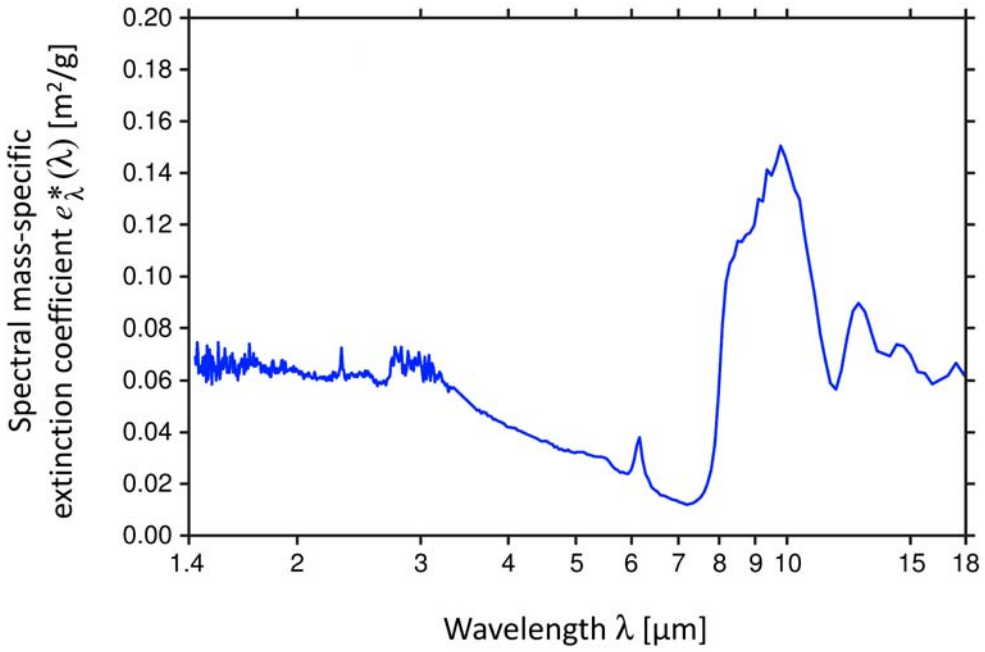

Figure 6.3: Spectral mass-specific extinction coefficient of TECHNOPERL ® - C 1,5 as a function of wavelength between 1.4 and 18 µm [63].

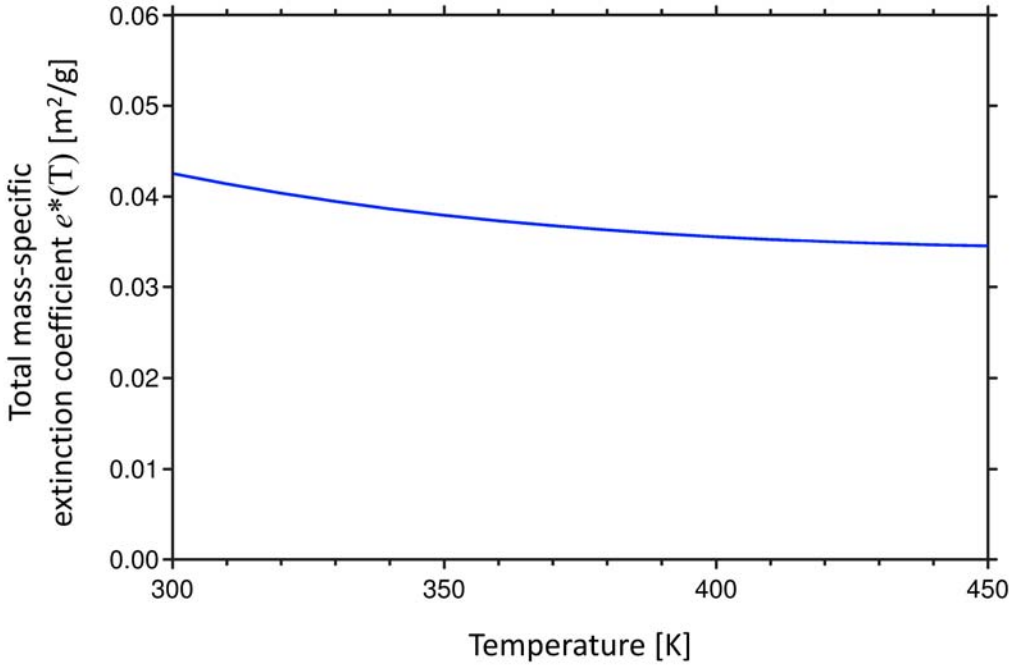

Figure 6.4: Total mass-specific extinction coefficient of TECHNOPERL ® - C 1,5 as a function of temperature between 300 and 450 K. The error of the measurement is $\Delta e^* = 0.004\,\mathrm{m^2/g}$ [63].

6.2 Effective Thermal Conductivity Measurements in a Parallel Plate Setup

After the radiative part of the heat transport had been investigated, the effective thermal conductivity of TECHNOPERL ® - C 1,5 was determined experimentally in a parallel plate apparatus at the ZAE BAYERN division in Würzburg. The device [91, 92] has been especially developed for thermal conductivity measurements of evacuated super insulations and allows the adjustment of vacuum pressure, temperature and bulk density of the investigated samples. The variation of these parameters is necessary to examine the validity of theoretical models and to separate gaseous conduction and the coupling effect from solid conduction and radiative heat transport.

6.2.1 Measurement Setup and Experimental Procedure

The layout of the parallel plate apparatus is shown in figure 6.5. The central components of the device are an electrically heated circular hot plate (2) and two cold plates (3,4) inside a vacuum chamber (1). Two identical samples (5) are placed symmetrically in the gaps between the metal plates. The inner hot plate has a diameter of $d_h = 200\,\text{mm}$ and is surrounded by two guard rings, which are kept at the same temperature T_h to prevent radial heat flux. A heat sink (6), which is needed to control the temperature T_c of the cold plates ($d_c = 280\,\text{mm}$), is realized by circulating a fluid. All temperatures are measured using Pt-100 resistances.

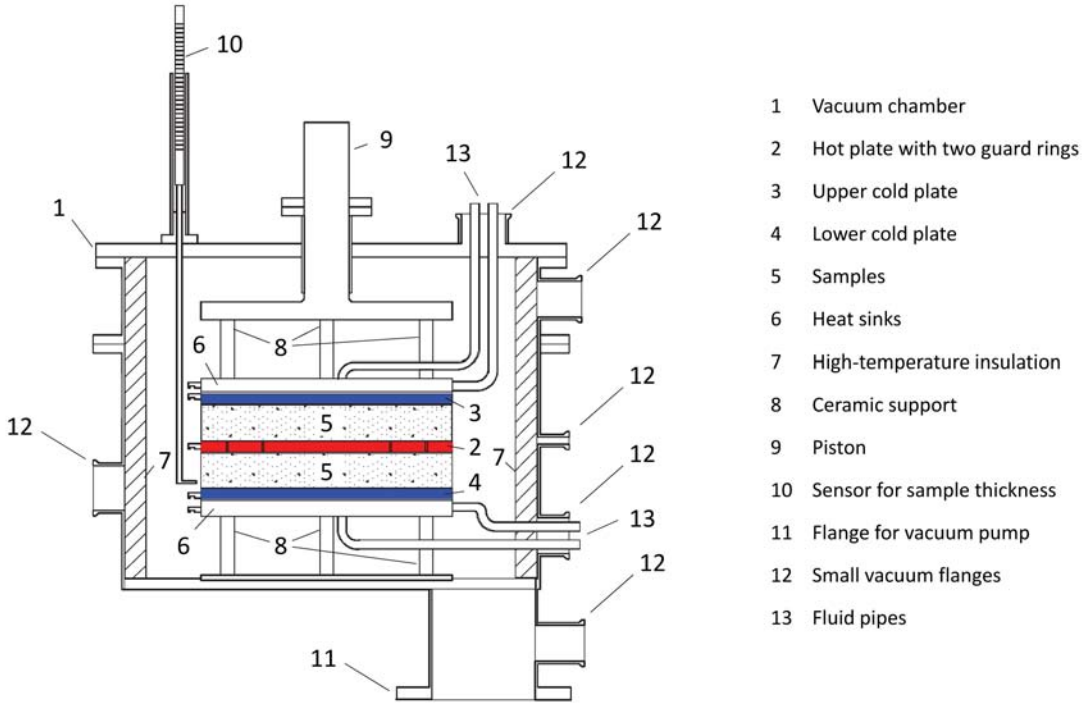

Figure 6.5: Layout of the parallel plate apparatus for thermal conductivity measurements [91, 92].

By applying a mechanical force via a piston (9), the density of the investigated samples can be varied. The sample thickness d_s may range from 1 to 28 mm and can be measured with an appropriate sensor (10). The heating power P_{el}, which is needed to keep the temperature of the hot plate constant, is regulated by a proportional-integral controller. It is calculated according to $P_{el} = R_{el} I_{el}^2$ where R_{el} is the (temperature-dependent) resistance of the electrical heater and I_{el} is the current which is measured as the voltage drop across a 1 Ω precision shunt. In the stationary case, the heating power is equal to the one-dimensional heat flux which flows symmetrically from the hot plate through both samples to the cold plates. The assumption of stationary conditions is assumed to be valid when all temperatures and the heating power have remained constant for at least 1.5 hours. The data of the last hour is then averaged to calculate the thermal conductivity of the sample material according to equation 6.11:

$$\lambda = \frac{P_{el} d_s}{2A\Delta T} = \frac{2P_{el} d_s}{\pi d_h^2 \left(T_h - T_c\right)} \tag{6.11}$$

For the evaluation of the measurements, the following systematic errors have to be taken into account [92]:

Temperature: Due to the tolerances of the Pt-100 sensors, the measured temperature difference ΔT between hot and cold plates is only accurate within 0.5 K.

Electrical power: Because of the high precision shunt resistance, the relative error of the heating current is only 0.1 %. However, the resistance of the heater is much less accurate. In total, an error of 1 % for the electrical heating power is estimated.

Sample thickness: The absolute error of the thickness sensor is given by 0.2 mm.

Measuring area: The area $A = \pi d_h^2$ has a relative error of 0.5 %, which corresponds to an absolute value of $1.57 \cdot 10^{-4}$ m².

Radial heat losses: If the central hot plate and the guard rings are not exactly at the same temperature, a radial heat flux occurs, which leads to a systematic error. From test measurements it is known that the radial heat loss is limited by 0.15 W in the worst case that can occur in practice. For samples with thermal conductivities above 0.1 W/mK, the heat flux through the sample is typically around 10 W, and thus the relative error due to radial heat losses is less than 2 %.

For specimens with thermal conductivities smaller than 0.1 W/mK (which is always valid for super-insulating materials), the heat flux through the sample can become as low as 0.3 W and is thus in the range of the maximum possible radial heat loss. For this case, a special correction method [92] has been developed to avoid high relative errors: Based on the assumption that radial heat losses and errors in measured temperatures are independent of the temperature difference ΔT between both plates, two measurements at different values of ΔT are performed. By taking the difference of both experiments, the errors are eliminated:

$$P_{el,1} = \lambda \frac{2A}{d_s} \Delta T_1 \qquad P_{el,2} = \lambda \frac{2A}{d_s} \Delta T_2$$

$$\begin{aligned} P_{el,1} - P_{el,2} &= \lambda \frac{2A}{d_s} (\Delta T_1 - \Delta T_2) \\ \lambda &= \frac{(P_{el,1} - P_{el,2})\, d_s}{2A\,(\Delta T_1 - \Delta T_2)} \end{aligned} \tag{6.12}$$

In other words, the measurement values are extrapolated to $\Delta T = \infty$, where both the relative error caused by radial heat losses and the relative error of the temperature measurement are zero. As a result of the correction method, the remaining error $\Delta\lambda_{T+rhl}$ (not including errors of measuring area, electrical power and sample thickness) is typically around 2 %. According to the law of propagation of uncertainty (equation 6.13), the total error of the measurement was calculated according to equation 6.14:

$$y = y(x_1, x_2, ..., x_n) \quad \Longrightarrow \quad \Delta y = \sum_{i=1}^{n} \left\| \frac{\partial y}{\partial x_i} \Delta x_i \right\| \tag{6.13}$$

$$\begin{aligned} \Delta\lambda &= \Delta\lambda_{T+rhl} + \frac{P_{el} d_s}{2A^2 \Delta T} \Delta A + \frac{d_s}{2A\Delta T} \Delta P_{el} + \frac{P_{el}}{2A\Delta T} \Delta d_s = \\ &= \lambda \left(2\% + 0.5\% + 1\% + \frac{\Delta d_s}{d_s} \right) = \lambda \left(3.5\% + \frac{0.2\,\mathrm{mm}}{d_s} \right) \end{aligned} \tag{6.14}$$

For the specific task of measuring the effective thermal conductivity of perlite, two samples of the powder with masses $m_1 = 76.55\,\mathrm{g}$ and $m_2 = 76.07\,\mathrm{g}$ were filled in special cloth bags. Before the measurements were started, the samples were baked out at $T = 150\,°\mathrm{C}$ and $p < 10^{-3}\,\mathrm{mbar}$ for a duration of 28 h. When the samples were removed after the measurements were finished, the masses were $m_1 = 75.31\,\mathrm{g}$ and $m_2 = 74.69\,\mathrm{g}$. Assuming that the mass decrease is only due to the evaporation of water which is contained in the sample, one obtains a moisture content of 1.7 % weight (see section 6.4 for further investigation regarding moisture content). For the evaluation of the measurements, it is supposed that the samples were completely dry. The temperature differences between hot and cold plates for the correction method were $\Delta T_1 = 10\,\mathrm{K}$ and $\Delta T_2 = 20\,\mathrm{K}$.

6.2.2 Presentation and Evaluation of Measurement Results

Because the radiative thermal conductivity has already been determined from the FTIR spectroscopy measurement (see section 6.1.2), the next mode of heat transfer to be investigated is solid conduction. According to equation 6.1, if gaseous conduction and coupling are suppressed ($p < 10^{-3}\,\mathrm{mbar}$), the solid heat conductivity λ_s at a certain temperature T and density ρ can be determined by measuring the total effective thermal

conductivity and subtracting the radiative thermal conductivity λ_r, which is calculated from equation 6.10. For this purpose, different measurements were performed in the fully evacuated vacuum chamber at different mean temperatures between 20 °C and 150 °C. The sample density was varied by applying an external loading pressure via the piston. The obtained experimental values for the solid thermal conductivity at different densities are depicted in figure 6.6. A linear correlation is observed. From empirical findings, λ_s is expected to scale with ρ^γ (see section 4.2), where γ can have values between 1 and 2. In this case, the linearity corresponds to $\gamma = 1$ and is therefore in good accordance with theory. In literature, a value close to 1 ($1.1 \leq \gamma \leq 1.3$) can be found for fumed silica, a material which is quite comparable to perlite [93]. Furthermore, $\gamma \approx 1$ was also determined for polyimide foams [94].

The height of the error bars in figure 6.6 was computed by adding the errors of the effective thermal conductivity measurement (equation 6.14) and the errors of the calculated values for λ_r, which are mostly caused by the error of the extinction (see equation 6.9).

Different values of λ_s were measured at equal densities, but different mean temperatures. However, no explicit temperature dependency could be observed, although $\lambda_s \sim T^{-1}$ is predicted from theory. A possible explanation is, that this relation is only valid for crystalline solids. For amorphous materials like SiO_2, it has even been observed that λ_s slightly rises with temperature [73]. Therefore, the temperature-dependence of λ_s for perlite, if existing, is assumed to be smaller than the indicated error and neglected from now on.

From the linear fit (black line), one obtains the following relation between solid thermal conductivity and density, including standard deviations of the fit parameters:

$$\lambda_s = \left((0.326 \pm 0.010) \cdot \rho \left[\frac{kg}{m^3} \right] - (15.4 \pm 0.7) \right) \cdot 10^{-3} \, \frac{\mathrm{W}}{\mathrm{mK}} \tag{6.15}$$

In the next step, effective thermal conductivity measurements at gas pressures between $0.1\,\mathrm{mbar} \leq p \leq 1000\,\mathrm{mbar}$ were done in order to examine conduction via the pore gas on the one hand and the coupling effect on the other hand. A first series of measurements was recorded at a temperature of $T = 20\,°\mathrm{C}$ and a bulk density of $\rho = 76.3\,\mathrm{kg/m^3}$. For the evaluation, the pure contribution of gaseous conduction and coupling was determined. For this purpose, the radiation and solid thermal conductivities at the given temperature and density of the sample were calculated according to equations 6.10 and 6.15. Subsequently, the values for λ_r and λ_s were subtracted from the measured effective thermal conductivity λ_{eff} to obtain the sum of $\lambda_g + \lambda_c$. The result of this procedure is shown in figure 6.7 (blue points), where $\lambda_g + \lambda_c$ is plotted as a function of pressure. The length of the error bars was calculated by adding the measurement error of λ_{eff} (equation 6.14), the systematic error of λ_r, which is mainly caused by the extinction e^*, (equation 6.9) and the statistical error from the linear fit for λ_s (equation 6.15).

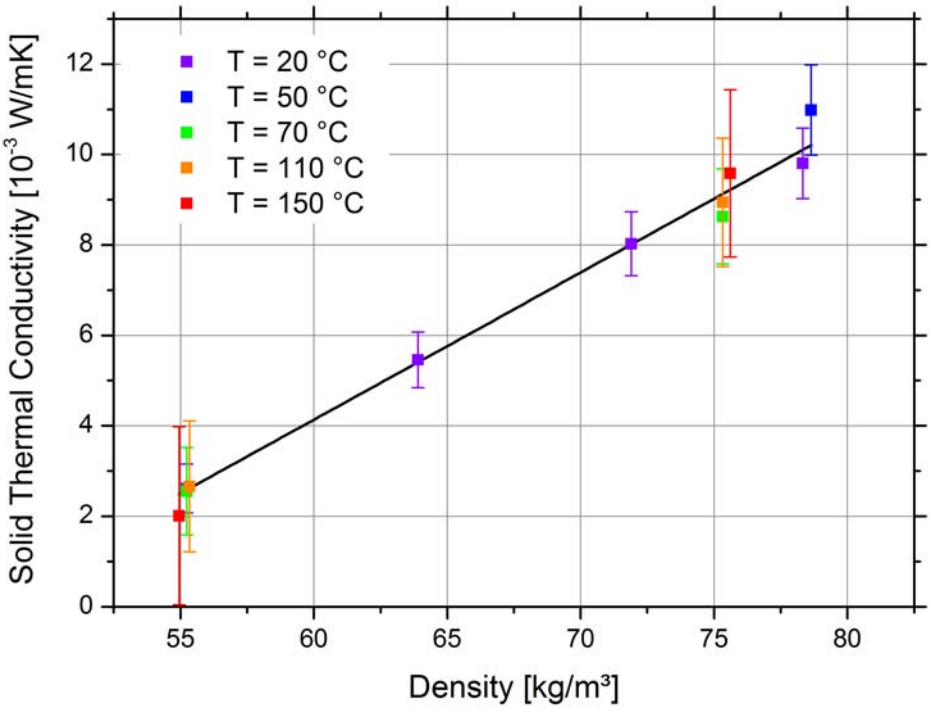

Figure 6.6: Solid Thermal Conductivity λ_s as a function of bulk density, measured in a parallel plate setup.

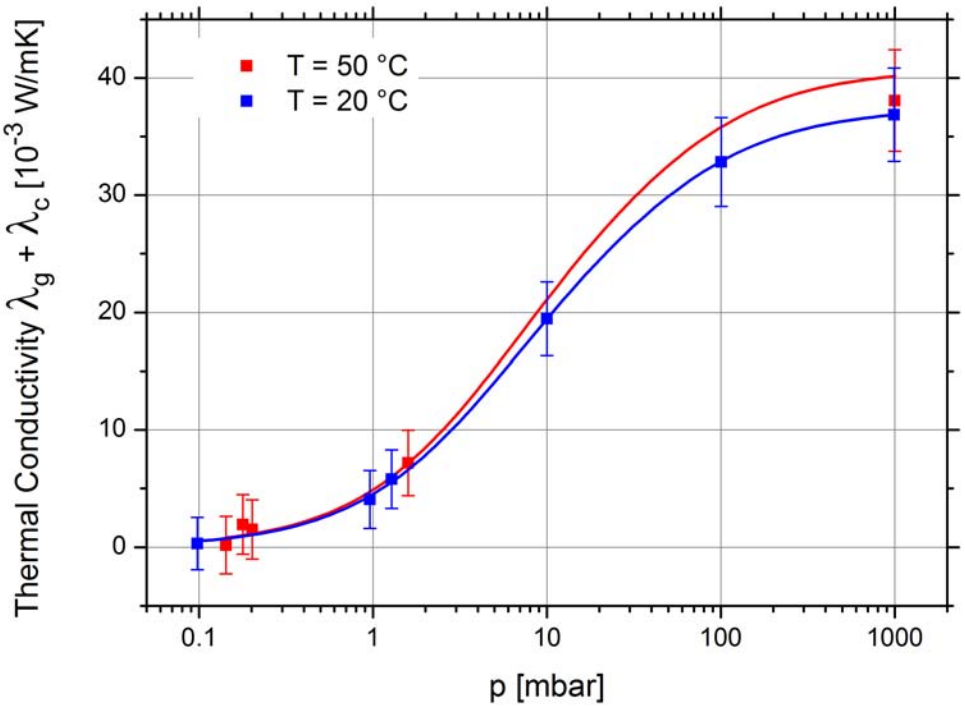

Figure 6.7: Sum of Gaseous Conduction λ_s and Coupling Effect λ_c as a function of pressure, measured in a parallel plate setup.

For the interpretation of the experimental data, the well-known relation for gas heat conduction (equation 4.4) and the model for coupling developed in section 4.4 was used. Initially, the more precise version of the coupling model (equation 4.31) was applied:

$$\lambda_g + \lambda_c = \frac{\lambda_0}{1 + \frac{p^g_{1/2}}{p}} + (1 - \Pi) \left[\frac{1 - \Gamma}{\lambda^*_s} + \Gamma \left(\frac{\lambda_0}{1 + \frac{p^c_{1/2}}{p}} \right)^{-1} \right]^{-1} \tag{6.16}$$

The measurement values from figure 6.7 at $T = 20\,°\text{C}$ were used to fit the parameters $p^g_{1/2}$, Π, Γ λ^*_s and $p^c_{1/2}$ in equation 6.16 using the software ORIGIN PRO 8.5.1 G. Table 6.2 shows the obtained results and their statistical errors. The quantity λ_0 was defined as a constant with $\lambda_0 = 25.7 \cdot 10^{-3}\,\text{W/mK}$, which is the continuum thermal conductivity of air at $T = 20\,°\text{C}$ [34]. It was observed that the outcome of the fitting procedure depended on the settings of the initial values. Especially the results for λ^*_s, Π and Γ varied dramatically, and their errors were unreasonably high in most cases. After testing different combinations, a setting of initial values was chosen that resulted in relatively low errors. They are also included in table 6.2.

	λ_0 [10^{-3} W/mK]	$p^g_{1/2}$ [mbar]	Π [1]	Γ [1]	λ^*_s [10^{-3} W/mK]	$p^c_{1/2}$ [mbar]
value	25.7	5.1	0.87	0.28	35157	39.3
error	0	0.7	$1.2 \cdot 10^6$	$2.6 \cdot 10^6$	$4.5 \cdot 10^{11}$	$11 \cdot 10^3$
initial value	25.7	5	0.9	0.4	2000	40

Table 6.2: Parameters for gaseous conduction and coupling according to equation 6.16, obtained by fitting the experimental data from figure 6.7 at $T = 20\,°\text{C}$.

Still, it has to be said that these results are not very expressive due to the high errors, which are in some cases seven orders of magnitude larger than the indicated values. This is also due to the fact that many parameters were fitted simultaneously, and therefore the calculation has many degrees of freedom. Especially the value for λ^*_s has a very large error margin.

Nevertheless, the results from table 6.2 support the assumption from section 4.4 and show that the term in equation 6.16, which describes the solid contribution to the coupling effect, can be neglected. The widely varying value of λ^*_s only proofs that the fitting results are independent of the choice of λ^*_s. Therefore, the simplified coupling model according to equation 4.32 was applied:

$$\lambda_g + \lambda_c = \frac{\lambda_0}{1 + \frac{p^g_{1/2}}{p}} + \Phi \frac{\lambda_0}{1 + \frac{p^c_{1/2}}{p}} \tag{6.17}$$

This time, the parameters $p^g_{1/2}$, Φ and $p^c_{1/2}$ were fitted according to equation 6.17. The results are shown in table 6.3.

	λ_0 [10^{-3} W/mK]	$p^g_{1/2}$ [mbar]	Φ [1]	$p^c_{1/2}$ [mbar]
value	25.7	5.1	0.46	39.3
error	0	0.3	0.02	8.7
initial value	25.7	5	0.4	50

Table 6.3: Parameters for gaseous conduction and coupling according to equation 6.17, obtained by fitting the experimental data from figure 6.7 at $T = 20\,°\mathrm{C}$.

It showed that the results of the fitting procedure were largely independent of the selection of initial values, and any reasonable combination yielded the same outcome with relatively small errors. The results for $p^g_{1/2}$ and $p^c_{1/2}$ are identical to the values from table 6.2, and $\Phi = (1 - \Pi)/\Gamma = 0.46$ from table 6.3 agrees with $\Pi = 0.87$ and $\Gamma = 0.28$ from table 6.2 (see section 4.4 for the definition of Φ). These facts are considered as further indications that the simplified coupling model (equation 4.32) is appropriate to describe the coupling effect in perlite with sufficient accuracy. As a consequence, the values from table 6.3 were used to draw the fitting curve (blue) in figure 6.7 according to equation 6.17. The agreement with the measured data is striking.

Considering the results from table 6.3, the following findings can be stated:

- The coupling thermal conductivity in the continuum is $\lambda_c = (11.8 \pm 0.5) \cdot 10^{-3}$ W/mK, which can be calculated from $\Phi = 0.46 \pm 0.02$ and $\lambda_0 = 25.7 \cdot 10^{-3}$ W/mK.

- With the relation $p_{1/2} = 230\,\mathrm{mbar}/\left(d_c\,[\mu\mathrm{m}]\right)$, which is valid for air (section 4.1), the fitted values for $p^g_{1/2}$ and $p^c_{1/2}$ can be converted to effective characteristic lengths. From $p^g_{1/2} = (5.1 \pm 0.3)$ mbar for gas heat conduction inside the pores, one obtains an effective pore diameter of $d_p = (45.1 \pm 2.7)$ µm.

- The characteristic pressure $p^c_{1/2} = (39.3 \pm 8.7)$ mbar for the coupling effect corresponds to $d_g = (5.9 \pm 1.3)$ µm, which is the effective distance between the grains. Hence, d_g would be smaller than the effective pore diameter by a factor of roughly 8. In order to proof, whether this result for d_g is realistic, the mean distance between two equally-sized grains is calculated (figure 6.8 a) according to:

$$\bar{d}_g = 2\bar{l} = 2\left(r_g - \bar{y}\right) = 2\frac{\int_0^{\pi/2}\left(r_g - r_g\cos\varphi\right)d\varphi}{\int_0^{\pi/2} d\varphi} = 2r_g\left(1 - \frac{2}{\pi}\right) \tag{6.18}$$

  Although TECHNOPERL ® - C 1,5 has grain diameters up to 1.5 mm, the majority of particles is much smaller. From a sieve analysis of the similar material

TECHNOPERL ® - K 2 [95], it is known that most grains (46 % by volume) have diameters between 0.125 mm and 0.5 mm, and only a small fraction of grains is larger. Therefore, the average radius of large particles is assumed to be around $r_g = 0.1\,\text{mm}$. With this input, one obtains $\bar{d}_g = 73\,\mu\text{m}$ from equation 6.18, which is one order of magnitude larger than the experimental result $d_g = (5.9 \pm 1.3)\ \mu\text{m}$. However, some additional assumptions can be made. Initially, the intermediate space can be filled with an additional grain of equal diameter (figure 6.8 b). This case can be approximated by changing the lower limit of the integration in equation 6.18 from zero to $\pi/4$ to obtain $\bar{d}_g = 2r_g\left(1 - \sqrt{8}/\pi\right) = 20\,\mu\text{m}$. By introducing another grain with smaller diameter (figure 6.8 c) and integrating only from zero to $\pi/8$, the result changes to $\bar{d}_g = 2r_g\left(1 - \frac{4}{\pi}\sqrt{2-\sqrt{2}}\right) = 5.1\,\mu\text{m}$, which is in the correct order of magnitude. Indeed, many assumptions and estimations have been made to arrive at this value for the mean distance between the grains, but eventually, the characteristic pressure $p^c_{1/2} = (39.3 \pm 8.7)$ mbar seems reasonable.

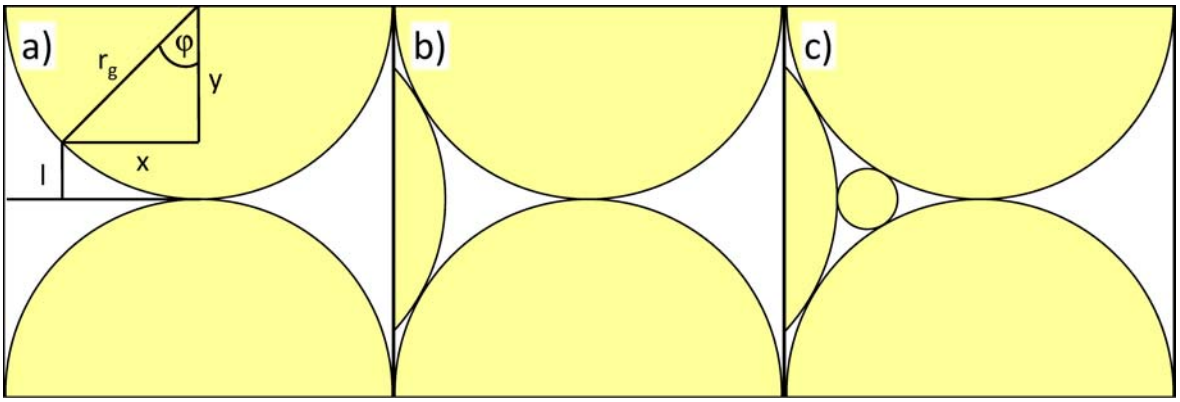

Figure 6.8: Estimation of the mean distance between perlite grains, which is relevant for the characteristic pressure $p^c_{1/2}$ of the coupling effect.

Some additional measurements on gaseous conduction and coupling were performed at $T = 50\,°\text{C}$ (red points in figure 6.7). However, no additional results could be derived from these experiments, because too few measurements were done in the transition regime between $1\,\text{mbar} \leq p \leq 100\,\text{mbar}$ and, as a consequence, the previously described fitting procedure with ORIGIN PRO 8.5.1 G did not converge. Therefore, the red line in figure 6.7 was drawn with the parameters $p^g_{1/2}$, Φ and $p^c_{1/2}$ from table 6.3, which are supposed to be constant within the small temperature difference between $T = 20\,°\text{C}$ and $T = 50\,°\text{C}$. Only the continuum thermal conductivity of air was adjusted to $\lambda_0 = 27.9 \cdot 10^{-3}\,\text{W/mK}$, which is the correct value at $T = 50\,°\text{C}$ [34]. It can be observed that the experimental values for $T = 50\,°\text{C}$ are slightly larger than those for $T = 20\,°\text{C}$ and that the measurement points agree with the calculated curve within the error interval.

In general, it has to be mentioned that the measurements in the parallel plate setup are possibly not fully representative for the thermal conductivity of TECHNOPERL ® - C 1,5 under practical conditions. The reason therefore is, that the compression of the material to high densities was not done by vibrations, which would cause the grains to arrange naturally in a compact way, but rather by applying an external mechanical force via the piston (see figure 6.5). For example, at $\rho = 76.3\,\mathrm{kg/m^3}$, the loading pressure was equal to $p_{ext} = 1.05\,\mathrm{bar}$. With the sample area of $A \approx 0.03\,\mathrm{m^2}$, this corresponds to a force of more than 3.2 kN, which was generated by lead blocks with a total weight of around 330 kg. As a result of this high mechanical load, the material structure may have been damaged. On the one hand, this could have a significant impact on solid conduction due to the shorting of thermal resistances. On the other hand, there might also be a minor effect on the characteristic pressures $p^g_{1/2}$ and $p^c_{1/2}$ due to a decrease of the pore diameters and the gap distances between the grains. In the following section and in chapter 7, an attempt will be made to clarify how large the mismatch is.

6.3 Measurements in a Cut-Off Cylinder Apparatus

From the experiments in the parallel plate setup, first important results for the thermal conductivity of TECHNOPERL ® - C 1,5 were known. However, there were still various questions to be investigated. Therefore, a separate apparatus in cylindrical geometry was set up at the division of ZAE BAYERN in Garching. The main goals, which were pursued with this device, were:

- Confirmation or, if necessary, correction of the measurements in the parallel plate setup.
- Analysis of gas heat conduction in pores and coupling effect using inert gases instead of air.

6.3.1 Conception, Setup and Procedure of the Experiment

Like in the parallel plate apparatus, electrical heatings were used to generate a temperature difference, which is the origin of a heat flux through the perlite sample. Again, the measurements were performed under stationary conditions, which means that all temperatures and heat flow rates are constant with time. In this case, the heat flux through the specimen is equal to the electrical heating power, a quantity that is relatively easy to measure. The main difference to the parallel plate setup is the geometry of the experiment, which is now cylindrical.

Experimental Setup

The layout of the cut-off cylinder apparatus is shown in figure 6.9. The central component is a copper tube (length $l = 27\,\text{cm}$, inner diameter $d_i = 0.8\,\text{cm}$, wall thickness $d_w = 0.1\,\text{cm}$), in which three separate heating cartridges (lengths $l_1 = 5\,\text{cm}$, $l_2 = 16\,\text{cm}$, $l_3 = 5\,\text{cm}$, outer diameter $d_o = 0.8\,\text{cm}$) were inserted (8). Because the cartridges could be heated independently of each other and due to the high thermal conductivity of copper, a homogeneous temperature of the tube could be reached. Using special mountings (10) made of a thick wire (diameter $d = 0.1\,\text{cm}$), the heating element was fixed in the center of the outer tube (length $l = 41.4\,\text{cm}$, inner diameter $d_i = 10.2\,\text{cm}$, wall thickness $d_w = 0.3\,\text{cm}$), which was made of high-grade steel and covered by vacuum flanges on its edges (11). The hollow space was filled with perlite (9). A rotary vane pump [96] (1), which could reach a minimum pressure of $p = 0.02\,\text{mbar}$ in the perlite sample, was used to evacuate the apparatus. Using an arrangement of valves (2,3,5) including a high-precision needle valve (3), the vacuum pressure could be adjusted, and the gases air (from the laboratory room) or argon and krypton (from gas bottles) could be inflated (4). Two capacitive pressure transducers [96] (6,7) with complementing measurement ranges were used to determine the vacuum pressure in the interval $0.01\,\text{mbar} \leq p \leq 100\,\text{mbar}$. A special property of capacitive sensors is, that the principle of measurement does not depend on the gas species.

Temperatures were measured with Pt-100 resistances, their locations are shown in figure 6.9. A multimeter was used to measure the voltage signals of the pressure transducers, the Pt-100 resistances and the electrical heating power. It was connected to a computer to visualize and archive the experimental data. The temperature of the copper tube with its three individual heating zones was regulated with PID controllers and was set to $T_{in} = 150\,°\text{C}$ during all measurements. For the middle zone, a hardware controller was used, and for the two marginal zones, two software controllers were implemented on the measurement computer. Because the electrical power of the controllers' voltage output was not sufficient, an amplifier (13) was used. For the determination of the electrical heating power P_2 of the middle zone, the output voltage V_2 of the amplifier and the heating current $I_{el,2}$ as the voltage drop over a high-precision shunt ($R_s = 0.500\,\text{m}\Omega$) were measured with the multimeter and multiplied according to $P_2 = U_2 \cdot I_{el,2}$. The electrical heating powers P_1 and P_3 of the marginal zones were calculated from $P_i = U_i^2/R_i$, where U_i are the respective measured output voltages of the amplifier and R_i are the resistances of the heating cartridges. This method is slightly less accurate than the determination of P_2, because the resistances R_i are temperature-dependent and cannot be measured during operation. However, the values of R_i were determined regularly between different series of thermal conductivity measurements. The individual contributions P_1, P_2 and P_3 were added to obtain the total electrical heating power P_{el}. For the feed-through of cables (13) to the inner Pt-100 resistances and to the heating cartridges, a special vacuum-tight flange with pin contacts on its inner and outer side was used.

To control the temperature of the outer high-grade steel pipe ($T_{out} = 50\,°C$), electrical heatings were applied as well, because a cooling system would have been connected with considerable additional amounts of effort and expenses. Just like for the inner copper tube, three individual heating zones were installed. For the pipe itself, a heating tape and another hardware PID controller were used. On the flanges, two selfmade wire heatings, which were controlled manually, were assembled. The electrical power of the outer heatings was not measured, because it is irrelevant for the thermal conductivity of the investigated samples, as long as the temperature T_{out} is constant. In order to thermally decouple the apparatus from its surroundings, it was coated with a heat insulation (12). A selection of photographs of the device and its components is shown in figure 6.10.

Measurement Procedure

For the preparation of the experiments, the heatable copper tube was mounted inside the pipe (figure 6.10 e). Subsequently, the cables of the temperature sensors and heating cartridges were connected, and the electrical feed-through flange was attached. The pipe was filled with perlite (figure 6.10 f) and sealed with the second flange afterwards. At the end, the vacuum connections to the pump were established, and remaining cables were plugged in. The exact amount of perlite was weighed with a high precision balance. From $m = 229.03\,g$ and the void volume of the outer pipe ($V = 3.358 \cdot 10^{-3}\,m^3$), a bulk density of $\rho = 68.2\,kg/m^3$ was calculated. After the perlite filling, the material was baked out at $T_{in} = 150\,°C$, $T_{out} = 50\,°C$ and $p < 0.1\,mbar$ for approximately 96 hours.

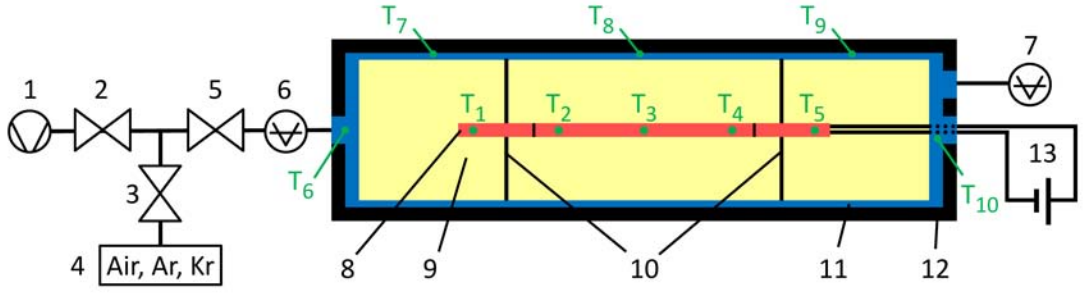

1 Vacuum pump
2 Pump valve
3 Valve for gas inflation
4 Gas reservoir (air, argon or krypton)
5 Safety valve
6 Pressure sensor (1 mbar < p < 100 mbar)
7 Pressure sensor (0.01 mbar < p < 1 mbar)
8 Three-zone cartridge heater
9 Perlite
10 Centering facilities
11 Tube with vacuum flanges on both edges
12 Thermal insulation
13 Electrical power supply with cables
T_i Temperature sensors

Figure 6.9: Schematic layout of the cut-off cylinder apparatus.

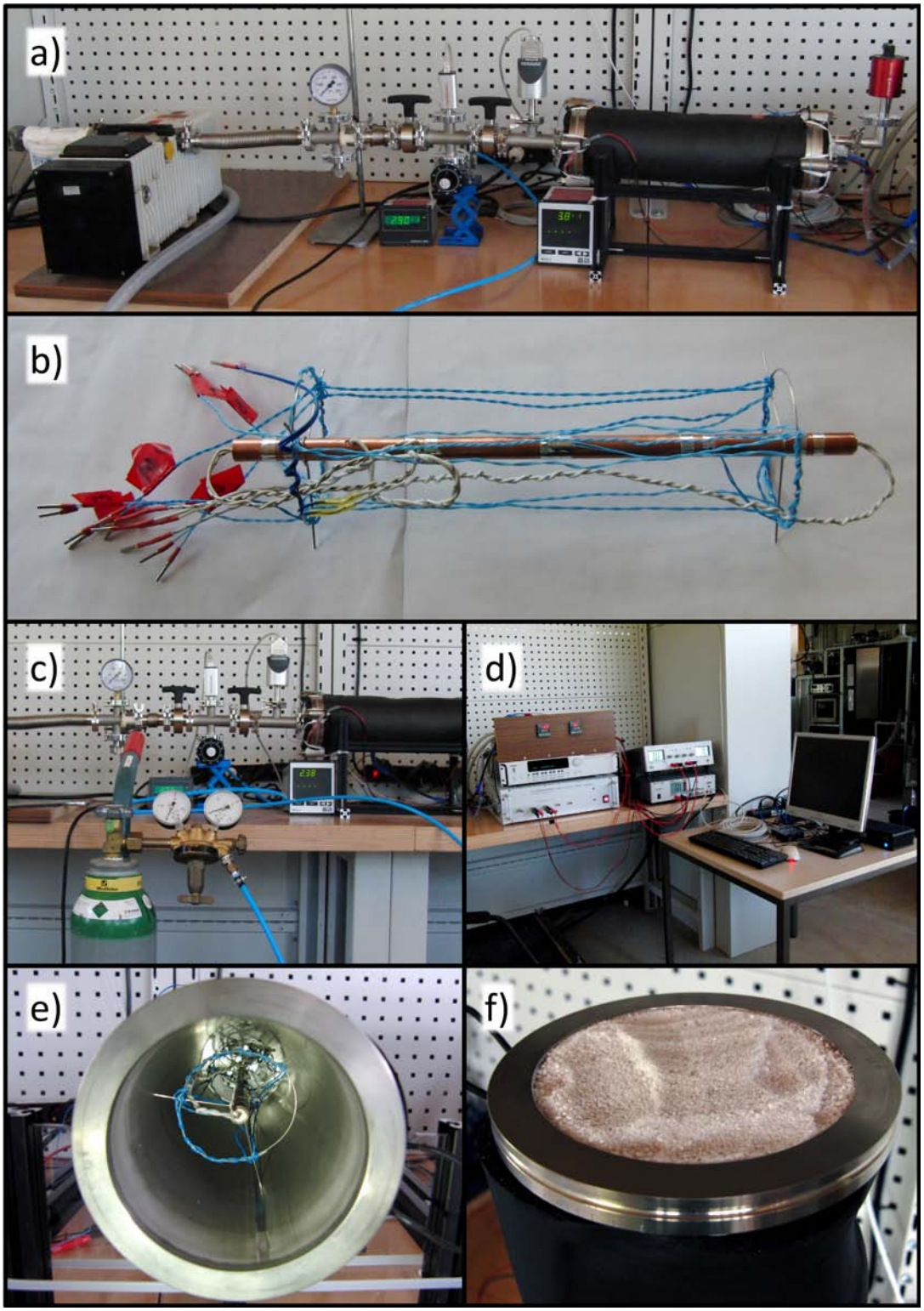

Figure 6.10: Photographs of the cut-off cylinder apparatus: Overview of the device with vacuum pump, valves, tube with thermal insulation and pressure sensors (a), three-zone heatable copper tube with mountings, Pt-100 sensors and cables (b), gas inflation with argon bottle and pressure reducing valve (c), measurement and control technology with PID-controllers, multimeter, amplifier, power supplies and measurement computer (d), mounting of the heating element (e), perlite filling (f).

For every measurement point, the respective pressure was set using the vacuum pump and the high-precision needle valve. The adjustment of temperatures was slightly more challenging, because the three control circuits influenced each other when running simultaneously with a nominal value of $T_{in} = 150\,°\mathrm{C}$. This was a result of errors in temperature measurement and a disadvantageous effect of the high thermal conductivity of copper. However, the problem could be solved with the following procedure: Initially, the middle zone was set to $T = 148\,°\mathrm{C}$. Afterwards, the marginal zones were activated with a nominal value of $T = 150\,°\mathrm{C}$. As soon as the control variables and the temperatures at the borders had become stationary, the output value was set manually, and the automatic control was switched off again. Because the middle zone was still slightly below $T = 150\,°\mathrm{C}$, the set point was increased until the average temperature of the sensors T_1 to T_5 was as close as possible to the nominal temperature of $T_{in} = 150\,°\mathrm{C}$. The adjustment of the outside temperatures was less critical, because the two flange heatings could be regulated manually. When stationary conditions were reached, all relevant data was recorded for a total duration of 9 hours. For the evaluation, the measured values of all temperatures, pressures and electrical heating powers were averaged over the whole time interval. Subsequently, the mean value of the temperatures T_1 to T_5 was calculated to obtain the average inner temperature T_{in}. In analogy, the data from T_6 to T_{10} was used to determine the average outer temperature T_{out}. At the end, the temperature difference was calculated according to $\Delta T = T_{in} - T_{out}$.

Measurement Errors

For the analysis of the experimental data, the following **systematic errors** have to be considered:

Pressure measurement: According to the operating manuals of the capacitive pressure transmitters (PFEIFFER CMR 364 [97] and LEYBOLD CERAVAC CTR 100 [98]), the relative measurement error is given by $0.2\,\%$. Due to temperature-related effects, another contribution of up to $0.7\,\%$ has to be added, yielding a systematic error of around $1\,\%$ in total.

Temperature measurement: The Pt-100 temperature sensors are specified according to IEC 60751 class A, which means that they have an absolute error of $0.15\,°\mathrm{C}$ plus a relative error which is given by $0.2\,\%$ of the measurement value (in °C). For $T = 150\,°\mathrm{C}$, this corresponds to a total error of $0.5\,°\mathrm{C}$. However, deviations between the single sensors of around $\pm 1\,°\mathrm{C}$ were observed in situations where the temperature should have been perfectly homogeneous. As a consequence, this value is assumed to be the total absolute error.

For the conversion of the measured resistances into temperatures, a quadratic correlation was implemented in the measurement software:

$$R = R_0 \left(1 + AT[°\mathrm{C}] + B\,(T[°\mathrm{C}])^2\right) \tag{6.19}$$

The parameters are $R_0 = 100\,\Omega$, $A = 3,9083 \cdot 10^{-3}$ and $B = -5.775 \cdot 10^{-7}$. This method is specified in the German industry standard DIN EN 60751 and suitable for temperatures between $T = 0\,°C$ and $T = 850\,°C$ [99, 100]. Although the quadratic relation is only an approximation, and terms of higher order are also existing, this conversion method is supposed to be sufficiently accurate, so that no additional errors are considered.

Electrical heating power: The accuracy of the multimeter for DC voltage measurements is in the range of $0.01\,\%$, and the error of the shunt resistance, which was used to measure the current in the middle zone of the heating element, is given by $0.1\,\%$. The voltage drop across the shunt resistance is irrelevant, because the heating voltage was measured directly at the heating cartridge. However, as an additional error source, voltage and current were not measured exactly simultaneously, but with a delay of around $t = 1\,\mathrm{s}$. In the stationary case, the correlated error should become zero though, because both voltage and current are constant. Altogether, a systematic error of $0.2\,\%$ is estimated for the electrical heating power P_2 in the middle zone of the heating element.

As already mentioned, the measurement of the electrical heating power of the marginal zones was less accurate, because the resistances R_1 and R_3 of the heating cartridges varied between the measurement series. Whereas a relatively high relative error of $4.6\,\%$ was obtained for the experiments with air, the deviations were much smaller for the measurements with argon ($0.2\,\%$) and krypton ($1\,\%$).

The propagation of systematic errors follows equation 6.20:

$$y = y(x_1, x_2, ..., x_n) \quad \Longrightarrow \quad \Delta y_{sys} \;=\; \sum_{i=1}^{n} \left\| \frac{\partial y}{\partial x_i} \Delta x_i^{sys} \right\| \tag{6.20}$$

In addition, there are also **statistical errors**, because all quantities were measured over an interval of 9 hours. They are equal to the standard deviations of the measurement data from the mean values. The statistical errors were below $0.1\,\%$ for the inner temperatures T_1 to T_5 and below $1\,\%$ for the outer temperatures T_6 to T_{10}, which is an indication that the condition of stationarity was well-fulfilled. Due to leakages of the apparatus, a constant pressure increase with time was noticeable, which resulted in statistical errors from $0.1\,\%$ up to $3\,\%$. The oscillations of the electrical heating power were below $1\,\%$.

According to the laws of error propagation, equation 6.21 has to be used for statistical errors:

$$y = y(x_1, x_2, ..., x_n) \quad \Longrightarrow \quad \Delta y_{stat} \;=\; \sqrt{\sum_{i=1}^{n} \left(\frac{\partial y}{\partial x_i} \Delta x_i^{stat} \right)^2} \tag{6.21}$$

For every quantity, the **total error** is calculated by adding the systematic and the statistical error:

$$\Delta y_{tot} = \Delta y_{sys} + \Delta y_{stat} \tag{6.22}$$

6.3.2 Presentation and Discussion of Measurement Results

Calibration of the Apparatus

Because of the truncated cylindrical geometry of the device, equation 2.4 is not applicable, since it is only valid for cylinders with infinite length. As the length of the outer tube is relatively small compared to its diameter, the additional heat flux at the boundaries can not be neglected. The heat transport in this specific geometry can only be treated by introducing a shape factor S (equation 2.6). In addition, a heat flux $\dot{Q}_{cab}$ due to the electric supply cables for Pt-100 sensors and heating cartridges occurs, which is independent of the heat flux through the perlite sample. It may not be taken into account for the calculation of the thermal conductivity. In order to quantify these two effects, the apparatus had to be calibrated first, which was done by a first measurement series of the electrical heating power at different air pressures ($0.02\,\text{mbar} \leq p \leq 1000\,\text{mbar}$). Due to the above considerations, the following equation was used:

$$\begin{aligned} P_{el} &= S\lambda_{eff}\Delta T + \dot{Q}_{cab} = S\left(\lambda_g + \lambda_c\right)\Delta T + S\left(\lambda_s + \lambda_r\right)\Delta T + \dot{Q}_{cab} \\ &= S\left(\lambda_g + \lambda_c\right)\Delta T + \dot{Q}_0 \end{aligned} \tag{6.23}$$

Hence, the electrical heating power consists of two components:

- The first contribution is a pressure-independent part Q_0, which includes the radiative heat transport and solid conduction within the sample and the heat flux $\dot{Q}_{cab}$ due to the supply cables. $\dot{Q}_0$ is a constant, because the shape factor and all temperatures are the same for all experiments. Therefore, also λ_s and λ_r are constant. The value of $\dot{Q}_0$ can be obtained from the calibration measurement by extrapolating the measured values to $p = 0$. An experimental determination could not be realized, because the lowest achievable pressure in the apparatus as a result of vacuum pump limitations and leakages was only $p = 0.02\,\text{mbar}$. At this value, gas heat conduction is still present to a small extent.
- The second part of the electrical heating power involves gaseous conduction in the pores and the coupling effect. It is therefore pressure-dependent. The shape factor S is the second important quantity that has to be determined from the calibration.

Furthermore, a third addend has to be considered, because there is an additional kind of heat flux that initially flows through the cables up to a certain transition point and then takes its path through the perlite. In the general case, this heat flux is neither included in $\dot{Q}_{cab}$, nor exactly proportional to λ_{eff}. For a precise treatment of this situation, one would have to consider a series connection of thermal resistances and calculate the heat flux according to the temperature distribution. However, the maximum possible

rate of heat transfer from the heating element to the transition point is supposed to be much larger than the heat flux from the cable through the perlite sample. This assumption is mainly supported by the fact that the thermal conductivity of the sample is between 0.005 W/mK and 0.05 W/mK and thus much smaller than the heat conductivity of the metal cables, which is in the order of 100 W/mK. As a consequence, this effect is in first order linear to λ_{eff}. Its solid and radiative part is contained in $\dot{Q}_0$, whereas the contributions of gas conduction and coupling effect increase the shape factor S. These assumptions are to be verified by the results of the calibration measurement (see equation 6.28).

The shape factor can roughly be estimated, if the geometry of the cut-off cylinder apparatus is approximated by a purely cylindrical geometry. From comparison of equation 2.6 with equation 2.4 and with the relevant dimensions of the device ($H = 0.27$ m, $r_{in} = 5$ mm, $r_{out} = 51$ mm), one obtains:

$$S_{app} = \frac{2\pi H}{\ln\left(r_{out}/r_{in}\right)} = 0.73\,\mathrm{m} \tag{6.24}$$

Furthermore, the mean temperature $\bar{T}$ of the sample, which is necessary for the determination of the continuum thermal conductivity λ_0 of the filling gases and of the radiative thermal conductivity λ_r, can be calculated from the above approximation. The temperature distribution $T(r)$ in a cylindrical geometry as a function of the radius r is given by [10]:

$$T(r) = T_{out} + (T_{in} - T_{out})\,\frac{\ln\left(\frac{r_{out}}{r}\right)}{\ln\left(\frac{r_{out}}{r_{in}}\right)} \tag{6.25}$$

The average temperature can be calculated via integration and by inserting $T_{in} = 150\,°\mathrm{C}$, $T_{out} = 50\,°\mathrm{C}$, $r_{in} = 5$ mm and $r_{out} = 51$ mm:

$$\begin{aligned} \bar{T}_{app} &= \frac{1}{2\pi\left(r_{out}^2 - r_{in}^2\right)} \int_{r_1}^{r_2} T(r) 2\pi r dr \\ &= T_{out} + (T_{in} - T_{out}) \left(\frac{1}{2\ln\frac{r_{out}}{r_{in}}} - \frac{r_{in}^2}{r_{out}^2 - r_{in}^2} \right) = 70.6\,°\mathrm{C} \end{aligned} \tag{6.26}$$

For more precise values of S and $\bar{T}$, the cut-off cylinder apparatus was reproduced in a CFD simulation with the CAD software SOLIDWORKS 2008 and the add-on COSMOSFLOWORKS 2008. The CFD model consisted of 403,016 cubic cells, which were used for the numerical solution of Fourier's Law in three dimensions (equation 2.1). All geometric dimensions were chosen exactly according to the specifications from section 6.3.1. However, the supply cables for Pt-100 sensors and heating cartridges were

not included in the model. The temperatures $T_{in} = 150\,°C$ of the heating element and $T_{out} = 50\,°C$ of the outer pipe were set as boundary conditions. The interspace was filled with a solid (to exclude convection) with an effective thermal conductivity of $\lambda_{CFD} = 0.01\,W/mK$, which is a realistic value for perlite. Figure 6.11 shows the resulting temperature distribution in the stationary case. The calculated mean temperature was $\bar{T}_{CFD} = 64\,°C$.

It is reasonable that $\bar{T}_{CFD}$ is smaller than $\bar{T}_{app}$, because the distance between the heating element and the flanges is larger than $r_{out} - r_{in}$, and therefore the temperature in a large part of the boundary regions is relatively close to T_{out} (see figure 6.11). The stationary rate of heat transfer, which was calculated in the CFD simulation, was $\dot{Q}_{CFD} = 0.78\,W$. With $\lambda_{CFD} = 0.01\,W/mK$ and $\Delta T = 100\,K$, this corresponds to $S_{CFD} = 0.78\,m$ (equation 2.6). Due to the additional heat flux at the boundaries, it makes sense that S_{CFD} is larger than S_{app}.

With this preliminary knowledge, the cut-off cylinder device was calibrated from a measurement series. The electrical heating power was measured as a function of air pressure, as described in section 6.3.1. The results are shown in figure 6.12. Due to the comparatively high leakage rate χ of the apparatus caused by the relatively large number of vacuum connections, a pressure increase of $\dot{p} \approx 0.04\,mbar/h$ was notable. With $V = 3.358\,l$, this corresponds to $\chi \approx 3.7 \cdot 10^{-5}\,mbar\ l/s$. Therefore, the vacuum pump was constantly operating during the measurements at $p = 0.02\,mbar$, $p = 0.1\,mbar$ and $p = 1\,mbar$, and its delivery rate was reduced respectively with the high-precision needle valve. With this procedure, the leakage rate was compensated for.

For the measurement at ambient pressure ($p \approx 1000\,mbar$), the valve was completely opened, so that the pressure inside the apparatus was equal to the air pressure in the laboratory. The exact value $p = (960 \pm 10)\,mbar$ was read off from a local meteorological station [101]. Because the actually measured temperature difference ΔT_{exp} varied between $99.9\,K$ and $100.4\,K$, the experimental values of P_{el} were divided by ΔT_{exp} and then multiplied by $100\,K$. As a result of this correction, the normalized electrical heating power $\hat{P}_{el}$ always refers to $\Delta T = 100\,K$.

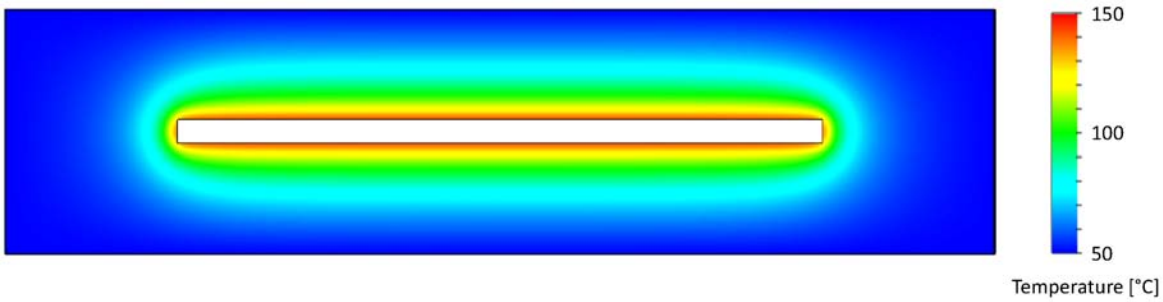

Figure 6.11: Temperature distribution in the cut-off cylinder device, modelled in a CFD simulation.

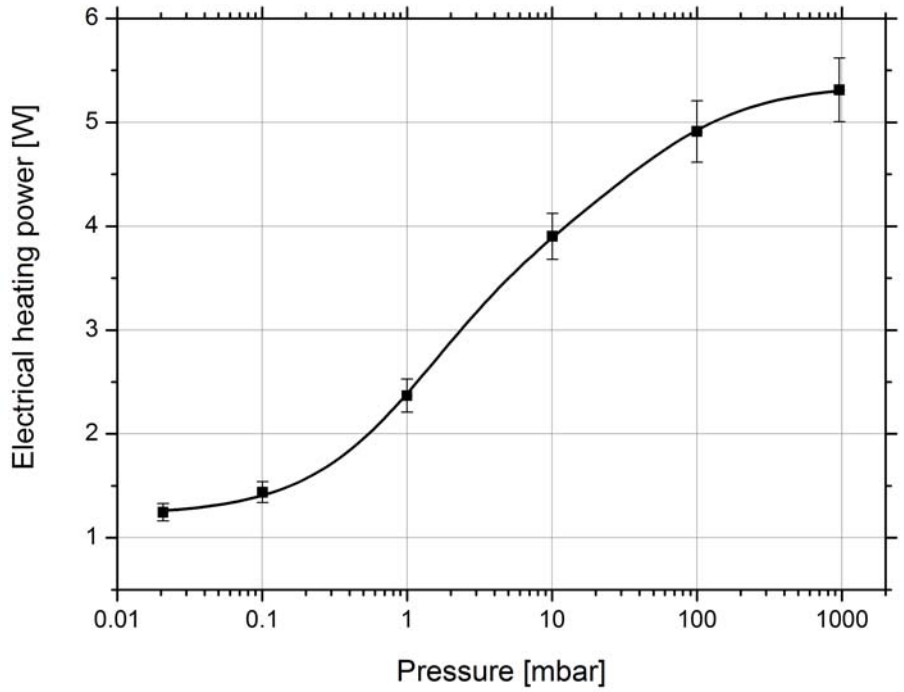

Figure 6.12: Calibration of the cut-off cylinder apparatus. The error of the pressure measurement is covered by the width of the data points.

According to equation 6.23, the experimental data from figure 6.12 can be described with the following relation:

$$\hat{P}_{el} = S\,(\lambda_g + \lambda_c)\,\Delta T + \dot{Q}_0 \tag{6.27}$$

Therefore, the parameters S and $\dot{Q}_0$ were fitted with ORIGIN PRO 8.5.1 G. For the fitting procedure, the temperature difference was set to $\Delta T = 100\,\mathrm{K}$ according to the above normalization of the electrical heating power. The term $\lambda_g + \lambda_c$ was represented by a function, which describes the experimental pressure dependency of these two parameters (figure 6.12) as well as possible. The obtained calibration constants are:

$$\begin{aligned} S &= (0.9319 \pm 0.0089)\ \mathrm{m} \\ \dot{Q}_0 &= (1.2216 \pm 0.0124)\ \mathrm{W} \end{aligned} \tag{6.28}$$

The determination of S and $\dot{Q}_0$ by fitting was the only reasonable method to calibrate the cut-off cylinder device. Looking at figure 6.10 b, it is clear that the geometry of the apparatus is considerably modified by the supply cables, compared to the CFD model (figure 6.11). The cables were intentionally kept at their original length in order to minimize the pressure-independent heat flux $\dot{Q}_0$. If they had been cut to the minimum

distance which had been necessary to connect the Pt-100 sensors and heating cartridges to the electrical feed-through flange, the heat losses $\dot{Q}_{cab}$ would have been significantly increased, and $\dot{Q}_0$ would have come close to the heat flux through the perlite sample due to gaseous conduction and coupling. This situation is not favorable either, because the measured variable should always be distinctly larger than any constant offset signal.

In this context, a typical experimental difficulty becomes notable. Because the supply cables were not shortened in order to keep $\dot{Q}_0$ small, a different kind of additional heat flux is now included in the shape factor: Comparing the experimentally determined shape factor $S = 0.93\,\mathrm{m}$ with the value $S_{CFD} = 0.78\,\mathrm{m}$, which was obtained from the CFD simulation, it shows that S is almost 20 % larger than S_{CFD}. This fact is interpreted as the verification of the assumption at the beginning of this section about the heat flux that initially flows through the supply cables and then takes its path through the perlite insulation. This effect was assumed to be proportional to the thermal conductivity of the perlite sample, and therefore the pressure-dependent part has to be included in the shape factor. Because the cables were not taken into account in the CFD model, the additional heat flux was not regarded in the simulation, and the experimental shape factor has to be larger than S_{CFD}. Due to the high thermal conductivity of the metal cables, the high temperature of the heating cartridges ($T_{in} = 150\,°\mathrm{C}$) can easily be transported into exterior regions, where the remaining insulation thickness of the perlite sample is comparatively small. Therefore, a relatively large heat flux emerges. With this consideration, the difference of 20 % between S and S_{CFD} can be explained. Consequently, it can be said that the three different shape factors for the cut-off cylinder apparatus (S_{app}, which was obtained from a cylindrical approximation of geometry, S_{CFD} from the simulation and S from the calibration measurement) are in good agreement with each other.

In principle, it would have been possible to include all supply cables in the CFD model. However, due to the high number and the complicated geometrical arrangement of the cables (figure 6.10 b), this approach would have involved an intense effort. Furthermore, it is not guaranteed, that a CFD model including all cables really describes the actual geometry of the apparatus with sufficient accuracy. For example, the cables can slip out of their positions during the perlite filling process (figure 6.10 f). Due to these reasons, the fitting method for the determination of S and $\dot{Q}_0$ was chosen, because it better represents the experiments.

As a result of the calibration, the measured electrical heating power can now be converted into the sum of λ_g and λ_c, which is the pressure-dependent part of the effective thermal conductivity:

$$\lambda_g + \lambda_c = \frac{\hat{P}_{el} - \dot{Q}_0}{S\Delta T} \tag{6.29}$$

Equation 6.29 implies a linear correlation, which is shown in figure 6.13. Again, the electrical heating power has to be normalized to $\Delta T = 100\,\mathrm{K}$, because $\dot{Q}_0$ refers to this temperature difference. However, this correction is very small and in the order of 0.1 %. The data points in figure 6.13 indicate the values of the calibration measurement. The error bars for the pressure measurement are covered by the width of the squares.

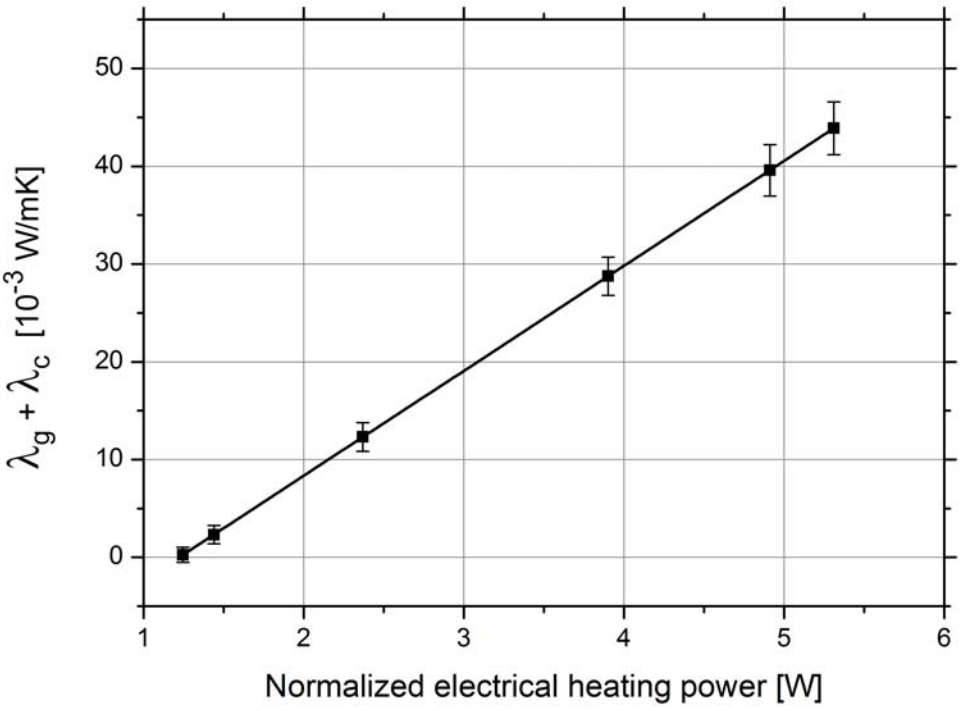

Figure 6.13: Conversion of the normalized electrical heating power into the sum of gas and coupling heat conductivity according to the calibration of the cut-off cylinder apparatus.

Evaluation of the Measurements with Air

With the previously determined calibration constants, it is possible to convert the experimental data of the electrical heating power for the measurement series with air into the sum of $\lambda_g + \lambda_c$. The obtained values are shown in figure 6.14 as a function of pressure. For the evaluation of the measurements, the relevant parameters for gas conduction and coupling were fitted using the same procedure as in section 6.2.2. Due to the results of the parallel plate setup, the simplified coupling model (equation 4.32) was applied. Correspondingly, the relation from equation 6.17 was used:

$$\lambda_g + \lambda_c = \frac{\lambda_0}{1 + \frac{p^g_{1/2}}{p}} + \Phi \frac{\lambda_0}{1 + \frac{p^c_{1/2}}{p}} \tag{6.30}$$

The parameter $\lambda_0 = 28.9 \cdot 10^{-3}$ W/mK [34] was defined as a constant according to the continuum thermal conductivity of air at the mean temperature of the perlite sample ($\bar{T}_{CFD} = 64\,°C$). Table 6.4 shows the obtained results of the fitting procedure.

In comparison with the results from the parallel plate setup (table 6.3), a good agreement can be found. All parameters are within the same order of magnitude. However, the values obtained from the parallel plate measurements for $p^g_{1/2}$ and $p^c_{1/2}$ are higher than those from the cut-off cylinder apparatus. These observations can be explained with the higher density ($\rho = 76.3\,\text{kg/m}^3$) of the measurements in the parallel plate setup (compared to $\rho = 68.2\,\text{kg/m}^3$ in the cut-off cylinder apparatus) and the fact that the material was compressed by external pressure. Consequently, the effective pore diameters and also the intermediate distances between the grains were smaller, which results in higher half-value pressures (see section 4.1).

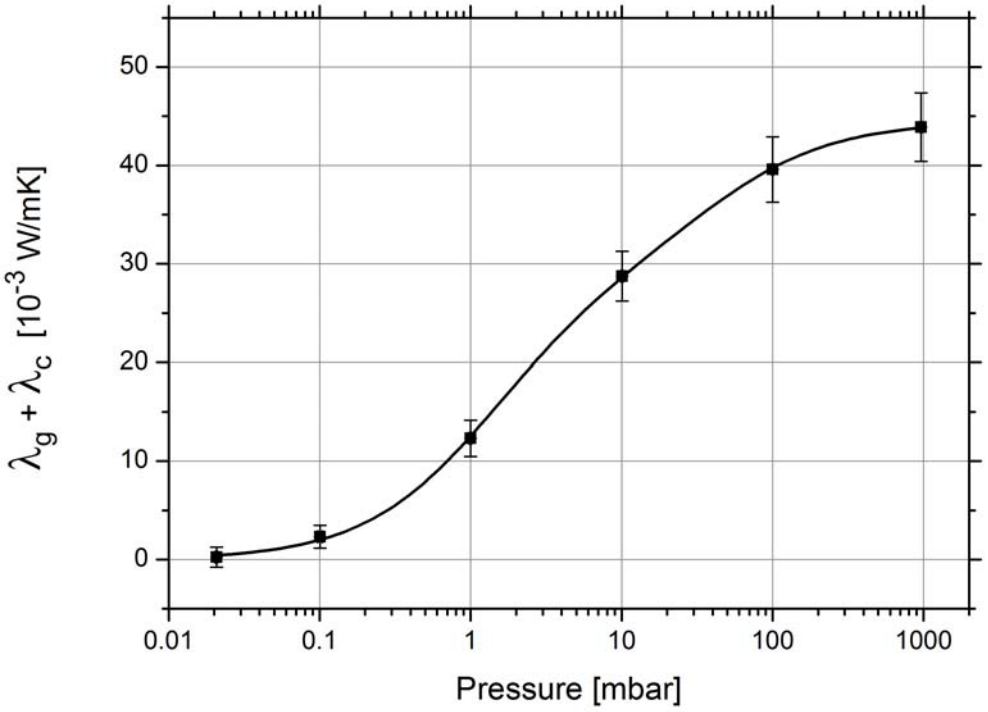

Figure 6.14: Sum of Gaseous Conduction λ_s and Coupling Effect λ_c as a function of air pressure, measured in the cut-off cylinder apparatus.

	λ_0 [10^{-3} W/mK]	$p^g_{1/2}$ [mbar]	Φ [1]	$p^c_{1/2}$ [mbar]
value	28.9	1.38	0.54	38.6
error	0	0.07	0.03	8.1

Table 6.4: Parameters for gaseous conduction and coupling according to equation 6.30, obtained by fitting the experimental data from figure 6.14.

Estimation of the Solid Thermal Conductivity

As shown at the beginning of this section, the calibration constant $\dot{Q}_0$ includes the thermal losses due to supply cables and the heat flux through the perlite sample as a consequence of solid conduction and radiative heat transfer. These single contributions cannot be separated from each other experimentally. However, the solid thermal conductivity λ_s can be estimated, which is the aim of this paragraph.

Initially, the rate of heat transfer through the supply cables is calculated (table 6.5). The following contributions have to be taken into account:

- On the heatable copper tube at the center of the apparatus, 6 Pt-100 temperature sensors (5 measurement points, 1 sensor for the PID controller) with 2 cables each were attached. For the conductor material copper, a thermal conductivity of $\lambda_{copper} = 350\,\mathrm{W/mK}$ is assumed [44].
- The cables for the heating cartridges (6 in total) were made out of nickel with $\lambda_{nickel} = 85\,\mathrm{W/mK}$ [44]. For one of the marginal heating cartridges, the cables had to be extended (see figure 6.10 c), but the extension was relatively short ($l \approx 10\,\mathrm{cm}$) and made out of copper. Its thermal resistance is therefore neglected against the nickel cable.
- The centering facilities (see figure 6.10 b and e) also have to be considered. They were made from welding wire with a diameter of $d = 1$ mm. Consequently, the cross section is equal to $d^2\pi/4 = 0.785\,\mathrm{mm^2}$. The material was W19123 Nb, a high-grade steel with a thermal conductivity of $\lambda_{HGS} = 15\,\mathrm{W/mK}$ [102].

Adding up the single contributions (table 6.5), one obtains $\dot{Q}_{cab} = 0.305\,\mathrm{W}$ for the overall thermal losses due to supply cables. Because the above considerations include several estimations, a general error of 10 % is assumed: $\Delta\dot{Q}_{cab} = 0.031\,\mathrm{W}$.

	Pt-100 cables	cables for heating cartridges	centering facilities
length l	60 cm	30 cm	4.5 cm
cross section A	0.09 mm²	0.5 mm²	0.785 mm²
material	copper	nickel	W19123 Nb
th. conductivity λ	350 W/mK	85 W/mK	15 W/mK
number N	12	6	6
$\dot{Q} = N\lambda\Delta T\frac{A}{l}$	0.063 W	0.085 W	0.157

Table 6.5: Estimation of thermal losses by supply cables and the centering facilities in the cut-off cylinder apparatus.

In the next step, the rate of heat transfer through the perlite sample due to radiation and solid conduction $\dot{Q}_{r+s}$ can be calculated by subtracting $\dot{Q}_{cab}$ from $\dot{Q}_0$:

$$\dot{Q}_{r+s} = \dot{Q}_0 - \dot{Q}_{cab} = (0.917 \pm 0.043)\ \mathrm{W} \tag{6.31}$$

With the shape factor from the calibration and the temperature difference $\Delta T = 100\,\mathrm{K}$, this heat flux can be converted into a thermal conductivity:

$$\lambda_r + \lambda_s = \frac{\dot{Q}_{r+s}}{S\Delta T} = (9.84 \pm 0.56) \cdot 10^{-3}\,\frac{\mathrm{W}}{\mathrm{mK}} \tag{6.32}$$

The radiative thermal conductivity can be calculated from equation 6.10 with the bulk density $\rho = 68.2\,\mathrm{kg/m^3}$ and the radiation temperature $T_r = 375\,\mathrm{K}$ (see equation 4.21):

$$\lambda_r = \frac{16\sigma T_r^3}{3\rho e^*(T_r)} = (6.45 \pm 0.83) \cdot 10^{-3}\,\frac{\mathrm{W}}{\mathrm{mK}} \tag{6.33}$$

Finally, by comparing equations 6.32 and 6.33, one arrives at:

$$\lambda_s = (3.39 \pm 1.39) \cdot 10^{-3}\,\frac{\mathrm{W}}{\mathrm{mK}} \tag{6.34}$$

According to the results of the measurements in the parallel plate setup (equation 6.15), the solid thermal conductivity at $\rho = 68.2\,\mathrm{kg/m^3}$ should be equal to:

$$\lambda_s = (6.83 \pm 1.38) \cdot 10^{-3}\,\frac{\mathrm{W}}{\mathrm{mK}} \tag{6.35}$$

Hence, a considerable deviation of 100 % is noticeable, which can be explained by the fact that the perlite sample was compressed by external pressure in the parallel plate device (see page 67). Therefore, the thermal resistances arising from the material structure were shorted. As a consequence, the result from equation 6.34 is very important, because it describes a material with an undamaged solid structure at a density of $\rho = 68.2\,\mathrm{kg/m^3}$. This topic is investigated further in chapter 7, where an even higher density was reached without applying external pressure.

Evaluation of the Measurements with Argon and Krypton

In order to examine the thermal conductivity of perlite under the influence of inert gases, two measurement series were performed where the filling gas air was replaced with argon and krypton at vacuum pressures between $1\,\mathrm{mbar}$ and $1000\,\mathrm{mbar}$. The individual pressures had to be adjusted using different procedures:

- Just like for the experiments with air, no suitable pressure sensor was available for $p = 1000\,\mathrm{mbar}$. Therefore, the cut-off cylinder apparatus was completely evacuated and then filled with argon or krypton from the gas bottles until $p \approx 1.5\,\mathrm{bar}$.

Subsequently, the needle valve was opened for a short amount of time, so that the gas decompressed until it reached the ambient pressure in the laboratory $p = (960 \pm 10)$ mbar, which was again obtained from the local meteorological station [101].

- For $p = 100\,\text{mbar}$ and $p = 10\,\text{mbar}$, the conventional procedure described in section 6.3.1 was applied, where the vacuum pump and the arrangement of valves was used to adjust the necessary pressure of argon or krypton, which was measured with the capacitive sensor. Just like before, the perlite sample was evacuated until the minimum pressure of the vacuum pump ($p = 0.02\,\text{mbar}$) was reached, before the inert gas was inflated. As already mentioned earlier, the leakage rate of the apparatus was $\chi \approx 3.7 \cdot 10^{-5}\,\text{mbar l/s}$, and therefore a pressure increase of $\dot{p} \approx 0.04\,\text{mbar/h}$ was notable. With the measurement interval of $t = 9\,\text{h}$ for every data point, the partial pressure of air at the end of every measurement was $p_{air} = 0.36\,\text{mbar}$. As a consequence, the requirement $p_{air} \ll p_{inert\,gas}$ is well fullfilled and the total effective thermal conductivity of the gas mixture inside the apparatus is sufficiently close to the thermal conductivity of the pure inert gas (compare equations 4.13 and 8.12 to 8.16).

- For $p = 1\,\text{mbar}$, the partial pressure of air reached the same order of magnitude as the partial pressure of the inert gas. Therefore, a different method had to be applied: After the apparatus was filled with the inert gas at the time t_{fill}, an immediate change of the inner temperatures T_1 to T_5 was notable due to the sudden variation of the thermal conductivity of the sample. After a few hours, at time t_0, all temperatures had become stationary again and the measurement interval of $t = 9\,\text{h}$ ($t = 14\,\text{h}$ for the krypton measurement) was started. At that time, the pressure in the apparatus had already increased by more than $0.2\,\text{mbar}$. During the measurement interval, a linear increase of the vacuum pressure and the normalized heating power was observed (figure 6.15). From a linear fit, the values were extrapolated back to the time t_{fill}, at which the partial pressure of air in the sample was still zero. Apart from the systematic errors due to the measurement equipment, a statistical error had to be considered as well for this method, which was given by the errors of the regression line as a result of the fitting procedure.

The values for the normalized heating power at different pressures, which were obtained from the measurements described above, were converted into the sum of gaseous and coupling thermal conductivity using the calibration constants S and $\dot{Q}_0$. Hence, the sum $\lambda_g + \lambda_c$ can be plotted as a function of pressure, which is shown in figure 6.16. For comparison, the values for air are also included.

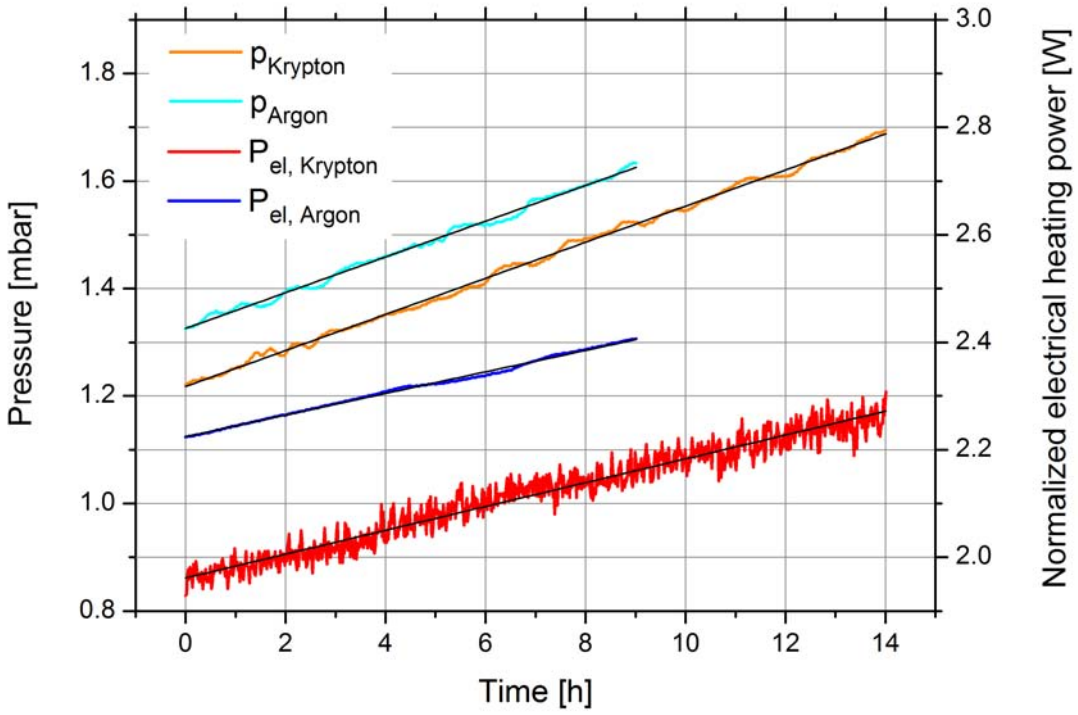

Figure 6.15: Pressures and normalized electrical heating powers during the measurements with argon and krypton with $p = 1\,\text{mbar}$.

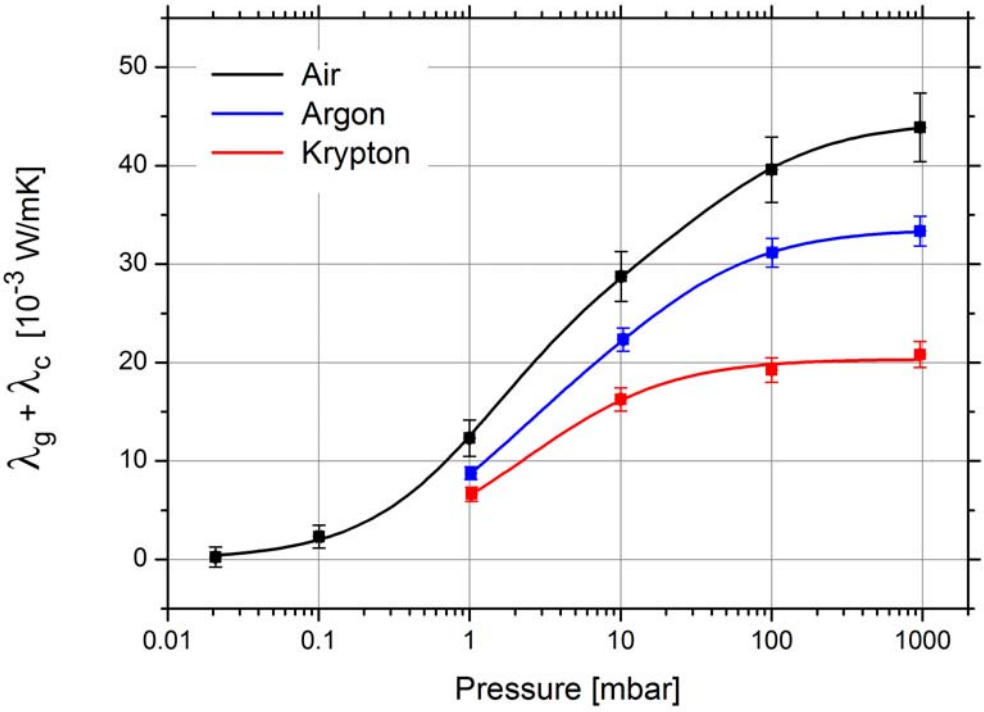

Figure 6.16: Sum of Gaseous Conduction λ_s and Coupling Effect λ_c as a function of pressure for argon, krypton and air, measured in the cut-off cylinder apparatus.

		λ_0 [10^{-3} W/mK]	$p^g_{1/2}$ [mbar]	Φ [1]	$p^c_{1/2}$ [mbar]
air	value	28.9	1.38	0.54	38.6
	error	0	0.07	0.03	8.1
argon	value	19.4	1.46	0.73	17.4
	error	0	0.01	0.01	0.4
krypton	value	10.6	1.24	0.93	4.5
	error	0	0.47	0.06	2.6

Table 6.6: Parameters for gaseous conduction and coupling according to equation 6.30, obtained by fitting the experimental data from figure 6.16.

Like for the previous measurements, the experimental values were fitted to obtain the characteristic pressures $p^g_{1/2}$ and $p^c_{1/2}$ as well as the weighting factor Φ. Once again, the continuum thermal conductivities λ_0 were defined as constants. Because $\lambda_{0,argon}$ and $\lambda_{0,krypton}$ were only available for $T = 25\,°C$ and $T = 100\,°C$ [34], an interpolation to the mean temperature $\bar{T}_{CFD} = 64\,°C$ of the perlite sample was performed. Table 6.6 shows an overview of all parameters for the measurements with air, argon and krypton. Due to the lower thermal conductivity of the inert gases (compare section 4.1), the argon curve (blue) is below the curve for air (black), and the values of $\lambda_g + \lambda_c$ for krypton (red) are even smaller than those for argon (figure 6.16).

It is notable that the characteristic pressure $p^g_{1/2}$ for gas conduction inside the pores stays almost constant, whereas $p^c_{1/2}$ decreases and Φ increases for argon and krypton. In general, it can be theoretically justified that $p_{1/2}$ varies for different kinds of gases: Comparing equations 4.4 and 4.7, one obtains the following relation for the characteristic pressure:

$$p_{1/2} = \frac{5\pi k_B T\,(2f+9)}{16\sqrt{2}d_c\alpha_{red}\,(f+1)\,\varsigma} \sim \frac{2f+9}{f+1}\alpha_{red}^{-1}\varsigma^{-1} \tag{6.36}$$

Therefore, $p_{1/2}$ is determined by the number of degrees of freedom f, the reduced accommodation factor α_{red} and the cross section ς for intermolecular collisions. Because the gas is enclosed in pores or intergranular gaps of perlite, α_{red} refers to the energy exchange between the gas molecules and the perlite surface in this case. It is obvious that the three indicated parameters are different for air, argon and krypton and that the characteristic pressure can not be the same for all three gases. However, because $(2f+9)\,/\,(f+1)$ and ς do not differ greatly (table 6.7), the variation of $p^c_{1/2}$ would have to be caused mainly by the reduced accommodation coefficient. In literature, no values for perlite could be found [103]. Therefore, α_{red} is calculated from equation 6.36.

	$\frac{2f+9}{f+1}$ [1]	ς [10^{-19} m^2]	α_{red} [1]	α [1]
air	3.17	5.33	0.84±0.35	0.91±0.19
argon	3.75	5.29	2.21±0.51	1.38±0.10
krypton	3.75	5.91	7.66±6.03	1.77±0.16

Table 6.7: Determination of the accommodation coefficient α of air, argon and krypton with perlite according to equations 6.36 and 4.11. The values for f and ς can be found in [35].

The effective characteristic distance between the grains $d_c = (5.96 \pm 1.25)$ µm is computed according to $d_c\,[\mu\text{m}] = 230\,\text{mbar}\,/p^c_{1/2}$ (see section 4.1), where the characteristic pressure $p^c_{1/2} = (38.6 \pm 8.1)$ mbar is known from the experiment with air. The temperature $T_{CFD} = 64\,°\text{C} = 337\,\text{K}$ is inserted, which is the mean temperature of the perlite sample. Luckily, the cross sections for air, argon and krypton ς are known at exactly this temperature [35]. With the values of $p^c_{1/2}$ from table 6.6 and the parameters f and ς from [35], the reduced accommodation coefficients for perlite can be calculated (table 6.7). Using equation 4.11, α_{red} is converted into the conventional accommodation coefficient α. Due to the application of equation 4.11, the geometry of the intergranular gaps is approximated by parallel plates.

The calculated values of α in table 6.7 are larger than unity for argon and krypton. From a physical point of view, this result is not reasonable (equation 4.10). However, it is common practice to specify accommodation coefficients greater than one, because α is an experimentally determined quantity [103]. This approach does not indicate a violation of the first law of thermodynamics, it rather shows that the kinetic theory of gases is no longer sufficient to describe all occurring phenomena. Instead, the effects which are related to the interaction of the gas molecules with the perlite surface also have to be included.

As a counter-argument of the whole above reflection about accommodation factors, it is inconsistent though that only the value of $p^c_{1/2}$ varies in table 6.6, while $p^g_{1/2}$ remains almost unchanged. Theoretically, a correlation between both characteristic pressures should be observable. Furthermore, the increase of the weighting factor Φ for the coupling effect is incomprehensible. In section 4.4, it was defined as $\Phi = (1 - \Pi)\,/\Gamma$, where both Π and Γ are only related to the structure and geometry of the porous material. Because the same perlite sample was used for all thermal conductivity measurements, one would expect Φ to stay constant for the experiments with air, argon and krypton.

These inconsistencies can be explained with the assumption that there is a certain fraction of closed pores, which are inaccessible for the inert gases and consequently contain air. Therefore, the characteristic pressure referring to these pores stays constant, which

matches the observation for $p^g_{1/2}$. In addition, the overall thermal conductivity $\lambda_g + \lambda_c$ is increased due to the higher continuum thermal conductivity of air compared to argon and krypton. The only possibility of the fitting procedure to account for this increase is to raise the weighting factor Φ. Thus, the observed effects would become reasonable. However, this assumption of closed pores containing air is not further justified. For clarification, microscopic examinations or similar investigations of the material structure would be necessary.

Nevertheless, it has to be appreciated that the model for the pressure-dependent part of the effective thermal conductivity, which was used in this thesis, is able to represent the measured values of both the parallel plate setup and the cut-off cylinder apparatus. It has to be kept in mind that other models, which are more sophisticated and precise from a theoretical point of view, could not achieve a complete agreement with experimental data [42]. Obviously, there is still a discrepancy between theory and experiments, especially regarding the coupling effect in porous materials. Therefore, it is a great success to obtain an excellent agreement between the measurement values and the fitting model with only three parameters, although the physical interpretation of these parameters is not fully reasonable.

6.4 Determination of the Moisture Content

As a last important experiment, the moisture content w of TECHNOPERL ® - C 1,5 was measured, which is defined as:

$$w = \frac{m_{water}}{m_{sample}} \tag{6.37}$$

For this purpose, the METTLER TOLEDO HR 83 halogen moisture analyzer was used, which is a special measuring instrument for the experimental determination of w. Its main component is a high precision balance, on which the sample is placed (figure 6.17). The investigated perlite sample had been exposed to the humidity of ambient air for a duration of several days. During the measurement in the moisture analyzer, the specimen is heated up by the radiation emitted from a halogen lamp. As a consequence, moisture which is contained in the material, evaporates and escapes. The temperature of the baking-out process can be adjusted by varying the radiation intensity and was set to $T = 200\,°\mathrm{C}$. The time evolution of the sample weight is recorded by the device (figure 6.18). According to the operation manual, it can be measured with an accuracy of $\Delta m = 1\,\mathrm{mg}$ [104]. A total duration of $t = 2\,\mathrm{h}$ was chosen for the experiment.

The following results can be derived from the measurement:

- From the initial mass $m_i = 1\,\mathrm{g}$ and the final mass $m_f = 0.986\,\mathrm{g}$, the moisture content can be calculated:

$$w = \frac{m_{water}}{m_{sample}} = \frac{m_i - m_f}{m_i} = (1.4 \pm 0.2)\ \% \tag{6.38}$$

  This result is in good agreement with $w = 1.7\,\%$, which was obtained in section 6.2. At such low values of w, the only possible heat transfer mechanism connected to moisture, which can have an effect in practice, is gaseous conduction due to water vapor. This impact is relatively harmless, because the thermal conductivities of water vapor and air are almost identical ($\lambda_{wv} = 0.025$ W/mK [34]). The two detrimental effects of moisture were already excluded in section 4.6: Pore diffusion can not happen as a consequence of the phase diagram of water, and flooding of pores with liquid water requires the perlite insulation to be completely wet.

- According to figure 6.18, the sample is already completely dry after a duration of 20 minutes, because its weight is equal to the final value and does not change significantly anymore. This result is important for the thermal conductivity measurements in the parallel plate setup and in the cut-off cylinder apparatus, where the samples were baked out prior to the experiments. Although the ratio of sample surface against volume was worse and the temperature was only $T = 150\,°\mathrm{C}$, the samples can be assumed to be completely dry, because the baking-out process was performed in vacuum and the duration was several hours.

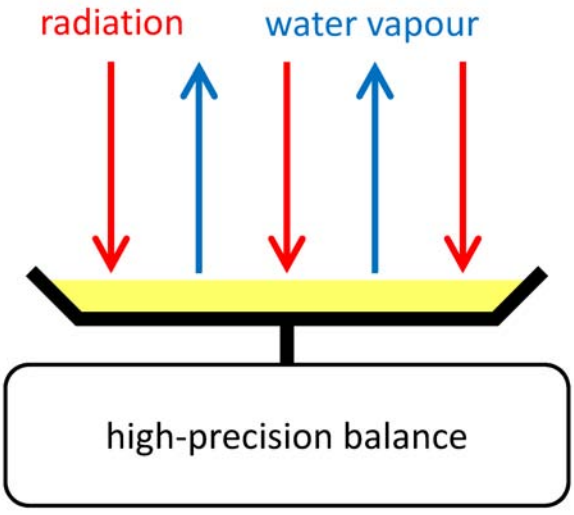

Figure 6.17: Measurement principle for the experimental determination of the moisture content.

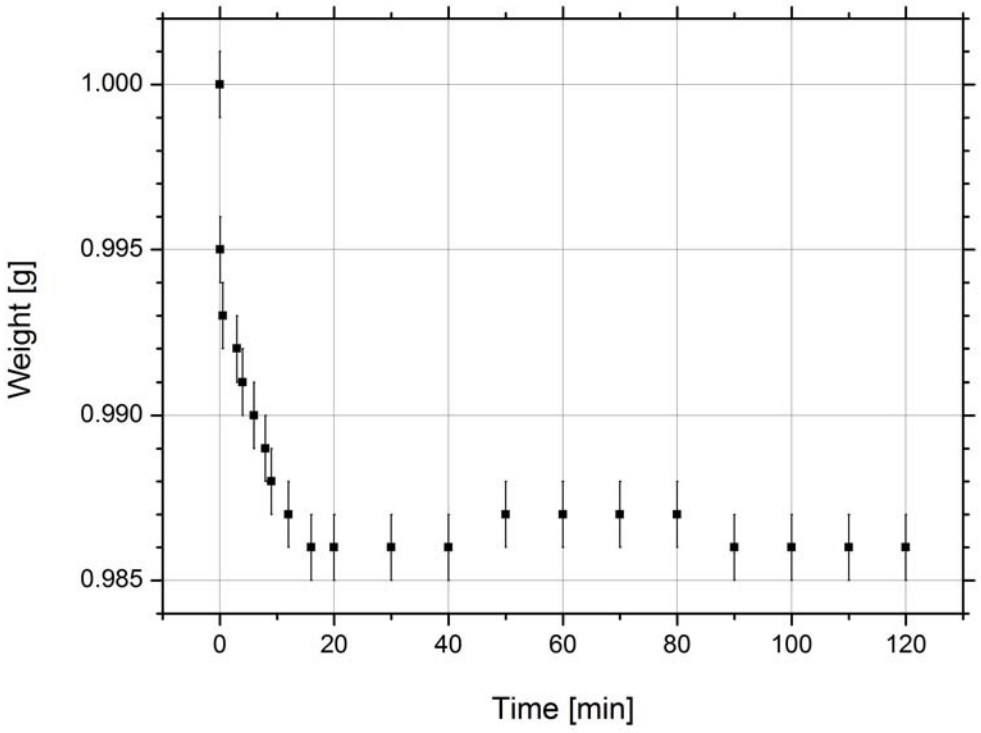

Figure 6.18: Weight of a perlite sample as a function of time for the determination of the moisture content.

Chapter 7

Heat Loss Measurements on a Real-Size Storage Prototype

In the framework of the research project at ZAE BAYERN about super-insulated long-term hot water storages, a real-size prototype tank was constructed by the project partner HUMMELSBERGER GMBH in Mühldorf in order to perform a variety of experiments under real conditions. During this thesis, heat loss measurements at the storage have been accomplished to determine the thermal conductivity of the vacuum super insulation in a real application.

7.1 Tank Layout and Measurement Setup

With respect to its schematic layout, the prototype is similar to the liquid gas storage tank described in section 5.2: The hot water is stored in the inner cylindrical container, which is fixed in the outer tank by a special suspension device (figure 5.2). Both containers are made of steel. The annular gap is filled with perlite (TECHNOPERL ® - C 1,5) and evacuated. In addition, the prototype tank is also equipped with several high-grade steel pipeline connections to load and discharge the water container. Furthermore, a stratification device, which was mentioned in chapter 1, is installed. Figure 7.1 shows a photograph and a sketch of the storage tank.

For the construction, large steel plates were bent to cylinders and subsequently covered with torispherical heads on their top and bottom. The different components were merged by welding. The heights of the tanks are $H_{tot,in} = 5.58\,\mathrm{m}$ and $H_{tot,out} = 5.98\,\mathrm{m}$, and the respective diameters are $D_{in} = 2\,\mathrm{m}$ and $D_{out} = 2.4\,\mathrm{m}$. Thus, the annular gap between inner and outer container, which is equal to the insulation thickness, has a constant value of $d_{gap} \approx 0.2\,\mathrm{m}$, also in the region of the torispherical heads. In fact, d_{gap} is slightly smaller, because the wall thickness of the containers has to be taken into account. All relevant dimensions of the prototype including the lengths of the supply pipelines are listed in table 7.1.

inner container (figure 7.1 b)		
outer diameter D_{in}	[m]	2
wall thickness $d_{wall,in}$	[mm]	8
inner diameter $d_{in} = D_{in} - 2d_{wall,in}$	[m]	1.984
height of the cylindrical part $H_{cyl,in}$	[m]	4.73
height of torispherical head $H_{TH,in}$	[m]	0.425
total height $H_{tot,in} = H_{cyl,in} + 2H_{TH,in}$	[m]	5.58
total volume (refers to outer diameter D_{in}) $V_{tot,in}$	[m³]	16.71
steel volume $V_{steel,in} = V_{tot,in} - V_{void,in}$	[m³]	0.32
void volume (refers to inner diameter d_{in}) $V_{void,in}$	[m³]	16.39
outer container (figure 7.1 a)		
outer diameter D_{out}	[m]	2.4
wall thickness $d_{wall,out}$	[mm]	8
inner diameter $d_{out} = D_{out} - 2d_{wall,out}$	[m]	2.384
height of the cylindrical part $H_{cyl,out}$	[m]	5
height of torispherical head $H_{TH,out}$	[m]	0.49
total height (without pedestals) $H_{tot,out} = H_{cyl,out} + 2H_{TH,out}$	[m]	5.98
total volume (refers to outer diameter D_{out}) $V_{tot,out}$	[m³]	25.49
steel volume $V_{steel,out} = V_{tot,out} - V_{void,out}$	[m³]	0.35
void volume (refers to inner diameter d_{out}) $V_{void,out}$	[m³]	25.14
suspension		
length l_{sus}	[m]	4
width d_{sus}	[m]	0.1
height H_{sus}	[mm]	10
supply pipelines (figure 7.1 b)		
outer diameter D_{SP}	[mm]	26.9
wall thickness $d_{wall,SP}$	[mm]	2
inner diameter $d_{SP} = D_{SP} - 2d_{wall,SP}$	[mm]	22.9
length 1 (return line from the solar thermal collector, red) $l_{SP,1}$	[m]	5.73
length 2 (feed line to the solar thermal collector, yellow) $l_{SP,2}$	[m]	1.26
length 3 (feed line for the heating system, green) $l_{SP,3}$	[m]	5.84
length 4 (return line from the heating system, blue) $l_{SP,4}$	[m]	1.2
length 5 (pipeline for temperature sensors, pink) $l_{SP,5}$	[m]	2.39
length 6 (air inlet and exhaust, brown) $l_{SP,6}$	[m]	6.67
general		
annular gap $d_{gap} = \frac{1}{2}(d_{out} - D_{in})$	[m]	0.192
insulation volume $V_{gap} = V_{void,out} - V_{tot,in}$	[m³]	8.43

Table 7.1: Dimensions of the storage tank prototype. For the supply pipelines, only the approximated lengths which are relevant for thermal losses are indicated [105, 106].

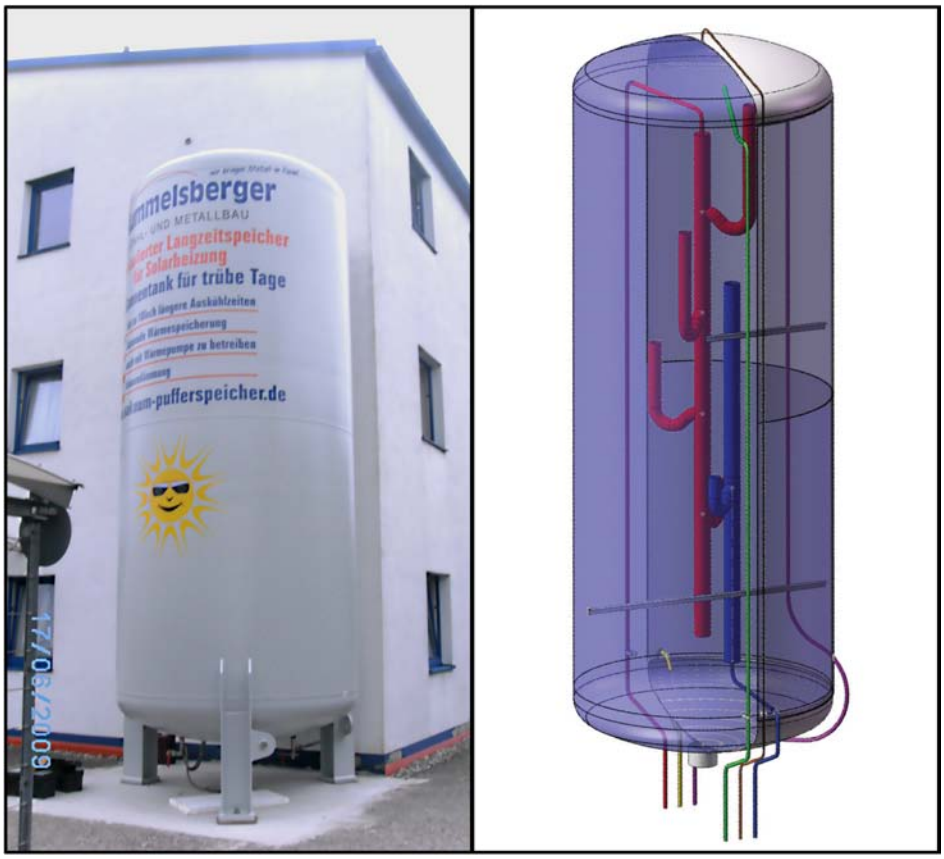

Figure 7.1: Layout of the real-size storage tank prototype: Photograph of the tank (a), sketch of the inner container with supply pipelines and stratification device (b).

Temperature Measurement

14 Pt-1000 sensors are installed at different positions in the inner and outer container. 6 sensors for measuring the water temperature (T_1 to T_6) are attached to the inner surface of a special supply pipeline, which is depicted pink in figure 7.1 b. The sensors are positioned equally-spaced over the whole height of the prototype (table 7.2). Another 6 sensors (T_9 to T_{14}) are located at the exterior surface of the outer container at the same heights, so that each of the inner sensors has its respective counterpart. Further sensors are mounted in the supply pipeline at a position near the bottom of the inner container within the perlite insulation (T_7) and on top of the outer container (T_8). However, these temperatures are not relevant for the determination of the thermal conductivity from the heat loss measurement.

sensors	T_1 and T_9	T_2 and T_{10}	T_3 and T_{11}	T_4 and T_{12}	T_5 and T_{13}	T_6 and T_{14}
height [m]	0.815	1.685	2.555	3.425	4.295	5.165

Table 7.2: positions of Pt-1000 temperature sensors, measured from the bottom of the outer container.

Because the electrical resistance of the Pt-1000 sensors is much larger than the resistance of the cables, temperatures are measured using the two-wire technique. The associated error is around $\Delta T = 1\,\mathrm{K}$. However, this error can be neglected for the determination of the thermal conductivity of the vacuum super insulation, because it is identical for all sensors (the lengths of the electrical supply cables are virtually equal) and only temperature differences are needed for the calculation (see section 7.2). An additional error for the temperature measurement arises from the fact that the pipeline, in which the sensors T_1 to T_7 are attached, is filled with air. As a consequence of convection inside the pipe, the temperature of the sensors T_1 to T_6 may differ from the real water temperature at the respective height. This error is also irrelevant though, because the water inside the tank was heated up to a homogeneous temperature of $T = 90\,°\mathrm{C}$ for the heat loss measurement. Convection inside the pipe can only occur if there is a sufficiently pronounced temperature difference along its height.

Pressure Measurement

Two vacuum flange connections are available, one at the bottom and one at the top torispherical head of the outer container. Initially, four pressure sensors were connected, both a capacitive sensor and a Pirani gauge [96] at both the upper and the lower position. From comparing the two capacitive sensors at a vacuum pressure of $p \approx 0.01\,\mathrm{mbar}$, it showed that there were no pressure differences between the top and the bottom region of the insulation. Therefore, the lower capacitive sensor was dismounted again. Because Pirani gauges are much less accurate, the capacitive sensor at the top of the prototype tank is used for the pressure measurement. As indicated in section 6.3, this type of sensor has a typical error of around 1 %.

Perlite Filling

During the process of filling the annular gap of the storage prototype with perlite, the compressibility of the material, which was already mentioned in the sections 4.3 and 5.5, became notable to a great extent: In total, $779\,\mathrm{kg}$ of TECHNOPERL ® - C 1,5 were filled into the annular gap with a total void volume of $V_{gap} = 8.43\,\mathrm{m^3}$ (table 7.1). The resulting bulk density is:

$$\rho = \frac{m}{V_{gap}} = 92.4\,\frac{\mathrm{kg}}{\mathrm{m^3}} \tag{7.1}$$

7.2 Presentation and Evaluation of Measurement Results

Heat Loss Measurement with Air at p = 0.08 mbar

The first important experiment, which was performed at the storage tank prototype, was the determination of the thermal conductivity λ_{eff} of the vacuum super insulation. The concept of the experiment was to measure the rate of temperature decrease dT_{water}/dt of the stored water and the ambient temperature T_a. If the total integral heat capacity C_{tot}

of the inner container and the shape factor S_{tot} of the overall tank geometry are known, λ_{eff} can be calculated according to:

$$C_{tot}\frac{dT_{water}}{dt} = \dot{Q} = \lambda_{eff} S_{tot} \left(T_{water} - T_a\right) \tag{7.2}$$

Theoretically, this method is only correct if T_{water} and dT_{water}/dt are determined at a single point in time, because T_{water} decreases exponentially (equation 1.1). In practice however, the derivative can be replaced by $\Delta T_{water}/\Delta t$, where Δt is an extended time interval with a constant temperature decrease (linear approximation). The calculation procedure is described in detail below, because equation 7.2 includes some simplifications and is only suitable to illustrate the measurement principle.

The temperature decrease was measured over a period of 240 hours starting on December 10, 2010 at 12:00 a.m. (midnight). A few days prior to the measurement, the water inside the storage tank was heated up to $T = 90\,°\text{C}$ using a specially designed heating station, which was connected to the supply pipelines for the solar collector. At the end of this process, a homogeneous temperature of $T_1 = T_2 = ... = T_6 = 90\,°\text{C}$ was reached. For the evaluation of the heat loss measurement, the average temperature of the sensors T_1 to T_6 was calculated and is shown in figure 7.2 as a function of time. During the measurement interval, the mean vacuum pressure in the insulation was $\bar{p} = 0.0833\,\text{mbar}$. The rate of temperature decrease is obtained from the linear fit (red line):

$$\frac{\Delta T_{water}}{\Delta t} = 2.69 \cdot 10^{-6}\,\frac{\text{K}}{\text{s}} \tag{7.3}$$

The statistical error of the fit is more than three orders of magnitude smaller and therefore neglected.

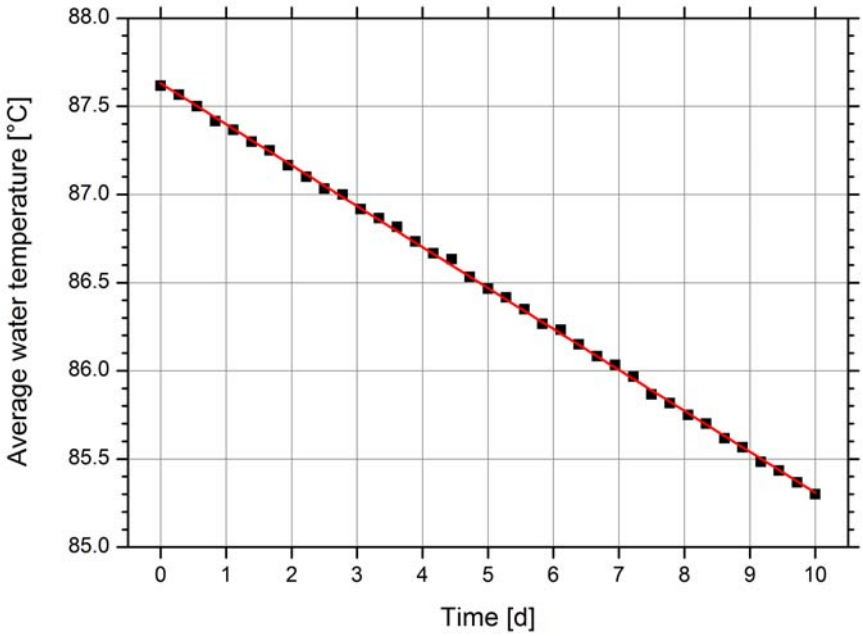

Figure 7.2: Decrease of the average water temperature for the heat loss measurement.

In the next step, the total integral heat capacity C_{tot} is determined. For its calculation, three contributions have to be taken into account:

- The largest fraction of C_{tot} is the heat capacity $C_{water} = c_{water} m_{water}$ of the stored water. During the filling process of the inner container, a water mass of $m_{water} = 15,537\,\text{kg}$ was measured. With the specific heat capacity $c_{water} = 4,187\,\text{J/kgK}$ [72], one arrives at $C_{water} = 65.05 \cdot 10^6\,\text{J/K}$. However, this quantity contains an error: At $T = 90\,°\text{C}$, the density of water is given by $\rho_{water} = 965.3\,\text{kg/m}^3$ [107]. Therefore, the measured value for m_{water} corresponds to a volume of $V_{water} = 16.1\,\text{m}^3$, which is less than the void volume of the inner tank $V_{void,in} = 16.4\,\text{m}^3$ (table 7.1). This means, that either the container has not been completely filled with water, or the measurement of the water mass has been inaccurate. The systematic error is assumed to be equal to the difference of $V_{void,in} - V_{water} = 0.3\,\text{m}^3$. Converted into heat capacity, one arrives at $\Delta C_{water} = 1.21 \cdot 10^6\,\text{J/K}$.
- The temperature of the steel container is practically identical to the water temperature, which causes another considerable contribution of C_{tot}. From $C_{steel} = c_{steel} \rho_{steel} V_{steel,in}$ and the values $c_{steel} = 477\,\text{J/kgK}$ [108], $\rho_{steel} = 8,000\,\text{kg/m}^3$ [108] and $V_{steel,in} = 0.32\,\text{m}^3$ (table 7.1), one obtains $C_{steel} = 1.22 \cdot 10^6\,\text{J/K}$.
- Finally, also the heat capacity of the perlite inside the annular gap has to be considered. However, this contribution has to be weighted by a factor of $1/2$, because the average temperature $\bar{T}_{perlite} = (T_{water} + T_a)/2$ only decreases by $0.5\,\text{K}$ if the water temperature T_{water} drops by $1\,\text{K}$ and the ambient temperature T_a stays constant. With $c_{perlite} = 900\,\text{J/kgK}$ [109], $\rho_{perlite} = 92.4\,\text{kg/m}^3$ (equation 7.1) and $V_{gap} = 8.43\,\text{m}^3$ (table 7.1), the contribution of perlite is equal to $C_{perlite} = c_{perlite} \rho_{perlite} V_{gap}/2 = 0.35 \cdot 10^6\,\text{J/K}$. On a sidenote, the linear approximation $\bar{T}_{perlite} = (T_{water} + T_a)/2$ is valid, because the gap size d_{gap} (table 7.1) is much smaller than the diameter D_{in} of the inner tank and therefore the geometry can be approximated by parallel plates (see section 2.1).

Summing up the three fractions, one arrives at:

$$C_{tot} = C_{water} + C_{steel} + C_{perlite} = (66.6 \pm 1.2) \cdot 10^6\,\frac{\text{J}}{\text{K}} \tag{7.4}$$

With this result, the heat loss of the stored water can be calculated according to:

$$\dot{Q}_{tot} = C_{tot} \frac{\Delta T_{water}}{\Delta t} = (179.1 \pm 3.2)\ \text{W} \tag{7.5}$$

For the further evaluation, it has to be taken into account that the total rate of heat loss $\dot{Q}_{tot}$ is not equal to the heat flux $\dot{Q}_{perlite}$ through the evacuated perlite insulation, because it also includes thermal losses $\dot{Q}_{loss}$ via the supply pipelines and the suspension device. In a separate investigation [105], the thermal losses were calculated from the

relevant dimensions (table 7.1) using numerical methods. The result of this examination is $\dot{Q}_{loss} = 2.4\,\mathrm{W}$. It is in good agreement with the following approximation:

$$\begin{aligned}\dot{Q}_{loss,approx} &= \dot{Q}_{suspension} + \dot{Q}_{pipelines} \\ &= 2\lambda_{steel}\frac{d_{sus}H_{sus}}{l_{sus}}\Delta T + \sum_{i=1}^{6}\lambda_{HGS}\frac{\left(D_{SP}^2 - d_{SP}^2\right)\pi}{4l_{SP,i}}\Delta T \\ &= 2.3\,\mathrm{W} + 0.5\,\mathrm{W} = 2.8\,\mathrm{W} \end{aligned} \tag{7.6}$$

For this calculation, the values $\lambda_{steel} = 50\,\mathrm{W/mK}$ [110], $\lambda_{HGS} = 15\,\mathrm{W/mK}$ [102] and $\Delta T = 90\,\mathrm{K}$ were used.

As a consequence of the determination of $\dot{Q}_{loss}$, the heat flux through the insulation is given by:

$$\dot{Q}_{perlite} = \dot{Q}_{tot} - \dot{Q}_{loss} = (176.7 \pm 3.2)\ \mathrm{W} \tag{7.7}$$

Now, equation 7.2 suggests to determine the total shape factor of the storage prototype and to calculate λ_{eff} from the measured temperature difference $\Delta T = T_{water} - T_a$. However, ΔT is not constant everywhere. During the heat loss measurement, the water in the top region of the inner container was around $3\,\mathrm{K}$ hotter than the water at the bottom. Therefore, the heat flux $\dot{Q}_{perlite}$ is divided into three parts, which is more precise:

$$\begin{aligned}\dot{Q}_{perlite} &= \dot{Q}_{top} + \dot{Q}_{cyl} + \dot{Q}_{bottom} \\ &= \lambda_{eff}\left(S_{TH}\Delta T_{top} + \frac{2\pi H_{cyl,in}}{\ln\left(d_{out}/D_{in}\right)}\Delta T_{cyl} + S_{TH}\Delta T_{bottom}\right) \end{aligned} \tag{7.8}$$

The major fraction of $\dot{Q}_{perlite}$ flows through the cylindrical part of the storage tank. It is denoted with $\dot{Q}_{cyl}$ and can be calculated according to equation 2.4. The relevant dimensions $H_{cyl,in}$, d_{out} and D_{in} can be read off from table 7.1. At the top and bottom boundaries, the heat transfer rates $\dot{Q}_{top}$ and $\dot{Q}_{bottom}$ through the arrangement of the torispherical heads have to be calculated. For an exact evaluation, equation 2.6 has to be used, which requires the determination of the shape factor S_{TH}. Thus, the four parameters ΔT_{top}, ΔT_{cyl}, ΔT_{bottom} and S_{TH} still have to be quantified in order to obtain the effective thermal conductivity of the insulation.

The temperature differences can be determined relatively easy from the measured temperatures T_1 to T_6 and T_9 to T_{14}. First, the values are averaged over the total measurement interval of 10 days to obtain the mean temperatures $\bar{T}_1$ to $\bar{T}_6$ and $\bar{T}_9$ to $\bar{T}_{14}$. The quantity ΔT_{top} is then calculated from $\bar{T}_1$ and $\bar{T}_9$, which are the relevant temperatures at the top region of the storage prototype:

$$\Delta T_{top} = \bar{T}_1 - \bar{T}_9 = 89.7\,\mathrm{K} \tag{7.9}$$

In analogy, $\bar{T}_6$ and $\bar{T}_{14}$ are used for the bottom region:

$$\Delta T_{bottom} = \bar{T}_6 - \bar{T}_{14} = 86.2\,\mathrm{K} \tag{7.10}$$

For the cylindrical part, the values from the remaining sensors are averaged:

$$\Delta T_{cyl} = \frac{1}{4}\left(\bar{T}_2 + \bar{T}_3 + \bar{T}_4 + \bar{T}_5 - \bar{T}_{10} - \bar{T}_{11} - \bar{T}_{12} - \bar{T}_{13}\right) = 89.2\,\mathrm{K} \tag{7.11}$$

The calculation of the shape factor S_{TH} is more difficult. Initially, the geometry of the torispherical heads, which consists of several radii and heights (figure 7.3) is approximated by spherical caps with a single radius. The arrangement of the two torispherical heads from the inner and the outer container according to the approximation is shown in figure 7.4. The dimensions r_1, r_2, d and h from figure 7.4 are defined according to the geometry of the storage prototype (table 7.1):

$$r_1 = 1\,\mathrm{m} \qquad r_2 = 1.2\,\mathrm{m} \qquad d = 0.2\,\mathrm{m} \qquad h = 0.4\,\mathrm{m} \tag{7.12}$$

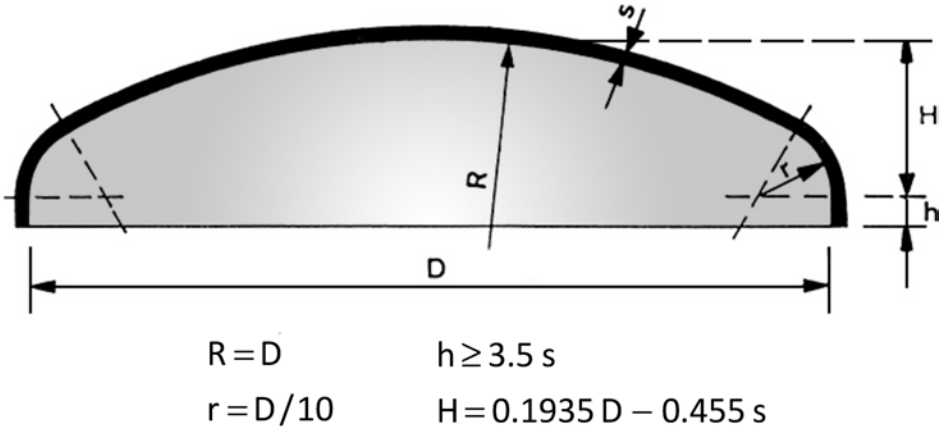

Figure 7.3: Dimensioning of torispherical heads according to DIN 28011 [111, 112].

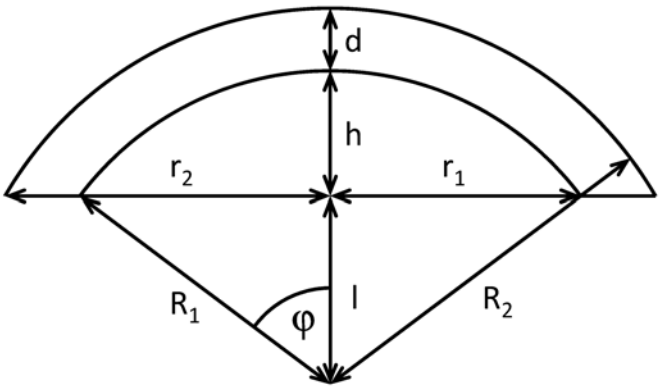

Figure 7.4: Approximation of the shape factor S_{TH}.

Subsequently, the missing geometrical quantities are calculated:

$$\begin{aligned} R_1^2 &= l^2 + r_1^2 = (R_1 - h)^2 + r_1^2 \;\Rightarrow\; R_1 = \frac{h^2 + r_1^2}{2h} = 1.45\,\mathrm{m} \\ R_2 &= R_1 + d = 1.65\,\mathrm{m} \\ l &= R_1 - h = 1.05\,\mathrm{m} \\ \sin\varphi &= \frac{r_1}{R_1} \;\Rightarrow\; \varphi = 43.6° \end{aligned} \tag{7.13}$$

Now, there are three possibilities to calculate S from the approximated geometry:

- The area A of a spherical cap is given by [113]:

$$A = 2\pi R^2 \left(1 - \cos\varphi\right) \tag{7.14}$$

  Therefore, the approximation for parallel plates (equation 2.3) can be applied, using the area A_1 of the inner spherical cap as reference area:

$$S_{approx,1} = \frac{A_1}{d} = \frac{2\pi R_1^2 \left(1 - \cos\varphi\right)}{d} = 18.2\,\mathrm{m} \tag{7.15}$$

- In analogy, it is also possible to refer to the area A_2 of the outer spherical cap:

$$S_{approx,2} = \frac{A_2}{d} = \frac{2\pi R_2^2 \left(1 - \cos\varphi\right)}{d} = 23.6\,\mathrm{m} \tag{7.16}$$

- Eventually, one can also use equation 2.5, which is valid for spherical geometries. Applying this method, the factor $\left(1 - \cos\varphi\right)/2$ has to be included, because the approximated shape factor $S_{approx,3}$ must not refer to the whole surface of the sphere, but only to the fraction of the spherical cap:

$$S_{approx,3} = \frac{4\pi \left(1 - \cos\varphi\right)}{2\left(\frac{1}{R_1} - \frac{1}{R_2}\right)} = 20.7\,\mathrm{m} \tag{7.17}$$

Because the deviations between the three different approximated shape factors are in the range of up to 30 %, a numerical simulation has been done in order to obtain a reliable result for S_{TH}. For this purpose, the exact geometry of the storage prototype including the dimensioning of the torispherical heads (figure 7.3) has been modelled in SOLIDWORKS 2008, and the add-on COSMOSFLOWORKS 2008 has been used to calculate the heat flux through the arrangement of the inner and outer torispherical head at a given thermal conductivity of the insulation and temperature difference [105]. The numerical investigation yields:

$$S_{TH,CFD} = 23.6\,\mathrm{m} \tag{7.18}$$

It is a remarkable coincidence, that this result is identical to $S_{approx,2}$, which has been calculated from an approximation by parallel plates.

Finally, all relevant parameters are known, and the effective thermal conductivity of the evacuated perlite insulation ($p = 0.08\,\text{mbar}$) can be calculated by inserting the results from equations 7.7, 7.9 to 7.11 and 7.18 into equation 7.8:

$$\begin{aligned} \lambda_{eff} &= \frac{\dot{Q}_{perlite}}{\left(S_{TH}\Delta T_{top} + \frac{2\pi H_{cyl,in}}{\ln(d_{out}/D_{in})}\Delta T_{cyl} + S_{TH}\Delta T_{bottom}\right)} \\ &= (9.18 \pm 0.17) \cdot 10^{-3}\,\frac{\text{W}}{\text{mK}} \end{aligned} \tag{7.19}$$

This value is surprisingly low, because one would expect a solid thermal conductivity of $\lambda_s = (14.7 \pm 1.6)$ W/mK from the measurements in the parallel plate setup (equation 6.15), which is already significantly higher than the total effective thermal conductivity of the perlite insulation in the storage prototype. This result is interpreted as another argument confirming the assumption on page 67, which states that the thermal resistances due to the solid structure were shorted by the high external pressure during the experiments in the parallel plate apparatus. This supposition was already supported by the estimation of the solid thermal conductivity from the measurements in the cut-off cylinder device (section 6.3.2). Obviously, there are two different possibilities to create high bulk densities for perlite:

The material can be compressed by applying external pressure. As mentioned above, the solid structure is damaged in this case, which leads to the shorting of thermal resistances. Under these conditions, equation 6.15 can be used to calculate the solid thermal conductivity.

Another possibility is to compress the material by pouring and vibrations, which causes the single perlite grains to arrange in a space-saving way (close-packing of spheres). Because the solid structure stays intact, the value of λ_s must be lower in this case. The density dependency of the solid thermal conductivity is still assumed to be linear for this situation. In order to determine $\lambda_s\,(\rho)$, at least three data points are necessary. Fortunately, one experimental value is available from each of the measurements in Würzburg, Garching and Mühldorf:

- In the parallel plate device, the material was still uncompressed during the measurement at the lowest density ($\rho = 55.2\,\text{kg}/m^3$). The corresponding solid thermal conductivity was $\lambda_s = (2.46 \pm 1.23) \cdot 10^{-3}$ W/mK at the mean temperature $\bar{T} = 361\,\text{K}$ (average values of all four measurements in figure 6.6).
- From the measurements in the cut-off cylinder apparatus at $\rho = 68.2\,\text{kg}/m^3$ and $T = 337\,\text{K}$, a solid thermal conductivity of $\lambda_s = (3.39 \pm 1.27) \cdot 10^{-3}$ W/mK was estimated (section 6.2.2).
- Finally, the value of λ_s at $\rho = 92.4\,\text{kg}/m^3$ can be calculated from the heat loss measurement on the storage prototype. As derived above, the effective thermal conductivity of the insulation is $\lambda_{eff} = (9.18 \pm 0.17) \cdot 10^{-3}$ W/mK (equation 7.19) at a pressure of $p = 0.08\,\text{mbar}$. As a first step, the radiative thermal conductivity

$\lambda_r = (2.55 \pm 0.25) \cdot 10^{-3}$ W/mK is computed according to equation 6.10, where the radiation temperature T_r is calculated from the average values of the temperatures $\bar{T}_1$ to $\bar{T}_6$ and $\bar{T}_9$ to $\bar{T}_{14}$. Subsequently, the contribution of gaseous conduction and coupling is determined from equation 6.14. For the parameters $p^g_{1/2}$, $p^c_{1/2}$ and Φ, the values from table 6.4 are inserted, because the measurement in the cut-off cylinder apparatus better represents the unmodified material with the original pore size. The result is $\lambda_g + \lambda_c = (1.53 \pm 0.08) \cdot 10^{-3}$ W/mK. For this calculation, the continuum thermal conductivity $\lambda_0 = 27.3 \cdot 10^{-3}$ W/mK is used [34]. This is the correct value at the average temperature of the perlite insulation $T = 315$ K, which is the arithmetic mean of the temperatures $\bar{T}_1$ to $\bar{T}_6$ and $\bar{T}_9$ to $\bar{T}_{14}$. Subtracting λ_r and $\lambda_g + \lambda_c$ from λ_{eff}, one arrives at $\lambda_s = (5.1 \pm 0.5) \cdot 10^{-3}$ W/mK. This value really represents the solid thermal conductivity of TECHNOPERL ® - C 1,5 without external pressure, because the pressure acting on the perlite layer at the bottom of the tank due to the weight of the higher layers is only $p_{ext} = \rho_{perlit}\, V_{gap}\, g / A_{ring} = 58$ mbar, which is much less than the pressure load of $p_{ext} = 1.05$ bar during the measurement in the parallel plate apparatus. For this calculation, the area $A_{ring} = \left(d^2_{out} - D^2_{in}\right) \pi/4$ has been used.

In figure 7.5, these values of λ_s without external pressure are shown as a function of density. Although the errors are relatively large, the linear correlation is clearly visible. The temperature dependency of λ_s is neglected, because it showed during the measurements in the parallel plate apparatus, that this effect is relatively small. Furthermore, the individual data points in figure 7.5 were measured at similar temperatures.

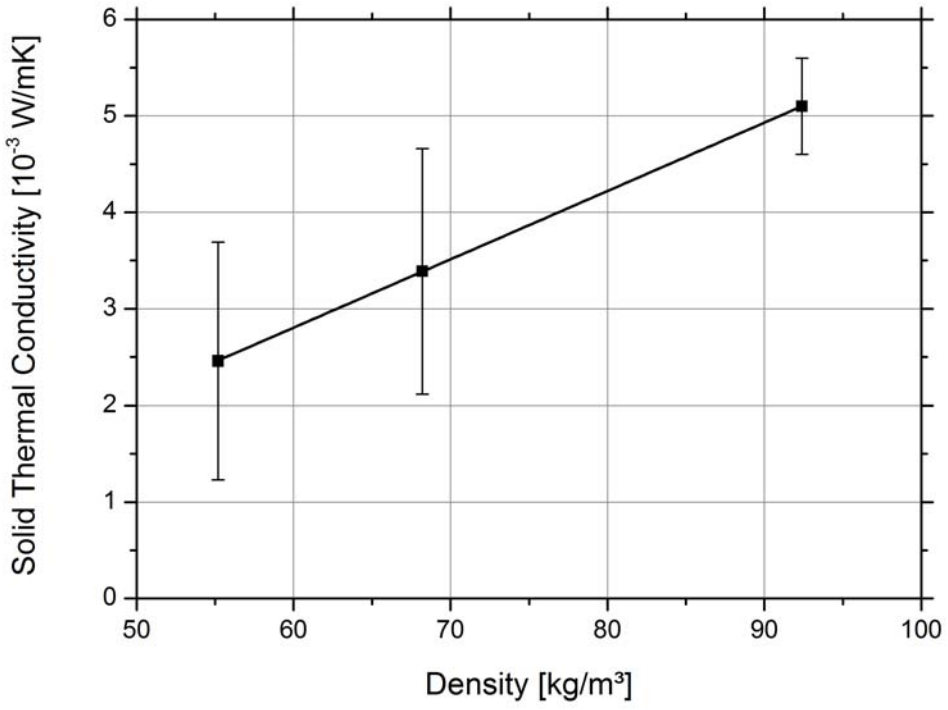

Figure 7.5: Solid heat conductivity as a function of density without external pressure.

From the linear fit in figure 7.5, one obtains:

$$\lambda_s = \left((0.0709 \pm 0.0002) \cdot \rho \left[\frac{kg}{m^3} \right] - (1.4499 \pm 0.0135) \right) \cdot 10^{-3} \, \frac{\mathrm{W}}{\mathrm{mK}} \tag{7.20}$$

Since equation 7.20 represents an intact solid structure, it is much more suitable than equation 6.15 for the calculation of λ_s under practical conditions.

Heat Loss Measurement with Krypton at p = 7.6 mbar

In a further experiment, the annular gap between both containers was completely evacuated and subsequently filled with krypton. Just like before, the water inside the storage was heated up to a homogeneous temperature ($T = 95\,°\mathrm{C}$), and the heat loss $\Delta T_{water}/\Delta t$ was measured for a total duration of 7 days, starting on May 24, 2010 at 12:00 a.m. (midnight). During this period, the average pressure within the perlite insulation was $\bar{p} = 7.598\,\mathrm{mbar}$. The other measured quantities, which are relevant for the determination of the effective thermal conductivity, are:

$$\Delta T_{water}/\Delta t \;=\; 5.48 \cdot 10^{-6} \, \frac{\mathrm{K}}{\mathrm{s}}$$

$$\Delta T_{top} = 73.5\,\mathrm{K} \qquad \Delta T_{bottom} = 69.0\,\mathrm{K} \qquad \Delta T_{cyl} = 72.8\,\mathrm{K} \tag{7.21}$$

According to equation 7.5, this corresponds to a total heat loss of $\dot{Q}_{tot} = (365.3 \pm 6.6)\ \mathrm{W}$. The thermal losses $\dot{Q}_{loss} = 1.9\,\mathrm{W}$ due to the supply pipelines and the suspension device are smaller, because the temperature differences were lower compared to the measurement with air as a consequence of the higher ambient temperature in May. Therefore, the rate of heat transfer through the perlite insulation is given by $\dot{Q}_{perlite} = (363.4 \pm 6.6)\ \mathrm{W}$ (equation 7.7). By inserting this result into equation 7.19, the effective thermal conductivity of the perlite insulation under the effect of krypton at $p = 7.6\,\mathrm{mbar}$ can be calculated:

$$\lambda_{eff} = (23.1 \pm 0.4) \cdot 10^{-3} \, \frac{\mathrm{W}}{\mathrm{mK}} \tag{7.22}$$

With $\lambda_r = (3.0 \pm 0.3) \cdot 10^{-3}\,\mathrm{W/mK}$, which has been computed according to equation 6.10 with the measured temperatures $\bar{T}_1$ to $\bar{T}_6$ and $\bar{T}_9$ to $\bar{T}_{14}$, and $\lambda_s = (5.1 \pm 0.5) \cdot 10^{-3}\,\mathrm{W/mK}$ (see figure 7.5), this value is equivalent to:

$$\lambda_g + \lambda_c = (15.0 \pm 1.2) \cdot 10^{-3} \, \frac{\mathrm{W}}{\mathrm{mK}} \tag{7.23}$$

This result is in perfect agreement with the krypton measurements in the cut-off cylinder apparatus: With the mean perlite temperature $\bar{T} = 55.5\,°\mathrm{C}$ during the heat loss measurement in the storage prototype, the continuum thermal conductivity of krypton is given by $\lambda_0 = 10.3 \cdot 10^{-3}\,\mathrm{W/mK}$ [34]. From a calculation of $\lambda_g + \lambda_c$ according to equation 6.30 with this value for λ_0 and the parameters $p^g_{1/2}$, $p^c_{1/2}$ and Φ from table 6.6, one obtains $\lambda_g + \lambda_c = (14.9 \pm 2.3) \cdot 10^{-3}\,\mathrm{W/mK}$.

Measurement of the Leakage Rate

Another important experiment for the practical application of vacuum super insulation is the determination of the leakage rate χ of the storage prototype. If the vacuum pressure increases over time, the insulation deteriorates due to an increment of λ_g and λ_c. For the measurement of χ, the pressure inside the annular gap was recorded over a total duration of 83 days, from December 15, 2010 to March 8, 2011. The experimental data is shown in figure 7.6. Because pressure is correlated to temperature according to the ideal gas law ($pV/T = Nk_B$), the values have been normalized:

$$\hat{p}\,(t) = \frac{\bar{T}}{T\,(t)} p\,(t) \tag{7.24}$$

The mean temperature $\bar{T}$ has been determined from averaging over the whole measurement interval and over all temperatures $\bar{T}_1$ to $\bar{T}_6$ and $\bar{T}_9$ to $\bar{T}_{14}$. From the linear fit (red line in figure 7.6), one obtains the pressure increase $\dot{p}$:

$$\dot{p} = 2.70 \cdot 10^{-9}\,\frac{\text{mbar}}{\text{s}} = 2.33 \cdot 10^{-4}\,\frac{\text{mbar}}{\text{d}} = 0.085\,\frac{\text{mbar}}{\text{a}} \tag{7.25}$$

With the insulation volume $V_{gap} = 8.43\,\text{m}^3$, the leakage rate can be calculated:

$$\chi = \dot{p} V_{gap} = 2.28 \cdot 10^{-5}\,\frac{\text{mbar}\,\text{l}}{\text{s}} \tag{7.26}$$

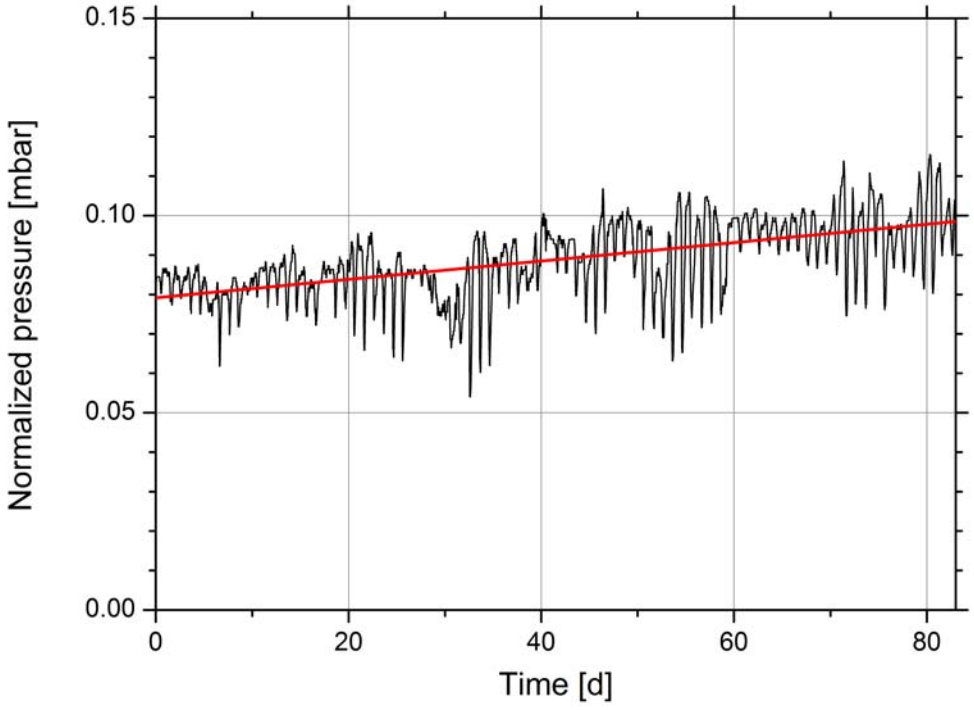

Figure 7.6: Determination of the leakage rate of the storage prototype.

Chapter 8

Summary of the Experimental Results and Conclusions

As a result of the experiments which were described in the two previous chapters, the effective thermal conductivity λ_{eff} of TECHNOPERL ® - C 1,5 can be calculated at a given pressure, temperature and density. This knowledge is important for the practical application of vacuum super insulation in hot water storages. Furthermore, approaches to minimize λ_{eff} can be formulated.

8.1 Calculation of the Effective Thermal Conductivity for Practical Purposes

According to section 4.5, there are four mechanisms that contribute to the effective thermal conductivity: radiative heat transport, solid conduction, gas conduction and the coupling effect:

$$\lambda_{eff} = \lambda_r + \lambda_s + \lambda_g + \lambda_c \tag{8.1}$$

For the radiative thermal conductivity $\lambda_r\,(T, \rho)$ as a function of temperature and density, the following relation can be used (sections 4.3 and 6.1):

$$\lambda_r\,(T, \rho) = \frac{16\sigma T_r^3}{3\rho e^*(T_r)} \tag{8.2}$$

In equation 8.2, $\sigma = 5.6704 \cdot 10^{-8}$ W/m^{2}K^4 is the Stefan-Boltzmann constant. Furthermore, the radiation temperature T_r occurs (see section 4.3), which is defined as:

$$T_r = \sqrt[3]{\frac{1}{4}\left(T_1^2 + T_2^2\right)\left(T_1 + T_2\right)} \tag{8.3}$$

T_1 and T_2 are the temperatures of the insulation boundaries. In the case of a cylindrical storage tank, T_1 can by approximated by the water temperature in the inner

container, and T_2 is practically identical with the ambient temperature. The extinction $e^*(T_r)$ has been determined experimentally (section 6.1). In the temperature interval between $300\,\mathrm{K} \leq T_r \leq 450\,\mathrm{K}$, it can be calculated from a quadratic approximation according to:

$$e^*(T_r) = \left(5.32 \cdot 10^{-4} \cdot T_r[\mathrm{K}]^2 - 0.4503 \cdot T_r[\mathrm{K}] + 130.31\right) \frac{\mathrm{m^2}}{\mathrm{kg}} \pm 4 \frac{\mathrm{m^2}}{\mathrm{kg}} \tag{8.4}$$

For the solid thermal conductivity $\lambda_s(T, \rho)$, a linear dependency on density has been observed:

$$\lambda_s(\rho) = \left((0.0709 \pm 0.0002) \cdot \rho \left[\frac{kg}{m^3}\right] - (1.4499 \pm 0.0135) \right) \cdot 10^{-3} \frac{\mathrm{W}}{\mathrm{mK}} \tag{8.5}$$

Equation 8.5 is only valid if the material is compressed by its own weight or by vibrations, which cause the single perlite grains to arrange in a close packing of spheres (see section 7.2). If the compression is achieved by external pressure, the solid structure is damaged and thermal resistances are shorted. In this case, equation 6.15 has to be used. The temperature dependency of λ_s, which has been expected according to section 4.2, has not been observed in the experiments. It is assumed that this effect is negligibly small.

The gaseous thermal conductivity $\lambda_g(T, p)$ at a given vacuum pressure and temperature can be calculated using the Sherman interpolation (section 4.1):

$$\lambda_g(T, p) = \frac{\lambda_0(T)}{1 + \frac{p^g_{1/2}}{p}} \tag{8.6}$$

The characteristic half-value pressure $p^g_{1/2}$ has been determined experimentally for air, argon and krypton and is shown in table 8.1. In addition, the temperature-dependent continuum thermal conductivity $\lambda_0(T)$ appears in equation 8.6. $\lambda_0(T)$ is depicted in figure 8.1 for a selection of gases and can be approximated using a second-order polynomial:

$$\lambda_0 = \left(A + B\,T[\mathrm{°C}] + C\,T[\mathrm{°C}]^2\right) \cdot 10^{-3} \frac{\mathrm{W}}{\mathrm{mK}} \tag{8.7}$$

The constants A, B and C are listed in table 8.2.

Regarding the coupling thermal conductivity $\lambda_c(T, p)$, the experiments in chapter 6 have shown that the measured data can successfully be represented by the simplified coupling model, which was developed in section 4.4:

$$\lambda_c(T, p) = \Phi \frac{\lambda_0(T)}{1 + \frac{p^c_{1/2}}{p}} \tag{8.8}$$

Again, the continuum thermal conductivity can be computed according to equation 8.7. The parameters Φ and $p^c_{1/2}$ are included in table 8.1 for air, argon and krypton.

gas	$p^g_{1/2}$ [mbar]	Φ [1]	$p^c_{1/2}$ [mbar]
air	1.38±0.07	0.54±0.03	38.6±8.1
argon	1.46±0.01	0.73±0.01	17.4±0.4
krypton	1.24±0.47	0.93±0.06	4.5±2.6

Table 8.1: Parameters for the calculation of λ_g and λ_c according to equations 8.6 and 8.8.

gas	A [1]	B [1]	C [1]
air	24.17±0.02	0.075±0.001	(-2.88±0.14)$\cdot 10^{-5}$
argon	16.39±0.10	0.049±0.001	(-2.72±0.56)$\cdot 10^{-5}$
krypton	8.76±0.02	0.029±0.001	(-1.30±0.10)$\cdot 10^{-5}$

Table 8.2: Parameters for the calculation of λ_0 according to equation 8.7.

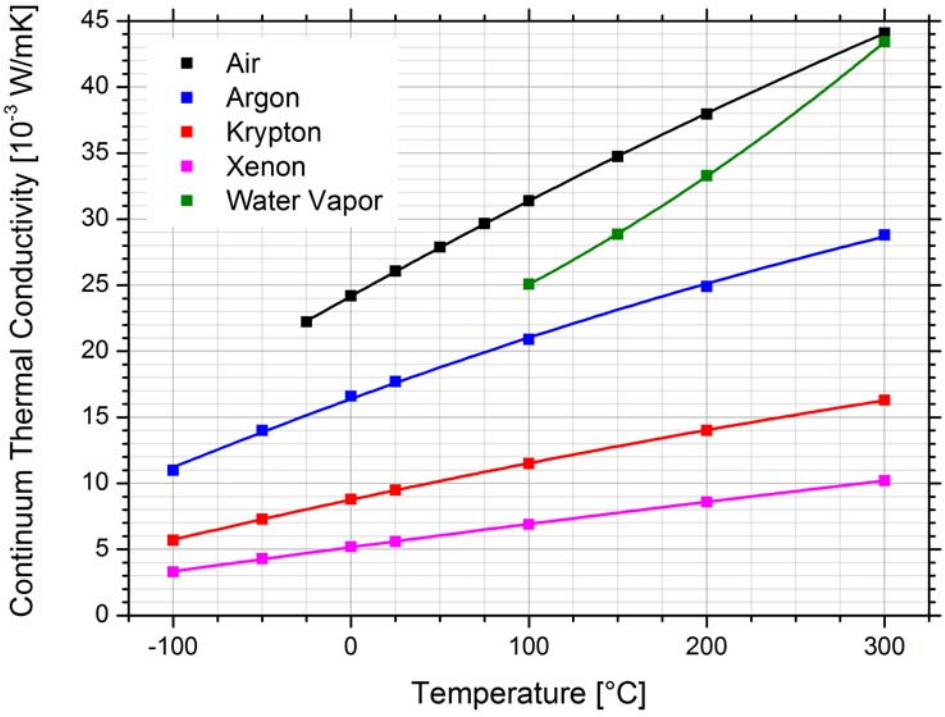

Figure 8.1: Continuum thermal conductivity λ_0 of selected gases as a function of temperature [34].

8.2 Suggestion of Optimization Approaches

In the experimental part of this thesis (chapters 6 and 7), the dependencies of the effective thermal conductivity on pressure, density, temperature and the type of filling gas have been measured. As a consequence, different optimization approaches can be suggested with the aim to minimize λ_{eff} under practical conditions.

Minimization of λ_s and λ_r

Both the solid and the radiative thermal conductivity of TECHNOPERL ® - C 1,5 depend on density. λ_s increases linearly with ρ (equation 8.5), whereas λ_r decreases according to $\lambda_r \sim \rho^{-1}$ (equation 8.2). Therefore, an optimum density ρ_{opt} exists, at which the sum $\lambda_r + \lambda_s$ attains a minimum value. Because λ_r also depends on the radiation temperature, ρ_{opt} is a function of T_r, which is usually predetermined by the application. The temperature dependency of λ_s is neglected (see section 6.2.2). In figure 8.2, the sum of $\lambda_r + \lambda_s$ is plotted against ρ at different radiation temperatures. The blue curve with $T_r = 325\,\mathrm{K}$ refers to the storage of hot water for solar thermal applications ($T_1 = 100\,°\mathrm{C}$, $T_2 = 0\,°\mathrm{C}$).

The optimum density can be calculated using the conventional method for the determination of extremal values:

$$\begin{aligned} \frac{d\left(\lambda_r + \lambda_s\right)}{d\rho} &= -\frac{16\sigma T_r^3}{3\rho^2 e^*\left(T_r\right)} + A_s \stackrel{!}{=} 0 \\ \Rightarrow \quad \rho_{opt} &= \sqrt{\frac{16\sigma T_r^3}{3A_s e^*\left(T_r\right)}} \end{aligned} \tag{8.9}$$

In equation 8.9, $A_s = 0.0709 \cdot 10^{-3}\,\mathrm{W\ m^2/K\ kg}$ is the first coefficient for the linear density dependency of λ_s (see equation 8.5). The optimum density as a function of the radiation temperature T_r is depicted in figure 8.3.

With respect to the solar thermal application ($T_r = 325\,\mathrm{K}$), it shows that the optimum density is at $\rho_{opt} = 60.4\,\mathrm{kg/m^3}$. It is questionable whether this value can be reached in practice, because the self-adapted bulk density in the storage prototype is considerably higher ($\rho = 92.4\,\mathrm{kg}/m^3$). However, it has to be said that the influence of ρ is not very pronounced at $T_r = 325\,\mathrm{K}$, which can be demonstrated by figure 8.2 (blue curve): In the whole interval from $50\,\mathrm{kg/m^3} \leq \rho \leq 95\,\mathrm{kg/m^3}$, the sum of radiative and solid thermal conductivity only changes by $1 \cdot 10^{-3}\,\mathrm{W/mK}$. For the application of vacuum super insulation in this temperature range, the bulk density of $\rho = 92.4\,\mathrm{kg}/m^3$ is still acceptable, because $\lambda_r + \lambda_s$ is only slightly above the minimum value.

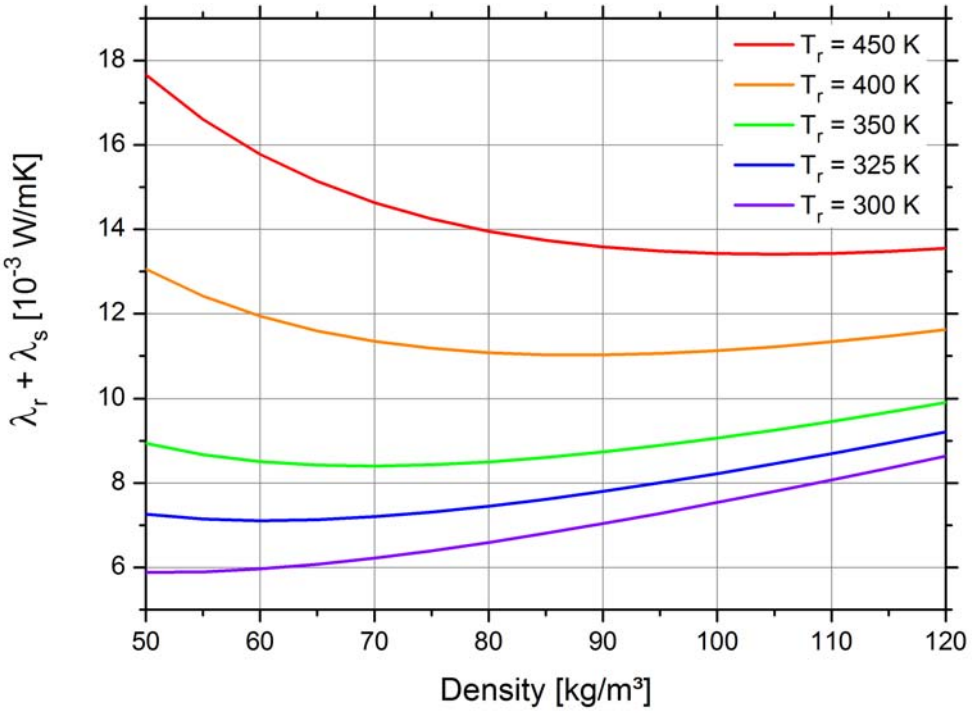

Figure 8.2: Sum of radiative and solid thermal conductivity as a function of density according to equations 8.2 and 8.5.

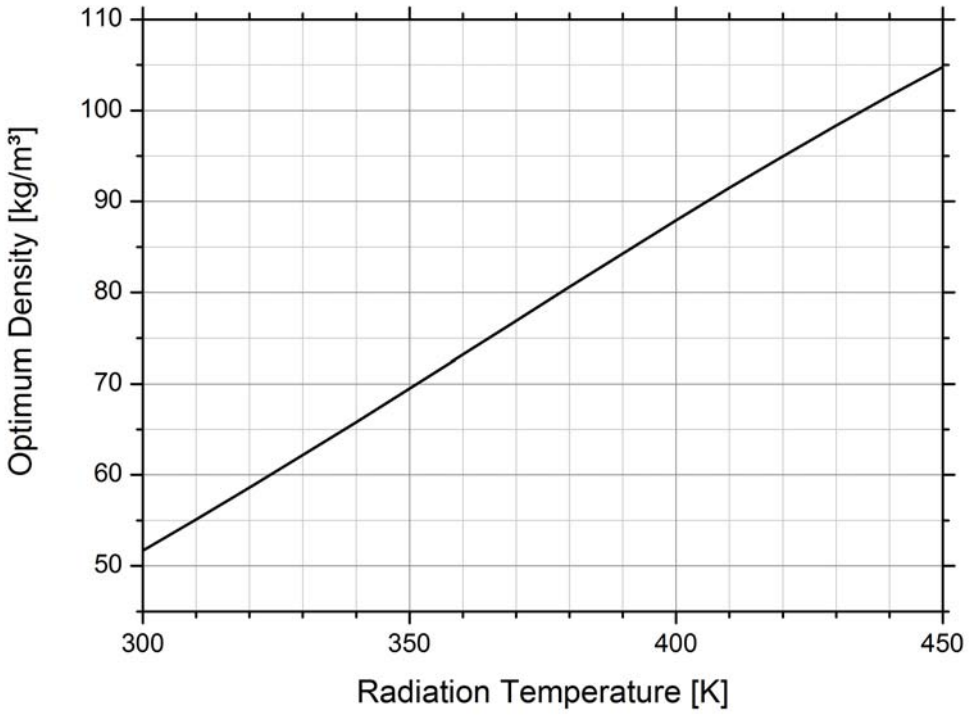

Figure 8.3: Optimum density ρ_{opt} as a function of radiation temperature according to equation 8.9.

Minimization of λ_g and λ_c

Both gas conduction and the coupling effect depend on temperature and pressure (see equations 8.6 and 8.8). Like before, the temperature, which determines the continuum thermal conductivity λ_0, is given by the application. It is obvious that an increase of vacuum pressure, caused by the leakage rate χ, leads to an enhancement of $\lambda_g + \lambda_c$. In practice, it is therefore necessary to keep the vacuum pressure as low as possible during the lifetime of a hot water storage tank, which is around 20 years.

For the conventional application with air as filling gas, this effect is illustrated in figure 8.4, where the time development of $\lambda_g + \lambda_c$ is depicted using the leakage rate χ as a parameter. The values for $\lambda_g + \lambda_c$ have been calculated from equations 8.6 and 8.8 with the parameters $p_{1/2}^g$, Φ and $p_{1/2}^c$ from table 8.1. For normalization, $\lambda_g + \lambda_c$ has been divided by λ_0:

$$\frac{\lambda_g + \lambda_c}{\lambda_0} = \frac{1}{1 + \frac{p_{1/2}^g}{p(t)}} + \frac{\Phi}{1 + \frac{p_{1/2}^c}{p(t)}} \tag{8.10}$$

The pressure $p\,(t)$ is calculated according to:

$$p\,(t) = p_0 + \frac{\chi t}{V_{gap}} \tag{8.11}$$

In this equation, $V_{gap} = 8.43\,\mathrm{m^3}$ is the insulation volume of the prototype and p_0 is the initial pressure, which is set to $p_0 = 0.01\,\mathrm{mbar}$. This value is a suitable compromise for practical applications, because it can be achieved with a moderate technical effort, but gas conduction and coupling is already sufficiently suppressed ($\lambda_g + \lambda_c = 2 \cdot 10^{-4}\,\mathrm{W/mK}$).

The red curve in figure 8.4 with $\chi = 2.3 \cdot 10^{-5}\,\mathrm{mbar\ l/s}$ refers to the storage prototype, which is most likely the worst case regarding the leakage rate. It is assumed that χ can be reduced by a factor of 5 for commercially available storages, because these tanks do not have to be equipped with measurement instrumentation (pressure sensors) and the number of vacuum connections can be decreased. However, for $\chi = 5 \cdot 10^{-6}\,\mathrm{mbar\ l/s}$ (green curve), the value of $\lambda_g + \lambda_c$ is still relatively high after 20 years. With $T = 50\,°\mathrm{C}$ and $\lambda_0 = 27.9 \cdot 10^{-3}\,\mathrm{W/mK}$ [34], one obtains $\lambda_g + \lambda_c = 6 \cdot 10^{-3}\,\mathrm{W/mK}$. A further reduction of the leakage rate (blue and purple curve) is desirable.

Lowering the initial pressure (for example to $p_0 = 0.001\,\mathrm{mbar}$) is not very effective for the long-time consideration of $\lambda_g + \lambda_c$. If $\chi = 2.3 \cdot 10^{-5}\,\mathrm{mbar\ l/s}$, the pressure reaches $p = 0.01\,\mathrm{mbar}$ after only 40 days. Even at the lowest indicated leakage rate of $\chi = 10^{-6}\,\mathrm{mbar\ l/s}$, the pressure rises to $p = 0.01\,\mathrm{mbar}$ after three years.

If the leakage rate cannot be reduced to a sufficiently low value, another option to maintain low thermal conductivities would be to re-evacuate the perlite insulation in regular intervals of several years.

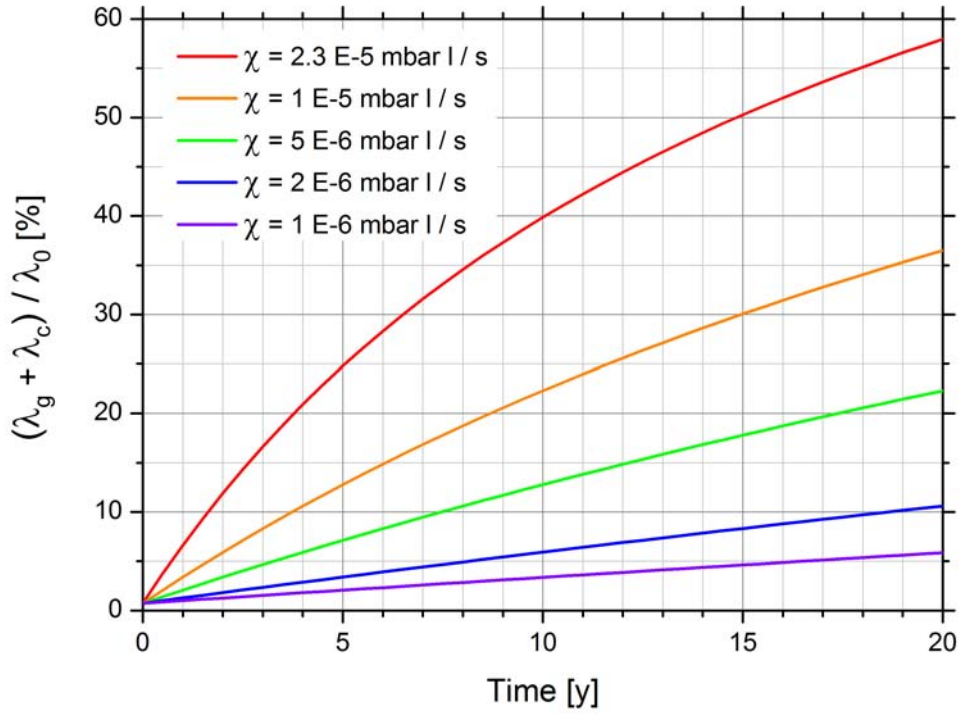

Figure 8.4: Development of $\lambda_g + \lambda_c$ over the typical lifetime of a hot water storage tank at different leakage rates χ according to equation 8.10.

Utilization of Inert Gases

A further theoretical possibility to maintain low effective thermal conductivities during the lifetime of the storages in spite of leakages is the utilization of krypton, which is characterized by its low heat conductivity both in the continuum and in the regime of free molecular flow (see section 4.1). The application of argon is not suggestive, because the thermal conductivity of the perlite insulation under the effect of argon is too close to the value of air (see figure 6.16). It is now examined, whether the usage of krypton is a reasonable option in practice. Therefore, a relation for the pressure dependency of the total thermal conductivity of a gas mixture is necessary. Initially, only gas conduction in the pores is considered, and the coupling effect will be treated by analogy later. From equation 4.13, a relation for the total continuum thermal conductivity λ_0^{tot} of a gas mixture is known, which is now applied to the mixture of air and krypton:

$$\lambda_0^{tot} = \frac{p_{air}\lambda_0^{air} + p_{kr}\lambda_0^{kr}}{p_{air} + p_{kr}} \tag{8.12}$$

In this equation, p_{air} and p_{kr} are the partial pressures of air and krypton, and λ_0^{air} and λ_0^{kr} are the continuum thermal conductivities. As demonstrated by figure 4.3, λ_0^{tot} is always larger than λ_0^{kr} and smaller than λ_0^{air}. In the regime of free molecular flow, this can no longer be valid. Because collisions between the gas molecules can be neglected

and the particles move freely between the boundary walls, the two components of the gas mixture represent a parallel connection of thermal resistances (equation 4.30). Accordingly, the individual thermal conductivities have to add up:

$$\lambda_{FM}^{tot} = \lambda_{FM}^{air} + \lambda_{FM}^{kr} = \frac{p_{air}\lambda_0^{air}}{p_{1/2}^{g,air}} + \frac{p_{kr}\lambda_0^{kr}}{p_{1/2}^{g,kr}} \tag{8.13}$$

The relation $\lambda_{FM}^{air} = p_{air}\lambda_0^{air}/p_{1/2}^{g,air}$ and the analog expression for krypton is obtained from the low-pressure limit of the Sherman interpolation (equation 4.4). With $p \to 0$ and consequently $\left(1 + p_{1/2}^{g,air}/p_{air}\right) \to p_{1/2}^{g,air}/p_{air}$, one arrives at the above term.

Now, the quantity λ_{IGP}^{tot}, which is the interpolation to general pressures (index IGP) of the total thermal conductivity of a gas mixture, is calculated according to:

$$\frac{1}{\lambda_{IGP}^{tot}} = \frac{1}{\lambda_0^{tot}} + \frac{1}{\lambda_{FM}^{tot}} \tag{8.14}$$

This approach corresponds to the Sherman interpolation for a pure, single-component gas [35]. After inserting equations 8.12 and 8.13 and solving for λ_{IGP}^{tot}, one arrives at:

$$\frac{\lambda_{IGP}^{tot}}{\lambda_0^{air}} = \frac{\left(p_{air} + p_{kr}\frac{\lambda_0^{kr}}{\lambda_0^{air}}\right)\left(p_{air}p_{1/2}^{g,kr} + p_{kr}p_{1/2}^{g,air}\frac{\lambda_0^{kr}}{\lambda_0^{air}}\right)}{(p_{air}+p_{kr})\left(p_{air}p_{1/2}^{g,kr} + p_{kr}p_{1/2}^{g,air}\frac{\lambda_0^{kr}}{\lambda_0^{air}}\right) + p_{1/2}^{g,air}p_{1/2}^{g,kr}\left(p_{air} + p_{kr}\frac{\lambda_0^{kr}}{\lambda_0^{air}}\right)} \tag{8.15}$$

Again, the values are normalized by λ_0^{air}. This is possible, because the ratio $\lambda_0^{kr}/\lambda_0^{air}$ only varies between 0.364 at $T = 0\,°\mathrm{C}$ and 0.370 at $T = 300\,°\mathrm{C}$ (compare figure 8.1). Therefore, $\lambda_0^{kr}/\lambda_0^{air} = 0.367$ is set as a constant, which is exact for temperatures around $T = 125\,°\mathrm{C}$ and a very good approximation with a deviation of maximally 1 % for lower and higher temperatures. The reason for this procedure is, that the calculated values from equation 8.15 are directly comparable to the curves in figure 8.4.

So far, only gas conduction in the pores has been considered. However, an analog expression can easily be derived for the coupling thermal conductivity $\lambda_{IGP}^{tot,c}$ of the gas mixture by replacing the terms λ_0 with $\Phi\lambda_0$ and the characteristic pressures $p_{1/2}^{g}$ with $p_{1/2}^{c}$:

$$\frac{\lambda_{IGP}^{tot,c}}{\lambda_0^{air}} = \frac{\left(p_{air}\Phi_{air} + p_{kr}\Phi_{kr}\frac{\lambda_0^{kr}}{\lambda_0^{air}}\right)\left(p_{air}p_{1/2}^{c,kr}\Phi_{air} + p_{kr}p_{1/2}^{c,air}\Phi_{kr}\frac{\lambda_0^{kr}}{\lambda_0^{air}}\right)}{(p_{air}+p_{kr})\left(p_{air}p_{1/2}^{c,kr}\Phi_{air} + p_{kr}p_{1/2}^{c,air}\Phi_{kr}\frac{\lambda_0^{kr}}{\lambda_0^{air}}\right) + p_{1/2}^{c,air}p_{1/2}^{c,kr}\left(p_{air}\Phi_{air} + p_{kr}\Phi_{kr}\frac{\lambda_0^{kr}}{\lambda_0^{air}}\right)} \tag{8.16}$$

Now, the sum of gas conduction and coupling $\lambda_g + \lambda_c$ can be calculated by adding equations 8.15 and 8.16. For the characteristic pressures $p_{1/2}$ and the weighting factors Φ, the values from table 8.1 are inserted. Because the time-development of the total thermal conductivity at different leakage rates is to be considered, the previously used relation has to be inserted for the partial pressure of air:

$$p_{air} = p_{air,0} + \frac{\chi t}{V_{gap}} \tag{8.17}$$

Just like before, the void volume of the insulation is given by $V_{gap} = 8.43\,\mathrm{m^3}$, and the initial pressure is set to $p_{air,0} = 0.01\,\mathrm{mbar}$. The partial pressure of krypton is assumed to be constant over the whole time interval and is initially set to $p_{kr} = 1\,\mathrm{mbar}$. Although the partial pressure of krypton in the ambient air is lower, the escape of krypton through the leakages due to diffusion can be neglected for two reasons:

- The krypton fraction of the atmosphere is in the range of 1 ppm [68], which corresponds to a partial pressure of almost zero. The difference of partial pressures, which is the driving force for the pressure equalization, is thus given by the partial pressure $p_{kr} = 1\,\mathrm{mbar}$ inside the insulation of the storage tank. This value is much smaller than the difference in the partial pressures of air, which is practically equal to $\Delta p_{air} = 1000\,\mathrm{mbar}$.
- The outward diffusion of krypton is obstructed by the opposingly directed flow of ambient air into the evacuated insulation volume.

Consequently, all revelant quantities are known, and the time development of the sum of gas conduction in the pores and coupling can be computed for the gas mixture of air and krypton. The result for $p_{kr} = 1\,\mathrm{mbar}$ is shown in figure 8.5. Another plot for $p_{kr} = 0.1\,\mathrm{mbar}$ is depicted in figure 8.6.

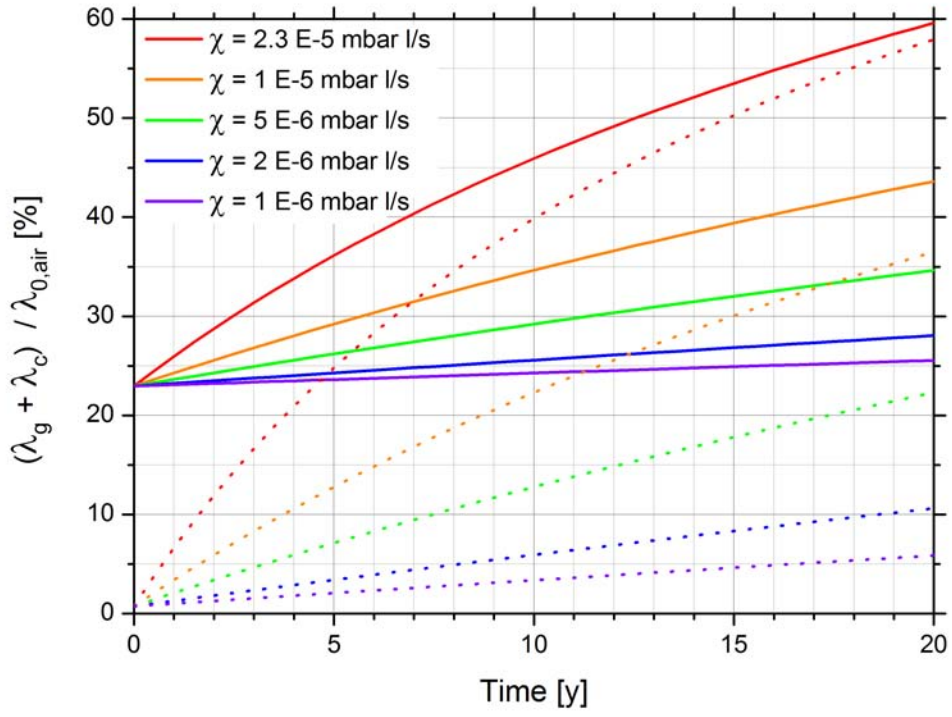

Figure 8.5: Development of $\lambda_g + \lambda_c$ over the lifetime of a hot water storage tank with a mixture of air and krypton according to equations 8.15 and 8.16. Due to the leakage rate χ, the composition of the gas mixture changes. The krypton pressure is set to $p_{kr} = 1\,\mathrm{mbar}$. For comparison, the curves without krypton from figure 8.4 are depicted, too (dotted lines).

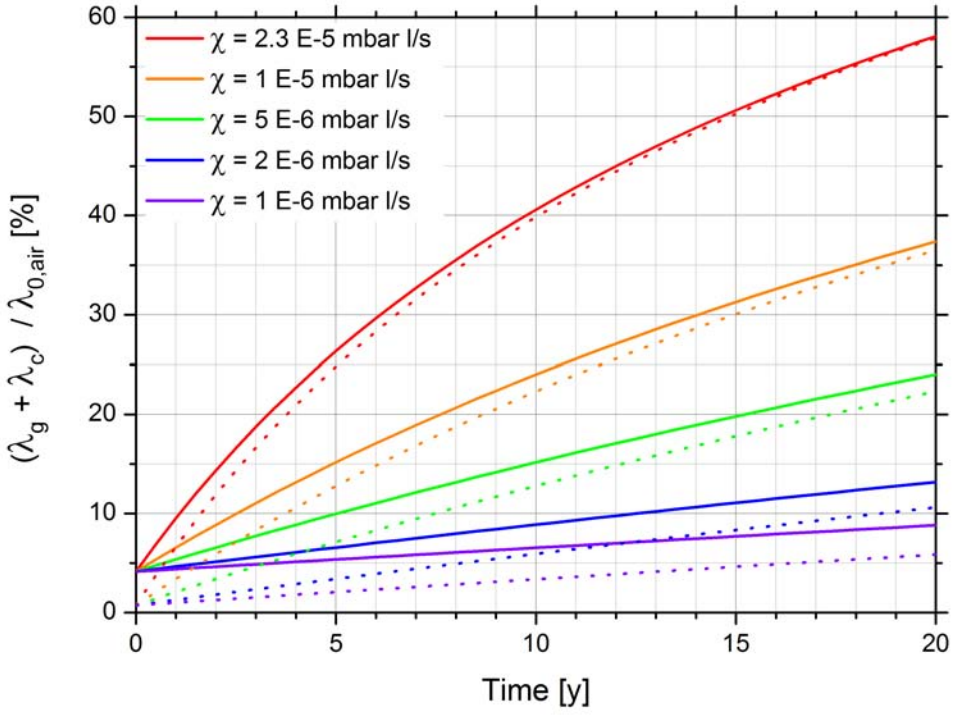

Figure 8.6: Development of $\lambda_g + \lambda_c$ over the lifetime of a hot water storage tank with a mixture of air and krypton according to equations 8.15 and 8.16. Due to the leakage rate χ, the composition of the gas mixture changes. The krypton pressure is set to $p_{kr} = 0.1$ mbar. For comparison, the curves without krypton from figure 8.4 are depicted, too (dotted lines).

It shows that $p_{kr} = 1$ mbar is not a suitable value, because the overall thermal conductivity is already too high (compare also figure 6.16), and the resulting curves are above those without krypton during the whole time interval (figure 8.5). The utilization of krypton at $p_{kr} = 0.1$ mbar is not beneficial either, the only difference is that the initial value of $\lambda_g + \lambda_c$ at $t = 0$ is lowered (figure 8.6). A further reduction of the krypton partial pressure is not reasonable, because the curves would approximate those in figure 8.4 after a very short period in this case. The advantage of krypton only becomes notable if the total pressure is in the continuum regime. However, setting the krypton pressure to $p_{kr} = 10$ mbar or higher is not suitable either. In this case, one would obtain a more or less horizontal line at a value of around $(\lambda_g + \lambda_c) / \lambda_0^{air} = 60\,\%$ in the indicated plots. There is a point in time, where the curves in figure 8.4 cross this horizontal line, but the break-even point is not reached within the time interval of 20 years.

In general, it can be said that the utilization of krypton is not advantageous in practice, because the thermal conductivity of the gas mixture is only lowered in the continuum compared to pure air (see equation 8.12). At the low pressures of a vacuum super insulation, in the regime of free molecular flow, both contributions of air and krypton add up, which results in a higher total thermal conductivity (equation 8.13). As a consequence, it is much more reasonable, not to use krypton and to re-evacuate the insulation of the storage tanks in regular time intervals, if the leakage rate can't be reduced far enough.

Chapter 9

Outlook

The experimental investigation of the heat transport in evacuated perlite showed, that the single heat transfer mechanisms and their dependencies on pressure, density and temperature can be described using common models and approaches. Due to this quantification, the effective thermal conductivity of TECHNOPERL ® - C 1,5 can be calculated for practical applications, and optimization approaches can be suggested. However, there is still motivation for future research and optimization.

Regarding the experiments, a first approach would be the improvement of the cut-off cylinder device, with the aim to reduce the leakage rate and to obtain minimum pressures lower than $p = 0.02\,\text{mbar}$. As a consequence, it would be possible to further investigate the temperature dependency of solid conduction, and to measure the pressure-dependent part $\lambda_g + \lambda_c$ of the effective thermal conductivity below $p = 1\,\text{mbar}$. In addition, the geometry and the positioning of the installed cables can be optimized in order to facilitate the calibration. Furthermore, a comparison between a parallel plate setup and a cylindrical geometry could be worthwile. In the experimental part of this thesis, it has been notable that both measurement setups have their distinct benefits and disadvantages. The comparison, which could also include spherical geometries, can be interesting and helpful for thermal conductivity measurements in general.

With respect to the experimental results, a main topic for further analysis is the coupling effect. Although it showed that the model for perlite, which was developed in section 4.4, can reproduce the experiments, its physical interpretation is not completely clarified. The increase of the weighting factor Φ, which was observed for argon and krypton, was explained by the accommodation coefficient. To validate this approach, further measurements and also theoretical considerations are a possible subject of additional research. In addition, a microscopic inspection or a similar examination of the material structure is desirable, in order to verify the effective pore diameters and the intergranular space dimensions, which were calculated from the experimentally determined characteristic pressures $p_{1/2}$. This study could also clarify the effect of external mechanical pressure on the material structure and the correlated solid thermal conductivity.

Ultimately, other porous materials in combination with different filling gases can be investigated. Apart from perlite, there are several similar materials, for example diatomaceous earth, expanded clay or aerogels. In addition to air, argon and krypton, one can think of the remaining inert gases helium, neon and xenon. Especially the latter may be particularly interesting for insulation purposes due to its low thermal conductivity (compare figure 8.1). From the scientific point of view, the development of a comprehensive model regarding the coupling effect for different combinations of materials and gases is a challenging topic for further research, which has not been solved until now [42].

Nomenclature

symbol	unit	meaning
A	m^2	area
A_s	$\mathrm{W\ m^2\ K^{-1}\ kg^{-1}}$	coefficient for the density dependency of λ_s
$a^*_\lambda(\lambda)$	$\mathrm{m^2\ kg^{-1}}$	spectral mass-specific absorption coefficient
a	1	weighting factor
B		bandwidth
b	1	weighting factor
C	$\mathrm{J\ K^{-1}}$	integral heat capacity
c	$\mathrm{m\ s^{-1}}$	speed of light in vacuum
$\tilde{c}$	$\mathrm{m\ s^{-1}}$	speed of light in a medium
c_p	$\mathrm{J\ kg^{-1}\ K^{-1}}$	specific heat capacity at constant pressure
c_V	$\mathrm{J\ kg^{-1}\ K^{-1}}$	specific heat capacity at constant volume
D	m	distance
D_v	$\mathrm{m^2\ kg^{-1}\ s^{-1}}$	vapor diffusion coefficient
$D\left(\tilde{\nu}\right)$		window function
d	m	distance or thickness or diameter
d_c	m	characteristic length
E	J	energy
E_{ex}	$\mathrm{m^{-1}}$	extinction coefficient

symbol	unit	meaning
$e\,(\tilde{\nu})$	1	spectral extinction
$e^*(T)$	$\mathrm{m^2\ kg^{-1}}$	mass-specific extinction coefficient
$e^*_\lambda(\lambda)$	$\mathrm{m^2\ kg^{-1}}$	spectral mass-specific extinction coefficient
F	1	view factor
$F\,(v)$		Maxwell-Boltzmann distribution
f	1	degrees of freedom
$\hat{f}$	$\mathrm{m^2}$	accommodation factor
$f_R(\lambda, T)$		Rosseland function
g	$\mathrm{m\ s^{-2}}$	gravity of Earth
H	m	height
H_c	$\mathrm{W\ m^{-2}\ K^{-1}}$	heat transfer coefficient for convection
H_i	$\mathrm{W\ m^{-2}\ K^{-1}}$	heat transfer coefficient for insulation materials
h	J s	Planck constant
Δh_v	$\mathrm{J\ kg^{-1}}$	specific heat of evaporation
I	$\mathrm{W\ m^{-2}}$	radiation intensity
I_{el}	A	electrical current
i		imaginary unit
k_B	$\mathrm{J\ K^{-1}}$	Boltzmann constant
l	m	length
l_f	m	mean free path
M	$\mathrm{kg\ mol^{-1}}$	molar mass
m	kg	mass
N	1	quantity, total number
Nu	1	Nusselt number
n	$\mathrm{m^{-3}}$	particle density
$\tilde{n}$	1	refractive index
P_{el}	W	electrical heating power

symbol	unit	meaning
p	mbar	pressure
$p_{1/2}$	mbar	characteristic half-value pressure
$p_{1/2}^{c}$	mbar	characteristic pressure for coupling
$p_{1/2}^{g}$	mbar	characteristic pressure for gas conduction in pores
p_{sat}	Pa	saturation vapor pressure
$\dot{Q}$	W	thermal power or rate of heat transfer
$\dot{\vec{q}}$	W m^{-2}	area-specific heat flux
R	J mol^{-1} K^{-1}	gas constant
R_{el}	Ω	electrical resistance
R_{th}	K W^{-1}	thermal resistance
r	m	radius
Ra	1	Rayleigh number
Re	1	Reynolds number
S	m	shape factor
$s_{\lambda}^{*}(\lambda)$	m^2 kg^{-1}	spectral mass-specific scattering coefficient
T	K	temperature
T_0	K	initial temperature
T_a	K	ambient temperature
T_r	K	radiation temperature
t	s	time
U	V	voltage
u	J m^{-3}	energy density
V	m^3	volume
v	m s^{-1}	velocity
w	%	water content
x	m	spatial coordinate

symbol	unit	meaning
α	1	accommodation coefficient or absorptivity
α_{red}	1	reduced accommodation coefficient
β	°	inclination angle
β_S	1	gas-specific constant for Sherman interpolation
Γ	1	weighting factor for the two contributions of λ_c
γ	1	exponent for density-dependence of λ_s
Δ		error or difference
δ	m	characteristic length for convection
ε	1	emissivity
ε_{eff}	1	effective emissivity
κ	m^{-1}	absorption coefficient
λ	$\mathrm{W\,m^{-1}\,K^{-1}}$	thermal conductivity
λ	m	wavelength
λ_c	$\mathrm{W\,m^{-1}\,K^{-1}}$	coupling thermal conductivity
λ_{eff}	$\mathrm{W\,m^{-1}\,K^{-1}}$	effective thermal conductivity
λ_g	$\mathrm{W\,m^{-1}\,K^{-1}}$	gaseous thermal conductivity
λ_{max}	m	wavelength of maximum intensity
λ_r	$\mathrm{W\,m^{-1}\,K^{-1}}$	radiation thermal conductivity
λ_s	$\mathrm{W\,m^{-1}\,K^{-1}}$	solid thermal conductivity (porous bulk)
λ_s^*	$\mathrm{W\,m^{-1}\,K^{-1}}$	solid thermal conductivity (massive material)
λ_0	$\mathrm{W\,m^{-1}\,K^{-1}}$	continuum gas thermal conductivity
μ	Pa s	dynamic viscosity
ν	Hz	frequency
$\tilde{\nu}$	m^{-1}	wave number
Π	1	modified porosity which only includes pores
π	1	circular constant
ρ	$\mathrm{kg\,m^{-3}}$	mass density
ϱ	1	reflectivity

symbol	unit	meaning
σ	W m^{-2} K^{-4}	Stefan-Boltzmann constant
σ_{el}	Ω^{-1} m^{-1}	electrical conductivity
ς	m^2	cross section for intermolecular collisions
τ	1	transmissivity
τ_0	1	optical thickness
Φ	1	weighting factor for the coupling effect
φ	°	angle
χ	mbar l s^{-1}	leakage rate
Ψ	1	porosity

Bibliography

[1] Bundesministerium für Umwelt, Naturschutz und Reaktorsicherheit: *Erneuerbare Energien in Zahlen - Internet-Update ausgewählter Daten*. Berlin, 2010. http://www.bmu.de/files/pdfs/allgemein/application/pdf/ee_in_deutschland_update_bf.pdf (July 28, 2011).

[2] T. Beikircher, F. Buttinger: *Projektantrag: Superisolierter Heißwasser-Langzeitwärmespeicher*. Fördernummer 0325964A (Bundesministerium für Umwelt, Naturschutz und Reaktorsicherheit), ZAE Bayern, Garching, 2010.

[3] Bundesministerium für Umwelt, Naturschutz und Reaktorsicherheit: *Umweltbewusstsein in Deutschland 2010 - Ergebnisse einer repräsentativen Bevölkerungsumfrage*. Berlin, 2010. http://www.umweltdaten.de/publikationen/fpdf-l/4045.pdf (July 28, 2011).

[4] http://en.wikipedia.org/wiki/Fukushima_I_nuclear_accidents (June 17, 2011).

[5] http://de.wikipedia.org/wiki/Atomausstieg (June 17, 2011).

[6] Energy Watch Group: *Crude Oil - The Supply Outlook*. Ottobrunn, 2007. http://www.energywatchgroup.com/fileadmin/global/pdf/EWG_Oilreport_10-2007.pdf (July 28, 2011).

[7] Bundesministerium für Wirtschaft und Technologie: *Energiedaten - ausgewählte Grafiken*. Berlin, 2011. http://www.bmwi.de/BMWi/Redaktion/PDF/E/energiestatistiken-grafiken,property=pdf,bereich=bmwi,sprache=de,rwb=true.pdf (July 28, 2011).

[8] http://en.wikipedia.org/wiki/Emissions_trading (June 17, 2011).

[9] Bundesministerium für Wirtschaft und Technologie: *Energie in Deutschland - Trends und Hintergründe zur Energieversorgung*. Berlin, 2010. http://www.bmwi.de/Dateien/Energieportal/PDF/energie-in-deutschland, property=pdf,bereich=bmwi,sprache=de,rwb=true.pdf (July 28, 2011).

[10] J. Fricke, W. L. Borst: *Energie - Ein Lehrbuch der physikalischen Grundlagen*. 2. Auflage, Oldenbourg Verlag, München, 1984.

[11] A. Goetzberger, V. Wittwer: *Sonnenenergie - Physikalische Grundlagen und thermische Anwendungen*. 3. Auflage, Teubner Verlag, Stuttgart, 1993.

[12] http://de.wikipedia.org/wiki/Ölpreis (May 12, 2011).

[13] Fachinformationszentrum Karlsruhe, BINE Informationsdienst: *Selektive Absorberbeschichtungen in Solarkollektoren*. Projektinfo 05/1999. http://www.bine.info/fileadmin/content/Publikationen/Projekt-Infos/1999/Projekt-Info_05-1999/projekt_0599internetx.pdf (July 28, 2011).

[14] Fachinformationszentrum Karlsruhe, BINE Informationsdienst: *Thermische Nutzung der Sonnenenergie*. basisEnergie Nr. 4, 2003.

[15] Fachinformationszentrum Karlsruhe, BINE Informationsdienst: *Thermische Solaranlagen*. basisEnergie Nr. 4, 2008. http://www.bine.info/fileadmin/content/Publikationen/Basis_Energie/Basis_Energie_Nr._04/basisEnergie_04_internetx.pdf (July 28, 2011).

[16] D. Häfner: *Wärmespeicher-Neuheiten: Größer, frischer, kompakter*. Sonne, Wind & Wärme, 18/2009 , 44-53.

[17] H. Drück, H. Müller-Steinhagen: *Innovative Speicherkonzepte für Kombianlagen mit hohen solaren Deckungsanteilen*. Universität Stuttgart, Institut für Thermodynamik und Wärmetechnik (ITW), 2003.

[18] I. Röpcke: *Solarwärme: Vom Speicher mit Haus zum Haus mit Speicher*. Sonderdruck aus Sonne, Wind & Wärme 2/2007, 1-4.

[19] B. Janzing: *Großspeicher in Stahl, Beton und Polyester*. Solarthemen 312, 20-23, 2009.

[20] E. Augsten, J. Berner, K. Ertmer, C. Hilgers, J.-P. Meyer, I. Röpcke: *Intersolar - Neue Systemkomponenten: Für den Keller fast zu schade*. Sonne, Wind & Wärme 10/2010, 94-103.

[21] A. Deimling: *Wärmedämmung von Vakuum-Stahlmantel-Fernheizrohren*. Dissertation, Universität Dortmund, Abteilung Chemietechnik, 1983.

[22] Forschungsstelle für Energiewirtschaft: *Ermittlung von Energiekennzahlen für Anlagen, Herstellungsverfahren und Erzeugnisse*. München, 1999. http://www.ffe.de/download/langberichte/Kennzahlen.pdf (July 28, 2011).

[23] F. Buttinger: *Entwicklung eines konzentrierenden Vakuum-Flachkollektors zur Prozesswärmeerzeugung*. Dissertation, Technische Universität München, Fakultät für Maschinenwesen, 2009.

[24] Fachinformationszentrum Karlsruhe, BINE Informationsdienst: *Solarthermische Kraftwerke werden Praxis*. Projektinfo 07/2008.

http://www.bine.info/fileadmin/content/Publikationen/Projekt-Infos/2008/Projekt-Info_07-2008/projekt_0708internet_x.pdf (July 28, 2011).

[25] International Energy Agency: *Technology Roadmap - Concentrating Solar Power*. Paris, 2010.
http://www.iea.org/papers/2010/csp_roadmap.pdf (July 28, 2011).

[26] http://upload.wikimedia.org/wikipedia/commons/0/01/Solar_troughs_in_the_Negev_desert_of_Israel.jpg (July 6, 2011).

[27] http://www.torresolenergy.com/EPORTAL_DOCS/GENERAL/SENERV2/DOC-cw4de8a92aec33f/gemasolar-october-27-2010hi.jpg (July 6, 2011).

[28] Y. A. Çengel: *Heat Transfer - A Practical Approach*. McGraw-Hill, Boston, 1998.

[29] http://upload.wikimedia.org/wikipedia/commons/0/0e/BlackbodySpectrum_loglog_150dpi_de.png (May 13, 2011).

[30] W. Wagner: *Wärmeübertragung*. 5. Auflage, Vogel Buchverlag, Würzburg, 1998.

[31] H. D. Baehr, K. Stephan: *Wärme- und Stoffübertragung*. 7. Auflage, Springer Verlag, Berlin, 2010.

[32] U. Grigull, H. Sandner: *Wärmeleitung*. Springer Verlag, Berlin, 1979.

[33] W. Polifke, J. Kopitz: *Wärmeübertragung: Grundlagen, analytische und numerische Methoden*. 2. Auflage, Pearson Studium, München, 2009.

[34] Verein Deutscher Ingenieure: *VDI-Wärmeatlas: Berechnungsblätter für den Wärmeübergang*. 9. Auflage, Springer Verlag, Berlin, 2002.

[35] T. Beikircher: *Gaswärmeleitung in evakuierten Sonnenkollektoren*. Dissertation, Ludwig-Maximilians-Universität München, Fakultät für Physik, 1996.

[36] T. Beikircher: *Vermessung und Optimierung eines evakuierbaren Flachkollektors*. Diplomarbeit, Ludwig-Maximilians-Universität München, Fakultät für Physik, 1991.

[37] I. Prigogine, P. Glansdorff: *Thermodynamic Theory of Structure, Stability and Fluctuations*. Wiley Interscience, New York, 1971.

[38] S. S. Kistler: *Coherent Expanded Aerogels and Jellies*. Nature 127, 741, 1931.

[39] J. Fricke: *Aerogele*. Physik in unserer Zeit 17 Nr. 4, 101, 1986.

[40] J. Fricke: *FCKW-freie Wärmedämmungen*. Physik in unserer Zeit 20 Nr. 6, 189-191, 1989.

[41] M. Wiener: *Synthese und Charakterisierung Sol-Gel-basierter Kohlenstoff-Materialien für die Hochtemperatur-Wärmedämmung*. Dissertation, Julius-Maximilians-Universität Würzburg, Fakultät für Physik und Astronomie, 2009.

[42] K. Swimm, G. Reichenauder, S. Vidi, H-P. Ebert: *Gas Pressure Dependence of the Heat Transport in Porous Solids with Pores Smaller than 10 µm*. International Journal of Thermophysics 30, 1329-1342, 2009.

[43] http://de.wikipedia.org/wiki/Wärmedämmung (May 13, 2011).

[44] http://de.wikipedia.org/wiki/Wärmeleitfähigkeit (May 13, 2011).

[45] http://www.knaufinsulation.de/files/ki_de/imagecache/normal/files/ki_de/upload/17021-Heralan-LAM-AR-D.jpg (May 13, 2011).

[46] http://img.archiexpo.de/images_ae/photo-g/starre-dammplatte-aus-polyurethanschaum-160941.jpg (May 13, 2011).

[47] http://upload.wikimedia.org/wikipedia/commons/7/7c/Styropian.jpg (May 13, 2011).

[48] http://upload.wikimedia.org/wikipedia/commons/7/7f/Foamglas.jpg (May 13, 2011).

[49] http://upload.wikimedia.org/wikipedia/commons/3/34/Dewargefäß.jpg (May 13, 2011).

[50] J. Fricke: *Von der thermischen Isolation zur Superisolation*. Physik in unserer Zeit 15 Nr. 2, 42-50, 1984.

[51] http://en.wikipedia.org/wiki/Multi-layer_insulation (May 13,2011).

[52] http://de.wikipedia.org/wiki/Multilayer_Insulation (May 13, 2011).

[53] A. Frohn: *Einführung in die kinetische Gastheorie*. 2. Auflage, AULA-Verlag, Wiesbaden, 1988.

[54] C. Cercignani: *The Boltzmann Equation and its Applications*. Springer Verlag, New York, 1988.

[55] E. H. Kennard: *Kinetic theory of gases*. McGraw-Hill, New York, 1938.

[56] F. S. Sherman. In: J. A. Laurmann, editor: *Rarefied Gas Dynamics Vol. II*. Academic Press, New York, 1963.

[57] J. Fricke, H. Schwab, U. Heinemann: *Vacuum Insulation Panels - Exciting Thermal Properties and Most Challenging Applications*. International Journal of Thermophysics 27 No. 4, 1123-1139, 2006.

[58] M. Smoluchowski, R. v. Smolan: *Über den Temperatursprung bei Wärmeleitung in Gasen*. Sitzungsberichte der Akademie der Wissenschaften in Wien 107, IIa, 304-329, 1898.

[59] M. Smoluchowski, R. v. Smolan, Annalen der Physik 34, 593 ff, 1898.

[60] R. Gross, A. Marx: *Festkörperphysik - Vorlesungsskript*. Walther-Meissner-Institut, Garching, 2010.

[61] H. Schwab: *Vakuumisolationspaneele - Gas- und Feuchteeintrag sowie Feuchte- und Wärmetransport*. Dissertation, Julius-Maximilians-Universität Würzburg, Fakultät für Physik und Astronomie, 2004.

[62] ZAE Bayern: *Vakuumdämmung im Bauwesen - Vorlesungsumdruck*. Nürnberg, 2010.
http://www.vip-bau.de/ (July 29, 2011).

[63] U. Heinemann: *Bestimmung der Strahlungswärmeleitfähigkeit von zwei Perliten*. ZAE Bayern, Würzburg, 2010.

[64] P. Zehner, E. U. Schlünder: *Einfluß der Wärmestrahlung und des Druckes auf den Wärmetransport in nicht durchströmten Schüttungen*. Chemie Ingenieur Technik 44, 1303-1308, 1972.

[65] S. Vidi: personal note.

[66] http://en.wikipedia.org/wiki/Nitrogen (May 16, 2011).

[67] http://en.wikipedia.org/wiki/Argon (May 16, 2011).

[68] http://en.wikipedia.org/wiki/Krypton (May 16, 2011).

[69] http://en.wikipedia.org/wiki/Xenon (May 16, 2011).

[70] T. Beikircher et al.: *A Modified Temperature-Jump Method for the Transition and Low-Pressure Regime*. Journal of Heat Transfer 120, 965-970, 1998.

[71] A. Wassiljewa: *Wärmeleitung in Gasgemischen*, Zeitschrift für Physik 5, 737-742, 1904.

[72] http://de.wikipedia.org/wiki/Eigenschaften_des_Wassers (May 16, 2011).

[73] O. Krischer, W. Kast: *Die wissenschaftlichen Grundlagen der Trocknungstechnik*. 3. Auflage, Springer Verlag, Berlin, 1992.

[74] F. Ochs, W. Heidemann, H. Müller-Steinhagen: *Effective Thermal Conductivity of Moistened Insulation Materials as a Function of Temperature*. International Journal of Heat and Mass Transfer 51, 539-552, 2008.

[75] F. Ochs, H. Stumpp, D. Mangold, W. Heidemann, H. Müller-Steinhagen: *Bestimmung der feuchte- und temperaturabhängigen Wärmeleitfähigkeit von Dämmstoffen*. Universität Stuttgart, Institut für Thermodynamik und Wärmetechnik (ITW), 2004.

[76] http://serc.carleton.edu/images/research_education/equilibria/h2o_phase_diagram_-_color.v2.jpg (July 11, 2011).

[77] http://en.wikipedia.org/wiki/Perlite (May 13, 2011).

[78] http://de.wikipedia.org/wiki/Perlit_(Gestein) (May 13, 2011).

[79] Europerl, Stauss-Perlite GmbH: *Informationsblatt Technoperl ® - C 1,5*. http://www.europerl.at/fileadmin/downloads/Europerl/Allgemein/Andere_Sprachen/Cryogenic_Europerl_englisch__1.4.pdf (July 28, 2011).

[80] http://upload.wikimedia.org/wikipedia/commons/d/d9/Perlite1.jpg (May 13, 2011).

[81] http://www.hycar.de/liquid.htm (May 13, 2011).

[82] A. Deimling, A. Steiff, P.-M. Weinspach: *Vakuum-Wärmedämmung bei Stahlmantel-Fernheizrohren*, Wärme- und Stoffübertragung 18, 129-140, 1984.

[83] Fachinformationszentrum Karlsruhe, BINE Informationsdienst: *Dämmen durch Vakuum - Hocheffizienter Wärmeschutz für Gebäudehülle und Fenster*. Themeninfo I/2011. http://www.bine.info/fileadmin/content/Publikationen/Themen-Infos/I_2011/TI_I_11_internetx.pdf (July 28, 2011).

[84] Fachinformationszentrum Karlsruhe, BINE Informationsdienst: *Vakuumdämmung*. Projektinfo 04/2001. http://www.bine.info/fileadmin/content/Publikationen/Projekt-Infos/2001/Projekt-Info_04-2001/projekt_0401internetx.pdf (July 28, 2011).

[85] D. Gintars, U. Heinemann: *Dämmen mit dem Nichts*. Deutsches Ingenieurblatt 03/2008, 20-24.

[86] http://www.vip-bau.de/pics/eng/vipcut.jpg (May 13, 2011).

[87] Europerl, Stauss-Perlite GmbH: *Datenblatt Technoperl ®*. http://www.europerl.at/fileadmin/downloads/Europerl/Produktdatenblaetter/EI-UEbersicht-a_-11.pdf (July 28, 2011).

[88] http://en.wikipedia.org/wiki/Fourier_transform_infrared_spectroscopy (June 7, 2011).

[89] http://www.ir-spektroskopie.de/spec/ftir-prinzip/index.html (June 7, 2011).

[90] P. R. Griffiths, J. A. de Haseth: *Fourier Transfom Infrared Spectroscopy*. 2nd edition, John Wiley & Sons, Hoboken, 2007.

[91] ZAE Bayern: *Two-Plate Vacuum-Capable Apparatuses for Determining Thermal Conductivity between -200 °C and 800 °C*. Würzburg, 2007.

[92] U. Heinemann, J. Hetfleisch, R. Caps, J. Kuhn, J. Fricke: *Evacuable Guarded Hot Plate for Thermal Conductivity Measurements beetween -200 °C and 800 °C*. Advances in Thermal Insulation - Proceedings of the Eurotherm Seminar No. 44, Espinho, 1995.

[93] X. Lu: *Transport Properties of Porous Media*. Dissertation, Julius-Maximilians-Universität Würzburg, Fakultät für Physik und Astronomie, 1991.

[94] R. Caps, U. Heinemann, J. Fricke, K. Keller: *Thermal conductivity of polyimide foams*. International Journal of Heat and Mass Transfer 40, 269-280, 1997.

[95] Europerl, Stauss-Perlite GmbH: *Siebanalyse Technoperl ®*. http://www.europerl.at/fileadmin/downloads/Europerl/Produktdatenblaetter/Technoperl_Sieblinen_2005.pdf (July 28, 2011).

[96] K. Jousten: *Wutz Handbuch Vakuumtechnik*. 9. Auflage, Vieweg + Teubner Verlag, Wiesbaden, 2006.

[97] Pfeiffer Vacuum GmbH: *Ceramic Capacitance Gauge CMR 361 ... CMR 365 Betriebsanleitung*.

[98] Oerlikon Leybold Vacuum GmbH: *Ceravac-Transmitter CTR 100 Gebrauchsanleitung*.

[99] http://de.wikipedia.org/wiki/Pt100 (June 30, 2011).

[100] DIN EN 60751 http://www.fh-jena.de/~endter/Schaltungssimulation/DIN%20EN%2060751%20Pt100.pdf (June 30, 2011).

[101] http://www.meteo.physik.uni-muenchen.de/mesomikro/garstat/messung.php (July 28, 2011).

[102] http://de.wikipedia.org/wiki/Edelstahl (July 14, 2011).

[103] S. C. Saxena, R. K. Joshi: *Thermal accommodation and adsorption coefficients of gases*. Hemisphere Publishing Corporation, New York, 1989.

[104] Mettler-Toledo AG: *Moisture Analyzer HR83 and HR83-P Operating Instructions*.

[105] K. M. Heißler: *Analytische Berechnung und CFD-Simulation der Wärmeverluste eines superisolierten Wärmespeichers*. Semesterarbeit, Technische Universität München, Fakultät für Maschinenbau, 2011.

[106] Hummelsberger GmbH: construction plans hot water storage prototype.

[107] http://de.wikipedia.org/wiki/Dichteanomalie (July 19, 2011).

[108] http://www.schweizer-fn.de/stoff/wkapazitaet/v2_wkapazitaet_metall.htm (July 19, 2011).

[109] http://www.schweizer-fn.de/stoff/wkapazitaet/v2_wkapazitaet_isolierung.htm (July 19, 2011).

[110] http://www.schweizer-fn.de/stoff/wleit_metall/v2_wleit_metall.htm (July 20, 2011).

[111] http://www.tommasinfondi.it/de/produkte/gewoelbte-gefaessboeden/typ-td/,325 (July 20, 2011).

[112] http://www.weisstaler.de/web/1/produkte/boeden/kloepperboden.html (July 20, 2011).

[113] http://de.wikipedia.org/wiki/Kugelsegment (July 20, 2011).

Acknowledgment

First, I would like to thank Prof. Dr. Rudolf Gross for his helpfulness and his willingness to supervise this master thesis, which has given me the opportunity to pursue my personal interests regarding the topic of the thesis.

My gratitude goes to Dr. Thomas Beikircher for supporting my work, providing helpful information and discussing the details of heat transport and correlated topics, which has brought me a lot of knowledge and understanding.

Last but not least, I would like to thank my colleagues at ZAE BAYERN, especially Dr. Frank Buttinger, Peter Kronthaler, Martin Heißler, Christopher Kaiser, Patrick Wagner and Lukas Pospiech for their support and for the pleasant working atmosphere.